PHYSICS OF THE STRUCTURAL COLOR ON THE SKIN OF CEPHALOPODS

A Dissertation

by

MENG GAO

Submitted to the Office of Graduate Studies of
Texas A&M University
in partial fulfillment of the requirements for the degree of

DOCTOR OF PHILOSOPHY

Approved by:

Chair of Committee,	George W. Kattawar
Committee Members,	Roland E. Allen
	Edward S. Fry
	Ping Yang
Department Head,	George R. Welch

December 2012

Major Subject: Physics

ABSTRACT

The structural colors, produced by leucophore and iridophore cells, are important for cephalopod camouflage; however, their scattering properties have not been very well studied. These colors are mainly due to the scattering of the specific small scatterers inside of the cell. In this work we will summarize the theories and the numerical methods used to solve both the scattering problems for one scatterer and a collection of such scatterers. The reflection spectrum of iridophores is shown to depend on both particle orientation and incident angle of the light. The leucophores are shown to be a white Lambertian surface. Therefore, starting from the structure of the cells, we can predict their color appearance in the skin. This work provides a general framework for the study of the structural color of cephalpods, and can be applied to many species with different cell structures.

DEDICATION

To my family, teachers and friends

ACKNOWLEDGEMENTS

First of all, I would like to thank my advisor, George Kattawar, for his guidance and encouragement during these years. His sincerity and enthusiasm had inspired my life in many ways. It's a really wonderful journey working with Dr. K.

I would like to thank Roland Allen, Edward Fry and Ping Yang for being my committee members and helping with my research. I would also like to thank Dr. Yang for teaching two classes on light scattering, which greatly benefited my research, and I appreciate all his advice on both my research and career. I also very appreciate Roland Allen for accepting me into his group when I just started as a graduate student and for his advice and encouragement.

Many thanks to our MURI group: Molly Cummings, Alexander Gilerson, James Sullivan, Michael Twardowski, Heidi Dierssen, and many others! They broadened my horizon in research. I also appreciate the financial support from the ONR MURI program under contracts N00014-09-1-1054, of which Dr. Kattawar is the Co-PI.

Thank Roger Hanlon and his group in MBL at Woods Hole: Lydia Mäthger, Alan Kuzirian, Stephen Senft, and George Bell. They shared their precious data with me and helped me understand the real biological system.

Thank our team members in Dr. K's group: You Yu, Lei Bi, Ben Stryker, Dong Sun, Xin Huang, Angela Marotta, Bingqiang Sun, Dayou Chen, and Zhaokai Meng, and also Dr. Yang's whole group, with whom we studied light scattering together. I would also like to thank Xiang Zhou, Zhibin Lin and Chenwei Jiang for the wonderful days we worked together with Dr. Allen. Xiang shared lots of his wisdom with me on how to do research and also on how to use a Mac.

Special thanks to Yu You and Xingbo Zhao for helping me and my wife settle down in College Station. Yu also encouraged me to join Dr. K's group, and helped me get into this new field. Thank Pengwang Zhai for his 3d Monte Carlo code. I learned the Monte Carlo method from reading his code line by line, and its elegance and accuracy set the standard for my programming. Many thanks to my friends: Xiongjun Liu, Shuai Yang, Kai Wang, Xiang Zheng and many others, with whom we enjoyed our lives together in College station.

Thank my English teacher, Sema Pulak, for her trust and efforts on improving my English. Also thanks to Angela Marotta for correcting my English. Thank Dr. K and Angela again for carefully proofreading this dissertation.

Finally, thank my parents, Huishan Gao and Jinfeng Meng, for their support and trust during all these years. Thank my wife, Jing Liu, for her love and care, and for sharing the journey with me.

TABLE OF CONTENTS

LIST OF FIGURES

1. INTRODUCTION

Cephalopods have a quick and accurate camouflage ability to match the color, pattern, and intensity of their background [1]. This ability relies on their highly sophisticated skin structure, which normally includes chromatohores, iridophores and leucophores, as shown in Figure 1.1. A chromatophore cell is a collection of pigmented granules, and its color is due to the selected absorption of the pigments for different wavelengths. The color of iridophores and leucophores is mainly due to the scattering of their specific small structures inside of the cell with negligible absorption effects. As shown in the middle layer of Figure 1.1, an iridophore contains a collection of layered structures, called iridosomes, which can produce color through coherent interference [2]. As shown in the bottom layer of Figure 1.1, a leucophore contains a collection of near-spherical structures, called leucosomes, which usually have a large refractive index [2]. The motivation for this study is to understand the physics of the camouflage mechanism from the microscopic cell strctures, which will benefit both our understanding of the optical principles, and the applications to biology and engineering.

Although the structural color can be easily observed, their optical properties have not been well studied. Previous research has tended to oversimplify the system structures. For a single iridosome, it is usually modeled as a layered film with an infinite spatial extent, and the multiple scattering between the iridosomes is neglected [3, 4, 5, 6]. But the actual iridosomes have a wide range of sizes. The thickness of plates in the iridosome is very thin, around $50 - 200nm$ [7, 8, 9, 10, 11, 12, 13]. But the length of the iridosome plates can be as large as $200 - 300\mu m$ and width $50\mu m$ for some species of squid, such as *Loligo vulgaris* and *Alloteuthis subulata* [14, 8]

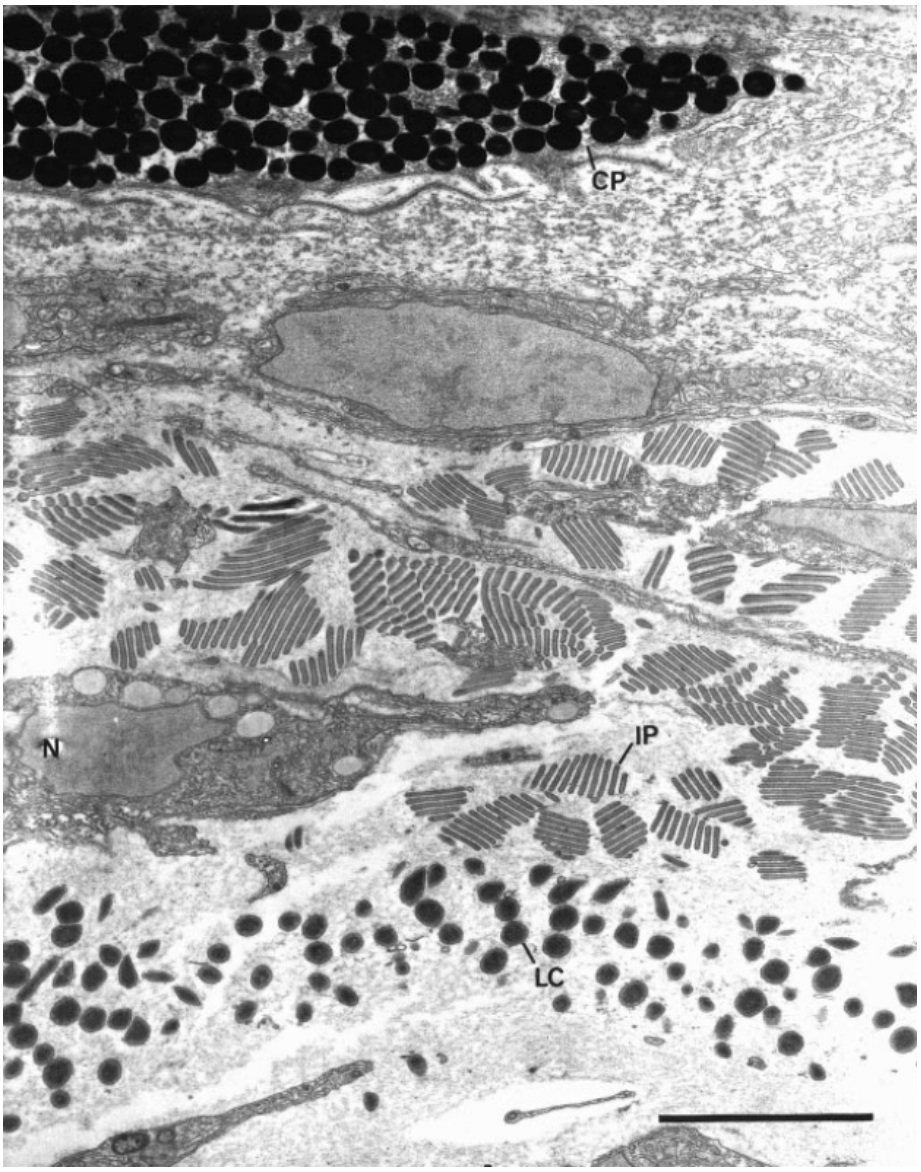

Figure 1.1: Electron micrograph of a vertical section in the skin of *Octopus vulgaris* (from Froesch and Messenger [7]).The skin layers from top to bottom are chromatophore, iridophore, and leucophore. The scale bar is $5\mu m$.

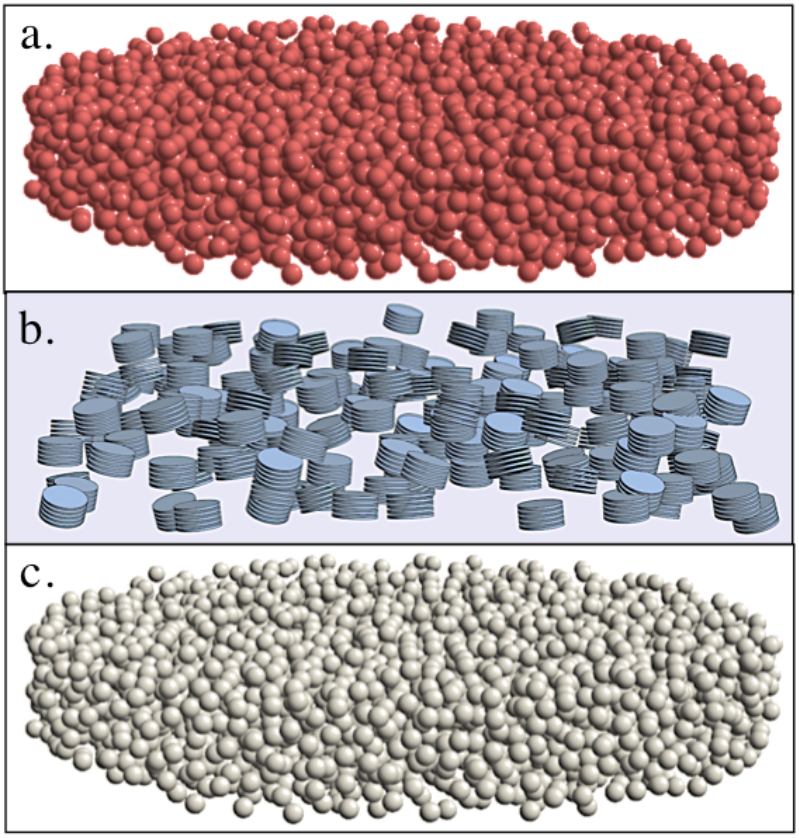

Figure 1.2: Modeled cephalpod skin with the same sequence of cells as shown in the electron micrograph: chromatophore (a), iridophore (b), and leucophore (c)). The structural color is produced by iridophore (b) and leucophore (c).

and *Loligo pealeii* [15]. However, for some other species, the radius can be as small as $1\mu m$, such as *Octopus dofleini* [10, 11] and *Octopus vulgaris* [7]. Therefore, the scattering properties of an iridosome with different sizes need to be studied. For leucophores, they are usually treated as a white Lambertian background without any microscopic structures [5, 6] . But as shown in Figure 1.1, each leucosome has a radius around $0.5\mu m$. By studying the scattering from leucosomes, we can understand how the white Lambertian reflection can be produced.

To understand the structural color, we will conduct an ab initio simulation on both the leucophore and iridophore cells. The modeled geometry of the cells is based on the electron micrographs from the literature [7, 10, 11] as shown in Figures 1.2 (b) and (c). Leucosomes are modeled as spheres, and iridomes are modeled as layered cylinders with a finite radius. We will study both the single scattering properties of an iridosome and a leucosome, and the multiple scattering properties of a collection of iridosomes and leucosomes. Therefore, starting from the structure of their cell, we can predict their color appearance in the skin. This work will provide a general framework on the study of the structural color of cephalpods, and can be applied to many species with different cell structures.

The physics of the structural color depends on both the single and multiple scattering processes. In this work, we will first discuss the theories and the numerical methods to solve these scattering problems. In Section 2, we will introduce the language to describe these scattering processes—the Stokes vector and Mueller matrix formalism. All our following discussions will be based on this formalism. In Section 3, we will introduce the methods to study the electromagnetic scattering of a single scatterer (single scattering); in Section 4, we will discuss the scattering between a collection of scatterers (multiple scattering). A Monte Calro code to solve this problem will be developed based on the theory developed in this section. Finally, in

Section 5, we will apply these methods to study several examples of the leucophore and iridophore cells. Conclusions will be provided in Section 6.

2. STOKES VECTOR AND MUELLER MATRIX FORMALISM

Light scattering is a complex process. To conveniently describe the scattered light field, we chose a four-dimensional real vector, called the Stokes vector, to represent it. All the intensity and the polarization information is included in this vector. Correspondingly, a real 4×4 matrix, called the Mueller matrix, is used to connect the incident Stokes vector and the scattered Stokes vector. Thus, this matrix contains all the scattering information of a scatterer undergoing elastic scattering [16, 17, 18].

We will use this Stokes vector and Mueller matrix formalism to discuss the scattering problem in this work. Both the mathematical treatment and the numerical simulation in the following sections are based on this formalism. There are two main kinds of scattering problems that will be introduced in the next two sections: the single scattering and multiple scattering problems. The single scattering problem studies the electromagnetic scattering of a single scatterer, which can be solved by using Maxwell equations. And the multiple scattering problem studies the incoherent scattering by a collection of particles. The differences in using Stokes vector and Mueller matrix between solving single and multiple scattering problems will be discussed in this section [19].

Under this formalism, the scattering and extinction cross sections will be introduced to describe the overall scattering and absorption properties. They are also important quantities to connect the single and multiple scattering studies. For spherical particles, the optical theorem is established to connect the extinction cross section with the forward scattering field. But when the particle is non-spherical, its extinction cross section could depend on the incident polarized state. In this case, we will introduce a matrix, called the extinction matrix, to describe this phenomenon

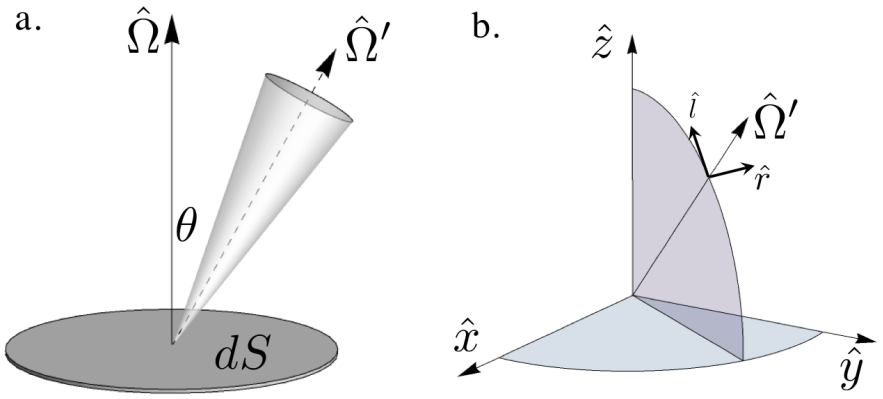

Figure 2.1: (a) The radiance is shown along direction $\hat{\Omega}'$, across an area dS with normal direction $\hat{\Omega}$. θ is the angle between $\hat{\Omega}$ and $\hat{\Omega}'$. (b) The electric field can be expanded into two components perpendicular ($\hat{r}$) and parallel ($\hat{l}$) to the principal plane: $\hat{l} = \mathbf{e}_\theta$, $\hat{r} = -\mathbf{e}_\phi$ and $\hat{\Omega}' = \hat{r} \times \hat{l}$.

[20]. Additionally, a generalization of the optical theorem will also be discussed.

2.1 Radiometric Quantities

Several radiometric quantities will be introduced in this section. They connect the theoretical results with the measured light field. Among these quantities, radiance is the most fundamental quantity in radiometry, which can describe the angular and spatial distribution of the measured light field [21].

Radiance I_ν is defined as the energy in a specified frequency interval $(\nu, \nu + d\nu)$, across an element of area dS in the direction confined to a solid angle $d\Omega'$, during a time dt (Figure 2.1(a)):

$$I_\nu(\Omega', \mathbf{r}) = \frac{d^4 E_\nu}{\cos\theta \; d\nu dS d\Omega' dt} \tag{2.1}$$

where $\mathbf{r}$ defines the field position; θ is the angle between the surface normal direction $\hat{\Omega}$ and the radiance direction $\hat{\Omega}'$. Since all our following discussions are for a specific frequency, we will neglect subscript ν in the notations.

Another quantity, irradiance F represents the flux density across an unit area. It can be obtained as the integral of the radiance over the solid angles of interest:

$$F = \int_{\Omega} I(\Omega) \cos\theta d\Omega. \tag{2.2}$$

Although the energy density u is not easy to measure directly, it can be represented by using radiance [18],

$$u = \frac{1}{c} \int_{4\pi} I(\Omega) d\Omega. \tag{2.3}$$

2.2 Description of Light—Stokes Vector

Any electric field vector of a light beam can be expanded into two perpendicular components: E_l and E_r, which are parallel and perpendicular to a reference plane across the light beam as shown in Figure 2.1 (b). Each component has its own phase and magnitude, and normally both E_l and E_r are represented as complex quantities. To conveniently represent the intensity and polarized state of a beam of light, a real vector, called the Stokes vector $\mathbf{I} = (I, Q, U, V)^T$ [16] is defined as:

$$I =< E_l E_l^* + E_r E_r^* >, \tag{2.4}$$

$$Q =< E_l E_l^* - E_r E_r^* >, \tag{2.5}$$

$$U =< E_l E_r^* + E_r E_l^* >, \tag{2.6}$$

$$V = i < E_l E_r^* - E_r E_l^* >, \tag{2.7}$$

where $<>$ denote a time average; all the 4 components are real, $I > 0$ and $I^2 - Q^2 - U^2 - V^2 \geq 0$.

Note that following the definition above, the Stokes vector has dimensions of ir-

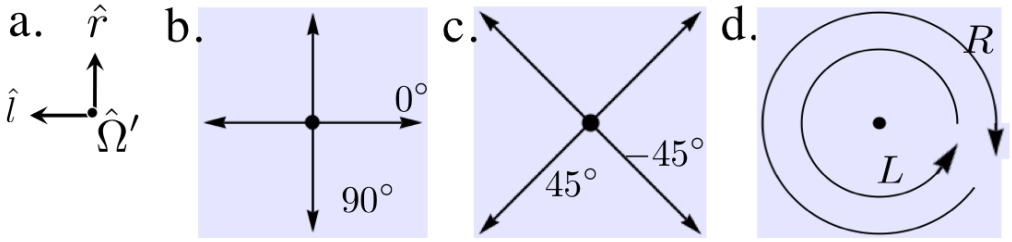

Figure 2.2: (a) The reference frame for light direction $\hat{\Omega}'$ points outward. (b) The direction for polarized direction 0° and 90°, (c) 45° and −45°, and (d) left and right circular polarization.

radiance. When discussing the multiple scattering in a random system, the Stokes vector is generally defined as having dimensions of radiance [19]. More will be discussed in the next section on the Mueller matrix.

The Stokes vector can be measured straightforwardly [16] as:

$$I = I_{0^\circ} + I_{90^\circ} = I_{45^\circ} + I_{-45^\circ} = I_r + I_l, \tag{2.8}$$

$$Q = I_{0^\circ} - I_{90^\circ}, \tag{2.9}$$

$$U = I_{45^\circ} - I_{-45^\circ}, \tag{2.10}$$

$$V = I_R - I_L, \tag{2.11}$$

where I_θ is the intensity of light polarized in the direction of θ, and it can be obtained by rotating a polarizer; $I_{R,L}$ represents the right and left circularly polarized components, as shown in Figure 2.2. The reference frame defined in Figure 2.2 was chosen to be consistent with the one in Figure 2.1 (b).

From the explicit definition of Stokes vector, it is not apparent as to why these particular 4 components were selected, and they are not compact for mathematical manipulation. Here we introduce another form of definitions using Pauli matrices, and in the following sections, we will use them to discuss both the Mueller matrix

and extinction matrix.

To represent the Stokes vector using Pauli matrices, we first denote an arbitrary transformation of the electric field as $\mathbf{A}$. For example, this transformation matrix could be the rotation matrix, or the scattering amplitude matrix (which will be introduced later). After the transformation, we will have the following expressions:

$$(\mathbf{E}^\dagger \mathbf{A}^\dagger)(\mathbf{A}\mathbf{E}) = \mathbf{E}^\dagger \mathbf{B} \mathbf{E}, \tag{2.12}$$

where $\mathbf{B} = \mathbf{A}^\dagger \mathbf{A}$ is a Hermitian matrix; the electric field vector $\mathbf{E}$ is defined as:

$$\mathbf{E}^\dagger = (E_l^*, E_r^*),\ \mathbf{E} = \begin{pmatrix} E_l \\ E_r \end{pmatrix}. \tag{2.13}$$

Since the Pauli matrices and unitary matrix together form a set of complete basis for a Hermitian matrix, we can expand $\mathbf{B}$ as:

$$\mathbf{B} = \frac{1}{2} \sum_{i=1}^{4} \sigma_i Tr(\sigma_i \mathbf{B}), \tag{2.14}$$

where Tr denotes the trace of a matrix, and

$$\sigma_1 = \begin{pmatrix} 1 & 0 \\ 0 & 1 \end{pmatrix}, \sigma_2 = \begin{pmatrix} 1 & 0 \\ 0 & -1 \end{pmatrix}, \sigma_3 = \begin{pmatrix} 0 & 1 \\ 1 & 0 \end{pmatrix}, \sigma_4 = \begin{pmatrix} 0 & -i \\ i & 0 \end{pmatrix}. \tag{2.15}$$

σ_1 is the unitary matrix, and $\sigma_{2,3,4}$ are the Pauli matrices.

From Eq. 2.12, we will have:

$$< \mathbf{E}^\dagger \mathbf{B} \mathbf{E} >= \frac{1}{2} \sum_{i=1}^{4} I_i\ Tr(\sigma_i \mathbf{B}), \tag{2.16}$$

and, therefore, we can construct four real quantities to represent the light field:

$$I_i =< \mathbf{E}^\dagger \sigma_i \mathbf{E} >, \tag{2.17}$$

where I_i corresponds to the ith component of the Stokes vector.

As an example of this definition, we will derive the rotation matrix of the stokes vector. This results will also be used in Section 4 when discussing multiple scattering problems. Rotation of $\mathbf{E}$ counterclockwise by angle θ, the new electric field can be obtained by $\mathbf{E}' = \mathbf{R}\mathbf{E}$ where

$$\mathbf{R} = \begin{pmatrix} cos\theta & -sin\theta \\ sin\theta & cos\theta \end{pmatrix} \tag{2.18}$$

To get the rotated Stokes vectors, we will have:

$$I' = E'^\dagger E' = I \tag{2.19}$$

$$Q' = E'^\dagger \sigma_2 E' = E^\dagger \mathbf{R}^T \sigma_2 \mathbf{R} E = cos2\theta Q - sin2\theta U \tag{2.20}$$

$$U' = E'^\dagger \sigma_3 E' = E^\dagger \mathbf{R}^T \sigma_3 \mathbf{R} E = sin2\theta Q + cos2\theta U \tag{2.21}$$

$$V' = E'^\dagger \sigma_4 E' = E^\dagger \mathbf{R}^T \sigma_4 \mathbf{R} E = V, \tag{2.22}$$

which leads to $\mathbf{I}' = L(\theta)\mathbf{I}$, and

$$\mathbf{L}(\theta) = \begin{pmatrix} 1 & 0 & 0 & 0 \\ 0 & \cos(2\theta) & -\sin(2\theta) & 0 \\ 0 & \sin(2\theta) & \cos(2\theta) & 0 \\ 0 & 0 & 0 & 1 \end{pmatrix}, \tag{2.23}$$

for a counterclockwise rotation of the electric field [16, 22], and for clockwise rotation, simply replace θ by $-\theta$.

2.3 Properties of a Scatterer—Mueller Matrix

When light is scattered by a particle, the incident field will be transformed into a scattered field for each different scattering direction. This transformation can be represented using the scattering amplitude matrix $\tilde{\mathbf{S}}$ [16]:

$$\mathbf{E}_s = \tilde{\mathbf{S}} \cdot \mathbf{E}_0, \tag{2.24}$$

where $\mathbf{E}_0$ is the incident field, $\mathbf{E}_s$ is the scattered filed, and $\tilde{\mathbf{S}}$ is a 2×2 matrix,

$$\tilde{\mathbf{S}} = \begin{pmatrix} \tilde{S}_{11} & \tilde{S}_{12} \\ \tilde{S}_{21} & \tilde{S}_{22} \end{pmatrix}. \tag{2.25}$$

Since the scattering amplitude matrix is generally a complex matrix, it would be convenient to represent it using a real matrix. Following the approach in the last section, the transformation of the incident Stokes vector into the scattered Stokes vector can be denoted using the Mueller matrix,

$$\mathbf{I}_s = \tilde{\mathbf{M}}\mathbf{I}_0. \tag{2.26}$$

It can be represented compactly using Pauli matrices [23] as:

$$\tilde{M}_{ij} = \frac{1}{2} Tr[\sigma_j \tilde{\mathbf{S}}^\dagger \sigma_i \tilde{\mathbf{S}}]. \tag{2.27}$$

For each scattering direction, there will be a different Mueller matrix to describe how the incident light is transformed into the scattered light; therefore, the Mueller

matrix includes all the information about the elastic scattering of a particle.

Generally a Mueller matrix will have a total 16 non-zero elements, but only 7 of them are independent. For a diagonal scattering amplitude matrix, such as the scattering of a spheres, or the scattering with a mirror symmetry, the Mueller matrix can be simplified and can be reduced to only 3 independent elements as follows [16, 17]:

$$\tilde{\mathbf{M}} = \frac{1}{2}\begin{pmatrix} |\tilde{S}_{11}|^2 + |\tilde{S}_{22}|^2 & |\tilde{S}_{11}|^2 - |\tilde{S}_{22}|^2 & 0 & 0 \\ |\tilde{S}_{11}|^2 - |\tilde{S}_{22}|^2 & |\tilde{S}_{11}|^2 + |\tilde{S}_{22}|^2 & 0 & 0 \\ 0 & 0 & 2Re[\tilde{S}_{11}\tilde{S}_{22}^*] & 2Im[\tilde{S}_{11}\tilde{S}_{22}^*] \\ 0 & 0 & -2Im[\tilde{S}_{11}\tilde{S}_{22}^*] & 2Re[\tilde{S}_{11}\tilde{S}_{22}^*] \end{pmatrix} \tag{2.28}$$

For different scattering processes there could be different forms for the expression of $\mathbf{S}$. For the scattering over a semi-infinite plates, the reflected and transmitted waves are both planes waves. We can follow the above definition to get the Mueller matrix. This will be discussed in section 2.5. For a finite size scatterer, the scattered filed at the far field is a spherical wave [16], and the scattering amplitude for the spherical wave $\mathbf{S}$ can be represented as:

$$\mathbf{E}_s = \tilde{\mathbf{S}}\mathbf{E}_0 = \frac{e^{ik(r-z)}}{-ikr}\mathbf{S}\mathbf{E}_0 \tag{2.29}$$

Therefore, the Mueller matrix for a spherical wave only differs from that of a total wave by a dimensionless factor,

$$\tilde{\mathbf{M}} = \frac{1}{k^2r^2}\mathbf{M}, \tag{2.30}$$

where $\mathbf{M}$ can be defined using $\mathbf{S}$ just as we used $\tilde{\mathbf{S}}$ for $\tilde{\mathbf{M}}$:

$$M_{ij} = \frac{1}{2} Tr[\sigma_j \mathbf{S}^\dagger \sigma_i \mathbf{S}]. \tag{2.31}$$

Note that Mueller matrix $\mathbf{M}$ has different definitions for a finite size scatterer and semi-infinite plates.

In multiple scattering studies of small particles described in Section 4, $\mathbf{M}$ is used to transform the radiance rather than irradiance. This was shown starting with the Maxwell equations in the book by Mishchenko [20], or from a phenomenological approach as discussed by Preisendorfer [24]. For the studies of semi-infinite plates in Section 3 and Section 5, we will use $\tilde{\mathbf{M}}$ directly, since both the transmitted field and the reflected field are always plane waves. The studies on semi-infinite plates will be shown in the last section of this section.

2.4 Generalized Optical Theorem—Extinction Matrix

A cross section is a useful concept to describe the interaction effectiveness of a scatterer. During the scattering process, the incident energy can be either scattered or absorpt. The summation of the scattering and the absorption cross sections is defined as the extinction cross section, that is the total extinguished energy divided by the incident energy density [16]. As shown in the Mueller matrix, the angular distribution of the scattered light can be represented by the first element of the Mueller matrix M_{11}, also called the phase function. Therefore, the scattering cross section can be obtained by:

$$C_{sca} = \frac{1}{k^2} \int_{4\pi} M_{11} d\Omega. \tag{2.32}$$

For a spherical particle, the extinction cross section can be associated with the

forward scattered field directly through the optical theorem [17],

$$C_{ext} = \frac{4\pi}{k^2}\Re[S(0)], \tag{2.33}$$

where the scattering angle $\theta_s = 0$ denotes the forward direction, and $S(0) = S_{11}(0) = S_{22}(0)$. Extinction can also be explained from the interference between the forward scattered field and the incident field. To consider the effect of absorption, we can define a quantity called the scattering albedo $\alpha = C_{sca}/C_{ext}$. When there is no absorption in the particle, we will have $\alpha = 1$, and for all other cases: $\alpha < 1$.

For a general non-spherical particle, the extinction cross section would depend on the incident polarization state. This means that for a different incident Stokes vectors, there may be a different extinction cross section, and therefore, a matrix $\mathbf{K}$, called the extinction matrix, is required to fully describe this phenomenon.

If a detector with area D detect the forward scattering of a single particle, the power $\mathbf{P}$ (polarization dependent) incident on the detector would be:

$$\mathbf{P} = \iint\limits_{D,\theta=0} \mathbf{I}_{total}\mathrm{d}S = D\ \mathbf{I}_0 - \mathbf{K}\cdot\mathbf{I}_0 + O(r^{-2}), \tag{2.34}$$

where $\mathbf{I}_{tot}$ denotes the Stokes vector of the total field, and $\mathbf{K}$ denotes the energy removed from the forward direction. Similar to the approach used to derive the Mueller matrix, we can derive the extinction matrix using the Pauli matrices,

$$K_{ij} = \frac{\pi}{k^2}Tr[\sigma_j(S^\dagger\sigma_i + \sigma_i S)]_{\theta=0}, \tag{2.35}$$

where $\mathbf{S}$ is the scattering amplitude matrix of a small scatterer (Eq. 2.29). This extinction matrix is for the scattering of a small scatterer. The extinction matrix of

semi-infinite plates will be discussed in the next section, where a similar derivation of $\mathbf{K}$ for semi-infinite plates will be provided in detail. Explicitly $\mathbf{K}$ can be expressed [25, 20] as follows:

$$\mathbf{K} = \frac{2\pi}{k^2} \begin{pmatrix} \Re[S_{11}+S_{22}] & \Re[S_{11}-S_{22}] & 0 & 0 \\ \Re[S_{11}-S_{22}] & \Re[S_{11}+S_{22}] & 0 & 0 \\ 0 & 0 & \Re[S_{11}+S_{22}] & \Im[S_{11}-S_{22}] \\ 0 & 0 & -\Im(S_{11}-S_{22}) & \Re[S_{11}+S_{22}] \end{pmatrix}_{\theta_s=0} \tag{2.36}$$

$$= \begin{pmatrix} C_{ext} & C_{pol} & 0 & 0 \\ C_{pol} & C_{ext} & 0 & 0 \\ 0 & 0 & C_{ext} & C_{cpol} \\ 0 & 0 & -C_{cpol} & C_{ext} \end{pmatrix}. \tag{2.37}$$

Note the first element of the extinction matrix corresponds to the optical theorem. Therefore, we have obtained the generalized optical theorem for an arbitrary incident Stokes vector and for an arbitrary particles. More discussion on the specific extinction properties of iridosomes will be discussed in Section 5.

2.5 Example on the Semi-infinite Plates

As discussed in Section 1, there are iridosomes with very large aspect ratios. If these iridosomes could be treated as semi-infinite plates, their simulation would be much easier. To better understand iridosomes' scattering properties, it's useful to compare their properties with that of semi-infinite plates, and discuss where are the differences come from.

In this section, we will introduce the Mueller matrix and extinction matrix for the semi-infinite plate structure. Its Mueller matrix can be introduced as discussed in section 2.3. But since the scattering from semi-infinite plates is always associated

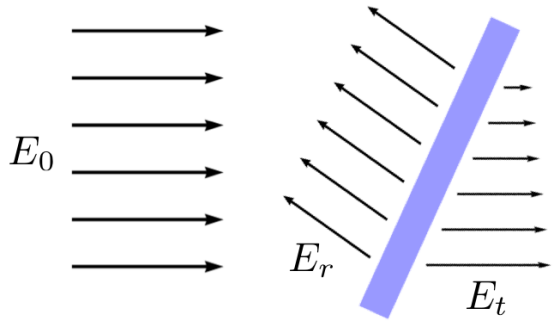

Figure 2.3: Reflection and transmission by a plate.

with plane waves, we will derive the extinction matrix for it in detail and and discuss its differences and similarities with the results for small scatterers. In the next section, we will introduce an exact method, called the transfer matrix method, to solve the electromagnetic scattering of semi-infinite plates. In Section 5, we will discuss the numerical comparison between finite plates and semi-infinite plates.

The reflectivity and trasmissivity of the electric field for multi-layer plates are denoted by r,and t. They are generally complex numbers, and are different for different polarization states. We can decompose the electric field vector in two directions, parallel and perpendicular to the principal plane. For each component, Fresnel formulas (discussed in more detail in the next section) are used to relate the incident and the reflected or transmitted fields (Figure 2.3) as:

$$E_r = rE_0, \tag{2.38}$$

$$E_t = tE_0. \tag{2.39}$$

Due to conservation of energy we have $|E_r|^2 + |E_t|^2 = |E_0|^2$ and $|r|^2 + |t|^2 = 1$.

The two component vector for electric field, as introduced in section 2.3, is used to represented the two polarization states of the electric field. $\mathbf{E}_s$ denotes the scattering field; $\mathbf{E}_r$ and $\mathbf{E}_t$ are the reflected and transmitted field. Note the transmitted field

is a combination of the forward scattered field and the incident field.

The scattering amplitude matrices for the reflected field, total transmitted field and the forward scattered field, are defined respectively, so that

$$\mathbf{E}_r = \tilde{\mathbf{S}}_r \mathbf{E}_0,\ \mathbf{E}_t = \tilde{\mathbf{S}}_t \mathbf{E}'_0,\ \mathbf{E}_f = \tilde{\mathbf{S}}_f \mathbf{E}'_0, \tag{2.40}$$

where

$$\tilde{\mathbf{S}}_r = \begin{pmatrix} r_p & 0 \\ 0 & r_s \end{pmatrix},\ \tilde{\mathbf{S}}_t = \begin{pmatrix} t_p e^{-i\phi} & 0 \\ 0 & t_s e^{-i\phi} \end{pmatrix},\ \tilde{\mathbf{S}}_f = \begin{pmatrix} t_p e^{-i\phi} - 1 & 0 \\ 0 & t_s e^{-i\phi} - 1 \end{pmatrix}. \tag{2.41}$$

Here $\mathbf{E}_t$ and $\mathbf{E}'_0$ are chosen at the same position. Since the transmitted field is a combination of the forward scattered field and the incident field, the forward scattered field can be defined as $\mathbf{E}_f = \mathbf{E}_t - e^{i\phi}\mathbf{E}_0 = \mathbf{E}_t - \mathbf{E}'_0$, where the phase factor $\phi = n_i L \cos\theta_i$, L is the total thickness of the plates, θ_i is the incident angle, and n_i is the refractive index in the medium.

With these scattering amplitude matrices, Mueller matrices for the reflection, transmission and the forward scattering can be defined as in Eq. 2.28. However, for the extinction matrix, we cannot directly use the results for small particles, because its definition follows the results of the spherical wave at the far field. For the scattering of semi-infinite plates, both its near field and far field are plane waves. Therefore, in order to understand their connection, we have to discuss the difference of these formalisms. In the following, we will derive an extinction efficiency matrix for the semi-infinite plates, and finally provide a one layer example to show how the extinction efficiency changes with its thickness.

Extinction is the part of energy removed from the incident and scattered field in

the forward direction. Similar to the discussion on the extinction from the measurement of a detector (Eq. 2.34), in the forward direction:

$$I_{t,i} = \mathbf{E}_t^\dagger \sigma_i \mathbf{E}_t = (\mathbf{E}_s + \mathbf{E}_0')^\dagger \sigma_i (\mathbf{E}_s + \mathbf{E}_0') \tag{2.42}$$

$$= \mathbf{E}_0^{'\dagger} \sigma_i \mathbf{E}_0' + \mathbf{E}_s^\dagger \sigma_i \mathbf{E}_s + \mathbf{E}_s^\dagger \sigma_i \mathbf{E}_0' + \mathbf{E}_0^{'\dagger} \sigma_i \mathbf{E}_s. \tag{2.43}$$

Here we have neglected the symbol for time average. We can rewrite this equation using the Mueller matrix:

$$\tilde{\mathbf{M}}_t \mathbf{I}_0 = \mathbf{I}_0 + \tilde{\mathbf{M}}_s \mathbf{I}_0 - \tilde{\mathbf{Q}} \mathbf{I}_0, \tag{2.44}$$

where the extinction efficiency matrix $\mathbf{Q}$ is defined as:

$$-E_s^\dagger \sigma_i E_0' - E_0^{'\dagger} \sigma_i E_s = \Sigma_j \tilde{Q}_{ij} I_{0j}, \tag{2.45}$$

and can be explicitly expressed as:

$$\tilde{\mathbf{Q}}_{ij} = -\frac{1}{2} Tr[\sigma_j (\tilde{\mathbf{S}}^\dagger \sigma_i + \sigma_i \tilde{\mathbf{S}})] \tag{2.46}$$

Since all the fields are plane waves, their integral around a small area in the forward direction can be obtained by multiplying the field by the area, and eventually this common factor can be canceled. After integrating around the forward direction over an area D, we will have:

$$\int_D dA \tilde{\mathbf{M}}_t = D + \int_D dA \tilde{\mathbf{M}}_s - \tilde{\mathbf{K}}, \tag{2.47}$$

where

$$\tilde{\mathbf{K}}_{ij} = \int_D dA\tilde{\mathbf{Q}}_{ij} = -\frac{1}{2}\int_D dATr[\sigma_j(\tilde{\mathbf{S}}^\dagger\sigma_i + \sigma_i\tilde{\mathbf{S}})] \tag{2.48}$$

Along the forward direction $\mathbf{E}_s = \mathbf{E}_f$, and $\tilde{\mathbf{M}}_s = \tilde{\mathbf{M}}_f$, we have:

$$\tilde{\mathbf{K}}_{ij} = D\tilde{\mathbf{Q}}_{ij} \tag{2.49}$$

$$= -\frac{D}{2}Tr[\sigma_j(\tilde{\mathbf{S}}_f^\dagger\sigma_i + \sigma_i\tilde{\mathbf{S}}_f)]_{\theta_s=0} \tag{2.50}$$

We can also find the connection between the extinction matrix with the extinction efficiency matrix for the plates:

$$\tilde{\mathbf{Q}} = 1 + \tilde{\mathbf{M}}_f - \tilde{\mathbf{M}}_t, \tag{2.51}$$

where $\mathbf{M}_f$ and $\mathbf{M}_t$ are the Mueller matrices for the forward scattered field and the total transmitted field, respectively. The expression for extinction efficiency $\mathbf{Q} = \mathbf{K}/D$ can be shown explicitly to be:

$$\tilde{\mathbf{Q}} = -\begin{pmatrix} Re[\tilde{S}_{11}+\tilde{S}_{22}] & Re[\tilde{S}_{11}-\tilde{S}_{22}] & 0 & 0 \\ Re[\tilde{S}_{11}-\tilde{S}_{22}] & Re[\tilde{S}_{11}+\tilde{S}_{22}] & 0 & 0 \\ 0 & 0 & Re[\tilde{S}_{11}+\tilde{S}_{22}] & Im[\tilde{S}_{11}-\tilde{S}_{22}] \\ 0 & 0 & -Im(\tilde{S}_{11}-\tilde{S}_{22}) & Re[\tilde{S}_{11}+\tilde{S}_{22}] \end{pmatrix}_{\theta_s=0}. \tag{2.52}$$

We can define three independent parameters: Q_{ext}, Q_{pol} and Q_{cpol}, and therefore the

extinction efficiency matrix can be denoted as,

$$\tilde{\mathbf{Q}} = \begin{pmatrix} Q_{ext} & Q_{pol} & 0 & 0 \\ Q_{pol} & Q_{ext} & 0 & 0 \\ 0 & 0 & Q_{ext} & Q_{cpol} \\ 0 & 0 & -Q_{cpol} & Q_{ext} \end{pmatrix}. \tag{2.53}$$

Suppose there is no absorption in the particle, then the extinction efficiency will be equal to the scattering efficiency. We can derive the scattering efficiency using the amplitude of the reflected and transmitted field, and discuss the way the extinction efficiency for unpolarized light changes. The scattering efficiency for unpolarized incident light can be represented as:

$$Q_s = \frac{|E_t - E_i'|^2 + |E_r|^2}{|E_0|^2} \tag{2.54}$$

$$= \frac{(|E_t|^2 + |E_r|^2) + |E_i'|^2 - 2Re(E_t \cdot (E_i')^*)}{|E_0|^2} \tag{2.55}$$

$$= 2 - 2\frac{Re(E_t \cdot (E_i')^*)}{|E_0|^2} \tag{2.56}$$

$$= 2 - 2Re(t \cdot e^{-i\phi}) \tag{2.57}$$

Since $|t| \leq 1$, we will have $-1 \leq Re(t \cdot e^{-i\phi}) \leq 1$, and $0 \leq Q_s \leq 4$. The extinction efficiency can vary from 0 to 4, but cannot be larger than 4. The behavior of the extinction efficiency is solely determined by the factor of $Re(t \cdot e^{-i\phi})$, which indicates the interference between the incident light and the forward scattered field.

In Section 5, detailed numerical comparison between the semi-infinite and finite size iridosomes will be given. Here we will consider a single layer plate as an example

to understand how the extinction efficiency changes with its thickness:

$$\tilde{Q}_{ext} = -Re[\tilde{S}_{11} + \tilde{S}_{22}] \tag{2.58}$$

$$= 2 - Re[t_l e^{-i\phi} + t_r e^{-i\phi}], \tag{2.59}$$

where the reflection t can be found using the transfer matrix method, as discussed in the next section:

$$t = \frac{t_{12}t_{21}e^{i\phi_b}}{1 + r_{12}r_{21}}, \tag{2.60}$$

for each polarization component. There are two phase factors defined as $\phi_b = nkd\cos\theta_b$, $\phi = kd\cos\theta_i$, where θ_b is the refractive angle in the plate; θ_i is the incident angle; d is the thickness of the plate.

For normal incidence $r_p = r_s$ and $t_p = t_s$, $\theta_b = 0$, and the symmetry relation between r_{12} and r_{21}, t_{12} and t_{21}.

$$t_{12} = \frac{2n_1}{n_2 + n_1} = \frac{2}{n_r + 1}, \tag{2.61}$$

$$t_{21} = \frac{2n_2}{n_1 + n_2} = \frac{2n_r}{n_r + 1}, \tag{2.62}$$

$$r_{12} = \pm\frac{n_2 - n_1}{n_2 + n_1} = \pm\frac{n_r - 1}{n_r + 1}, \tag{2.63}$$

$$r_{21} = r_{12}, \tag{2.64}$$

for both the $\hat{l}$ and $\hat{r}$ components. For the reflectance the plus sign is for the parallel component and the minus sign is for the perpendicular component.

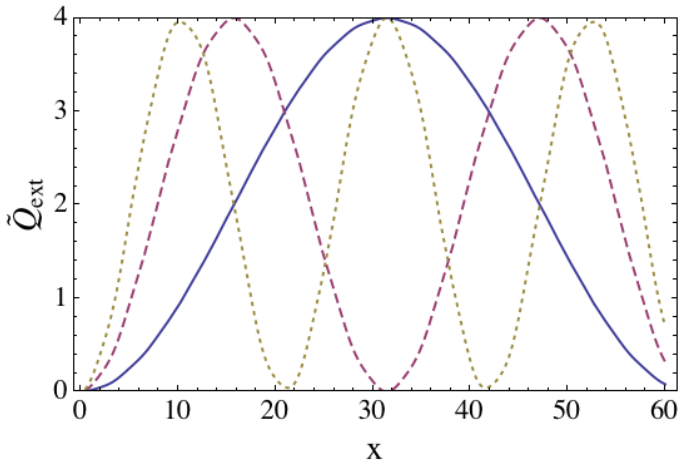

Figure 2.4: Extinction efficiency vs size parameter ($x = kd$) of the plate thickness with three relative refractive indices $n_r = 1.1$ (Solid), 1.2 (Dashed), and 1.3 (Dotted).

Therefore, the extinction efficiency can be found as:

$$\tilde{Q}_{ext} = 2 - 2Re[\frac{4n_r e^{i(\phi_b - \phi)}}{(n_r+1)^2 - (n_r-1)^2 e^{-2i\phi_b}}] \tag{2.65}$$

$$= 2Re(1 - \frac{4n_r e^{i(n_r-1)kd}}{(n_r+1)^2 - (n_r-1)^2 e^{-2ikd}}) \tag{2.66}$$

We defined the size parameter $x = kd$. The variation of the extinction efficiency with the size parameter for several relative refractive indices is shown in Figure 2.4. Extinction efficiency is shown as a periodic function of the size parameter.

3. SINGLE SCATTERINGS METHODS

As discussed in Section 1, there are two main kinds of scatterers in the skin of cephalopods, namely leucosomes and iridosomes. Leucosomes are highly spherical and can be modeled as spheres. Iridosomes can be approximately modeled as layered plates. When light enter the skin, it will be scattered multiple times by numerous iridosomes and leucosomes. The overall reflectance depends predominantly on how an individual iridosome or leucosome scatters light. In this section we will introduce the so-called single scattering methods, which will solve the electromagnetic scattering problem based on Maxwell equations. The resulting scattering properties, such as the albedo, the extinction cross section, and the scattering Mueller matrix, will be used as the input for multiple scattering simulations, which will be the topic of the next section.

There are three basic shapes for leucosome and iridosome modeling described in Figure 3.1. The scattering solutions of each of these shapes will be discussed in this section. Figure 3.1 (a) shows a solid sphere as a model for a leucosome, which can be solved by using the Lorenz-Mie theory (LMT). Figures 3.1 (b) and (c) are both multiple layer plates, one with finite radius and another with infinite radius.

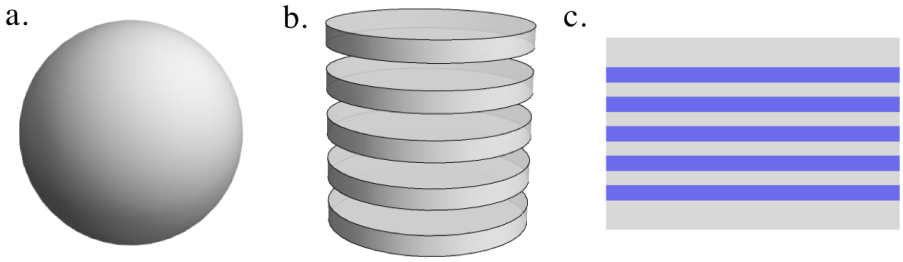

Figure 3.1: Three shapes modeled in this study: (a) a single sphere, (b) a finite size layered plate, and (c) a representation of the semi-infinite plates, which is similar to (b) but with an infinite radius; gray region denotes the medium.

Both can be used as approximations for iridosomes depending on their aspect ratio (a detailed discussion will be provided in Section 5). When the plates have a finite radius (Figure 3.1 (b)), their scattering properties can be solved by using the Discrete Dipole Approximation(DDA) method. When their radius is infinite, they become semi-infinite plates (Figure 3.1 (c)) and their analytical solution can be obtained through the transfer matrix method (TMM). The application of these methods will be discussed in Section 5. In this section, we will only briefly discuss the LMT theory and the DDA method, since for both methods, there are well tested and documented numerical codes available. We will discuss the TMM in more detail, since will study several scattering effects based on this method.

Before discussing the theory of the single scattering method, we will summarize the inputs and the outputs for each method. The inputs are the necessary quantities required by the these methods in order to produce valid results; the output physical quantities are the ones we intend to solve for. The input information includes the shape, size, and refractive index of the scatterer, the refractive index of the medium (non-absorptive), and the wavelength of the incident light (plane wave). Several scattering quantities will be calculated, which include the single scattering albedo, the extinction cross section, and the Mueller Matrix (for each scattering direction), which are quantities necessary for multiple scattering simulations. There are also several auxiliary quantities which indicate the characteristics of single scattering properties. We will frequently use these quantities to analyze and verify the numerical results. They include the backscattering, scattering, and absorption cross sections (or efficiencies), and the asymmetry factor (g factor). Note that except for the extinction cross section (or absorption cross section), all other quantities can be calculated from the unnormalized phase function.

3.1 Lorenz-Mie Theory (LMT)

The electromagnetic scattering of a plane wave off a solid sphere can be elegantly solved by using Lorenz-Mie theory. This solution was independently discovered by Danish physicist Ludvig Lorenz in 1898 and by German physicist Gustav Mie in 1908 [16]. In this section, we will review the essential treatment of the Lorenz-Mie theory (LMT). For the numerical simulation, we will use BHMIE code (provided in Appendix A of Bohren-Huffman's book [16], and modified by B.T.Draine). This code has been well documented and tested. For a more detailed history and application of LMT, please refer to the book by Wolfram Hergert and Thomas Wriedt [26].

Consider a sphere with radius a and refractive index m relative to the background material (non-absorptive). The wavelength of the incident light in the medium is λ, and the wavenumber is defined as $k = 2\pi/\lambda$. We will use the size parameter to represent the size of the sphere, which is defined as $x = ka$. Size parameter has a very clear physical meaning—it measures the phase change of the incident light across the radius of the particles.

In Lorenz-Mie theory, the solutions of the vector wave equation for the electromagnetic waves in free space are constructed using the solution of the scalar wave equations. When the sphere is presented, the internal (inside the sphere) and external (outside the sphere) solutions can be found using the free space results. By connecting these two sets of solutions using the boundary conditions at the sphere interface, the final solutions for the sphere scattering can be obtained [16]. Here we will briefly review these procedures.

From Maxwell equations, the vector wave equations for both the electric and

magnetic field can be derived as:

$$\nabla^2\mathbf{E} + k^2\mathbf{E} = 0, \tag{3.1}$$

$$\nabla^2\mathbf{H} + k^2\mathbf{H} = 0, \tag{3.2}$$

where k is the wavenumber in the medium as defined previously.

The solution of these two vector wave equations can be constructed through the solution of a scalar wave equation as follows:

$$\mathbf{M} = \nabla \times (\mathbf{r}\psi), \tag{3.3}$$

$$\mathbf{N} = \frac{\nabla \times \mathbf{M}}{k}, \tag{3.4}$$

where ψ is the solution of the scalar wave equation:

$$\nabla^2\psi + k^2\psi = 0. \tag{3.5}$$

This scalar wave equation (Eq. 3.5) can be solved by using the separation of variables method [27]. As we have discussed, the final solution of the scattering by a solid sphere can be obtained by connecting the internal and external fields using the boundary conditions. Therefore, we can solve the final scattering amplitude matrix (as introduced in Section 2) at the far field for every scattering direction:

$$S_1 = \sum_n \frac{2n+1}{n(n+1)}(a_n\pi_n + b_n\tau_n), \tag{3.6}$$

$$S_2 = \sum_n \frac{2n+1}{n(n+1)}(a_n\tau_n + b_n\pi_n), \tag{3.7}$$

where a_n and b_n are defined as:

$$a_n = \frac{m\psi_n(mx)\psi_n'(x) - \psi_n(x)\psi_n'(mx)}{m\psi_n(mx)\xi_n'(x) - \xi_n(x)\psi_n'(mx)}, \tag{3.8}$$

$$b_n = \frac{\psi_n(mx)\psi_n'(x) - m\psi_n(x)\psi_n'(mx)}{\psi_n(mx)\xi_n'(x) - m\xi_n(x)\psi_n'(mx)}. \tag{3.9}$$

Here the prime superscript denotes first order differentiation with respect to the argument of the function, and τ_n and π_n are defined as:

$$\pi_n = \frac{P_n^1}{\sin\theta},\ \tau_n = \frac{dP_n^1}{d\theta}, \tag{3.10}$$

where P_n^1 is the associated Legendre function of the first kind of degree n and order 1, and θ is the scattering angle relative to the incident direction. To introduce a_n and b_n, we have used the Riccati-Bessel functions:

$$\psi_n(\rho) = \rho j_n(\rho),\ \xi_n(\rho) = \rho h_n^{(1)}(\rho), \tag{3.11}$$

where j_n is the spherical Bessel function, and $h_n^{(1)}$ is the spherical Hankel function of the first kind.

The solutions of S_1 and S_2 (Eqs. 3.7 and 3.6) involves the summation over the index n. An efficient method to determine the maximum number of required terms (n_c) in the summation is provided by Wiscombe [28], where n_c is given by

$$n_c = x + 4x^{1/3} + 2. \tag{3.12}$$

Note n_c is a function of the size parameter x. More discussion on n_c and the stability of the numerical algorithm can be found in Appendix A of the book by Bohren & Huffman ([16]).

Following the discussion in the previous section, the Mueller matrix can be obtained straightforwardly from the scattering amplitude matrix. The expression for the scattering and extinction cross sections can be represented using a_n (Eq. 3.8) and b_n (Eq. 3.9):

$$C_{sca} = \frac{2\pi}{k^2} \sum_{n=1}^{\infty} (2n+1)(|a_n|^2 + |b_n|^2), \tag{3.13}$$

$$C_{ext} = \frac{2\pi}{k^2} \sum_{n=1}^{\infty} (2n+1) Re(a_n + b_n). \tag{3.14}$$

The extinction efficiency is defined as the ratio of the extinction cross section and the geometric cross section:

$$Q_{ext} = \frac{C_{ext}}{\pi a^2} \frac{2}{x^2} \sum_{n=1}^{\infty} (2n+1) Re(a_n + b_n). \tag{3.15}$$

One of the consequences of the Lorenz-Mie solution is the so called extinction paradox:

$$\lim_{x \to \infty} Q_{ext}(x, m) = 2, \tag{3.16}$$

where x is the size parameter, m is the refractive index. This result shows the total extinction energy, which includes both scattering and absorption energy, is twice of the energy blocked by the geometric cross section. This gives us the impression that more energy is removed than the particle receives. The total wave in the forward direction is a combination of the incident wave and the forward scattered wave. The paradox can be explained by the interference effect in the forward direction between these two waves. There will be more discussions on this using plates as example in Section 5.

3.2 Discrete Dipole Approximation Method (DDA)

A macroscopic material involves a huge number of molecules on the order of Avogadro's constant ($N_A = 6.02 \times 10^{23}$). Under incident radiation, each molecule in the material will undergo forced oscillation and radiate by itself. Its subsequent radiation will act on all the other molecules, and make every molecule in the material couple to all the others. The total number of coupling during the scattering process will be on the order of N_A^2 — an inordinately large number for any feasible numerical simulations.

In 1973, Purcell and Pennypacker proposed a plausible way for such a simulation [29], called the Discrete Dipole Approximation(DDA). They used an effective dipole which averages over a large number of molecules in a small volume, to replace the single molecular dipole in the formalism. The total number of effective dipoles (N) can be greatly reduced from the earlier estimate to a range between 10^4 and 10^8 dipoles, which make the numerical simulation feasible for a particle with a reasonable sizes (the size will be discussed later). For example, Figure 3.2 provides an actual DDA model for a 5 layer leucosome (shown in Figure 3.1 (b)) with diameter $1\mu m$ and one layer thickness $0.1\mu m$. There are 12 dipoles along this thickness and a total 470580 dipoles for the whole scatterer. This model is used for the simulation in Section 5.

In 1980s, Draine and Flatau developed a DDA code called DDSCAT [30, 31]. which is widely used. In a later development, the DDSCAT can also be used to simulate scattering with periodic boundary conditions [32]. For a fairly large particle, the DDA method still requires a large amount of computer memory and many CPUs. DDSCAT has been parallelized for particles with random orientations, while for a single particle the memory requirements restrict it to a size parameter 25 [33].

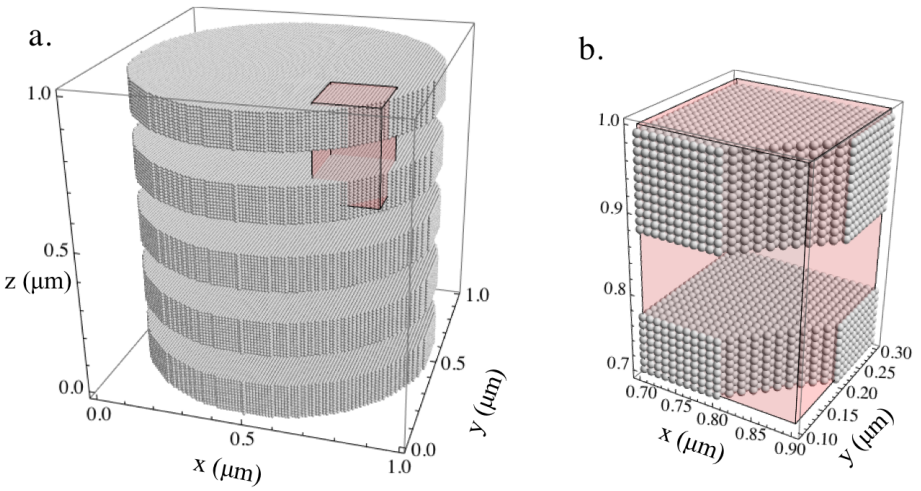

Figure 3.2: (a) A DDA model for the finite size plates. (b) An enlarged image of the region in the red box of (a).

Yurkin and Hoekstra parallelized the DDA method for the computation of both single particle and random orientations with the size parameter extended to more than 100 [34]. We will use ADDA for most of our simulations, and use DDSCAT to calculate the scattering properties of a system with periodic boundary conditions as discussed in the next section.

Here we will briefly review the DDA theory. As discussed in the beginning of this section, a particle is discretized into a cubic lattice with N effective dipoles and an inter-dipole distance d. Each one is an average over all the molecules in a small volume ($V = d^3$). The effective dipole polarization $\mathbf{P}_i$ at lattice size i can be obtained as:

$$\mathbf{E}_j^{ext} = \mathbf{E}_j^{inc} - \sum_{k \neq j} \bar{\mathbf{G}}_{jk} \mathbf{P}_k, \tag{3.17}$$

$$\mathbf{P}_j = \bar{\alpha}_j \mathbf{E}_j^{ext}, \tag{3.18}$$

where $\bar{\alpha}_j$ is the polarization tensor at site j, $\mathbf{E}_j^{ext}$ is the total electric field—it include

the incident plane wave $\mathbf{E}_j^{inc}$ at site j and the induced electric field due to all other effective dipoles. The induced electric field is described by the interaction matrix $\bar{\mathbf{G}}_{jk}$ which connects the site j and k. It can be obtained analytically [35]. Following the notation of Yurkin [34], the interaction matrix can be represented by:

$$\bar{\mathbf{G}}_{jk} = \frac{\exp(ikR)}{R}\left[k^2(\bar{\mathbf{I}} - \frac{\hat{R}\hat{R}}{R^2}) - \frac{1-ikR}{R^2}(\bar{\mathbf{I}} - 3\frac{\hat{R}\hat{R}}{R^2})\right], \tag{3.19}$$

where $\mathbf{r}_j$ is the vector to the lattice site j, $\mathbf{R} = \mathbf{r}_j - \mathbf{r}_k$, $R = |\mathbf{R}|$ and $(\hat{R}\hat{R})_{ij} = R_i R_j$.

The polarizability $\bar{\alpha}_j$ is important in connecting the effective dipole and the macroscopic properties. Its first order approximation can be obtained through the Clausius-Mossotti (CM) relation [30]:

$$\bar{\alpha}_j^{CM} = \frac{1}{n_d}\frac{3}{4\pi}\frac{\bar{\epsilon}_j - 1}{\bar{\epsilon}_j + 2}, \tag{3.20}$$

where $n_d = 1/d^3$ is the number density of dipoles, and $\bar{\epsilon}_j$ is the permittivity tensor at lattice site j. Several corrections for this polarizability have been introduced, and can be chosen during the numerical simulation depending on the specific problems [34].

To solve Eq. 3.18, we can write it into a more compact form:

$$\sum_{k=1}^{N} \mathbf{G}_{jk}\mathbf{P}_k = \mathbf{E}_j^{inc}, \tag{3.21}$$

where $\mathbf{G}_{jj} = \bar{\alpha}_j^{-1}$. Since both $\mathbf{E}^{inc}$ and $\mathbf{G}$ are known, $\mathbf{P}$ can be obtained by solving N linear equations. All the scattering quantities, including the Mueller matrix and cross sections can be represented using $\mathbf{P}$ [34].

3.3 Transfer Matrix Method (TMM)

For a multiple layer plate with infinite radius, as shown in Figure 3.1 (c), light can be reflected an infinite number of times between the two interfaces of the plates. To solve for its overall reflection and transmission, the Transfer Matrix Method (TMM) provides an efficient way to do this, and can easily be extended to a plate with a large number of layers [36, 37, 38]. In this section, we will first introduce the transfer matrices for an interface connecting two materials with different refractive indices, and then get the transfer matrix for the free propagation between two interfaces. By combining the transfer matrices for all the interfaces and the spaces between them, we can get the solution for a plate with an arbitrary number of layers. This method has been widely used in the study of a photonic lattice [36]. Following the theory discussed in this section, we developed a numerical code for all the calculations regarding semi-infinite multiple layer plates.

3.3.1 Fresnel Formulas

The reflection and transmission of the electric field at a dielectric interface can be solved using the boundary conditions of Maxwell equations, and are summarized in the following Fresnel Formulas [39]. The reflection and transmission for the parallel(p) and perpendicular(s) electric field components can be represented as:

$$r_p = \frac{\tan(\theta_i - \theta_t)}{\tan(\theta_i + \theta_t)}, \qquad r_s = -\frac{\sin(\theta_i - \theta_t)}{\sin(\theta_i + \theta_t)}, \tag{3.22}$$

$$t_p = \frac{2\sin\theta_t \cos\theta_i}{\sin(\theta_i + \theta_t)\cos(\theta_i - \theta_t)}, \qquad t_s = \frac{2\sin\theta_t \cos\theta_i}{\sin(\theta_i + \theta_t)}, \tag{3.23}$$

and from Snel's law of refraction, we have:

$$\frac{\sin\theta_i}{\sin\theta_t} = \frac{n_2}{n_1}, \tag{3.24}$$

θ_i is incident angle in medium 1 with refractive index n_1, and θ_t is the refracted angle in medium 2 with refractive index n_2; the relative refractive index is $n_r = n_2/n_1$.

For the normal incidence case, $\theta_i = \theta_t = 0$, the Fresnel formulas can be simplified to:

$$r_p = \frac{n_r - 1}{n_r + 1}, \qquad r_s = -\frac{n_r - 1}{n_r + 1}, \tag{3.25}$$

$$t_p = \frac{2}{n_r + 1}, \qquad t_s = \frac{2}{n_r + 1}. \tag{3.26}$$

Therefore, the reflectivity and transmissivity of the energy flux (irradiance) can be obtained as:

$$R = \left(\frac{n_r - 1}{n_r + 1}\right)^2, \qquad T = \frac{4n_r}{(n_r + 1)^2}, \tag{3.27}$$

where $R + T = 1$; energy is conserved.

3.3.2 Scattering Matrix and Transfer Matrix

We have introduced the scattering amplitude matrix in Section 2, which associates the scattered light with the incident light for either scattered plane waves or spherical waves. The scattering matrix ($\mathbf{S}$) we are introducing here has the same meaning as the scattering amplitude matrix for plane waves. With this scattering matrix, we can solve for the transfer matrix ($\mathbf{T}$), which connects the electric field at the two boundaries of the system [36].

For the boundary between two materials 1 and 2 shown in Figure 3.3 (a), the scattering matrix is defined as:

$$\begin{pmatrix} E_2^{(+)} \\ E_1^{(-)} \end{pmatrix} = \mathbf{S}_{21} \begin{pmatrix} E_1^{(+)} \\ E_2^{(-)} \end{pmatrix} \tag{3.28}$$

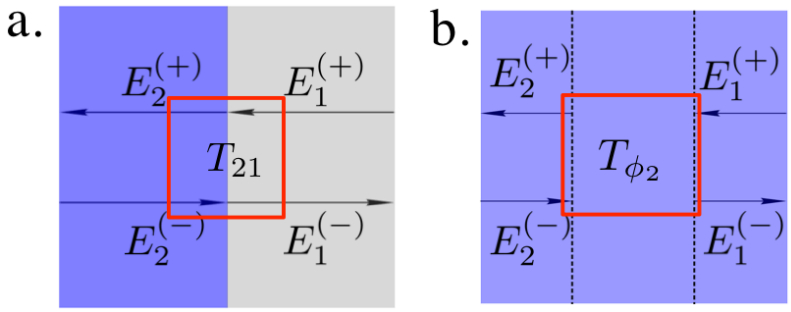

Figure 3.3: Incident light are denoted by $E_1^{(+)}$ and $E_2^{(-)}$, which can be related to $E_1^{(-)}$ and $E_2^{(+)}$ through the scattering matrix T_{21} for an interface (a), and T_{ϕ_2} for a free space. Transfer matrices are shown in the red box.

There are two incident waves, $E_1^{(+)}$ and $E_2^{(-)}$, toward the interface, and another two waves leaving (scattering away) the interface $E_1^{(-)}$ and $E_2^{(+)}$. The scattering matrix transfers the incident waves into the scattering waves.

For a typical multiple layer system such as the one shown in Figure 3.4, there are many interfaces— it would be convenient to have a transfer matrix that can associate the electric field at one side of the system to the other side. We will first introduce the transfer matrix for both interface and free space, and then show how they are used to solve the problem efficiently in the next section.

At the interface we just discussed in Figure 3.3 (a), a transfer matrix can be defined as follows:

$$\begin{pmatrix} E_2^{(+)} \\ E_2^{(-)} \end{pmatrix} = \mathbf{T}_{21} \begin{pmatrix} E_1^{(+)} \\ E_1^{(-)} \end{pmatrix}. \tag{3.29}$$

Here we have labeled the subscript ji of the transfer matrix as from material j to material i, so $\mathbf{T}_{21}$ is the scattering matrix from 1 to 2.

The scattering matrix can be represented directly using the reflection and transmission at the interface from Fresnel's formulas, and the transfer matrix can be solved

correspondingly:

$$\mathbf{S}_{21} = \begin{pmatrix} t_{21} & r_{12} \\ r_{21} & t_{12} \end{pmatrix}, \mathbf{T}_{21} = \frac{1}{t_{12}} \begin{pmatrix} t_{21}t_{12} - r_{21}r_{12} & r_{12} \\ -r_{21} & 1 \end{pmatrix}, \tag{3.30}$$

where the Fresnel's formulas are labeled in the same way as the transfer matrix.

To solve a multiple layered system, we need two types of transfer matrices—one for the interface as we just discussed, and another for the phase change of the wave propagating through a uniform medium as shown in Figure 3.3 (b). The scattering and transfer matrices for the second case can be obtained,

$$\mathbf{S}_{\phi} = \begin{pmatrix} e^{i\phi} & 0 \\ 0 & e^{i\phi} \end{pmatrix}, \mathbf{T}_{\phi} = \begin{pmatrix} e^{i\phi} & 0 \\ 0 & e^{-i\phi} \end{pmatrix}, \tag{3.31}$$

where $\phi = n_i d_i \cos\theta_i$ [39], d is the thickness, n_i and θ_i are the refractive index and the propagating direction in medium i.

3.3.3 Transfer Matrix Method

From the definition of the transfer matrix, each transfer matrix can transfer the electric field from one side to the other. Therefore, the net transfer matrix for the whole multiple layer system, as shown in Figure 3.3 (c), can be obtained by multiplying the transfer matrices for each interface with its spacing. After this transfer matrix is obtained, comparing with Eq. 3.30, both the reflection and transmission are explicit in the scattering matrix. We will first show the transfer matrix for a single layer plate, and then extend it to a N layer system.

For a one layer system, $N = 1$, as shown in Figure 3.4 (a), we will have the

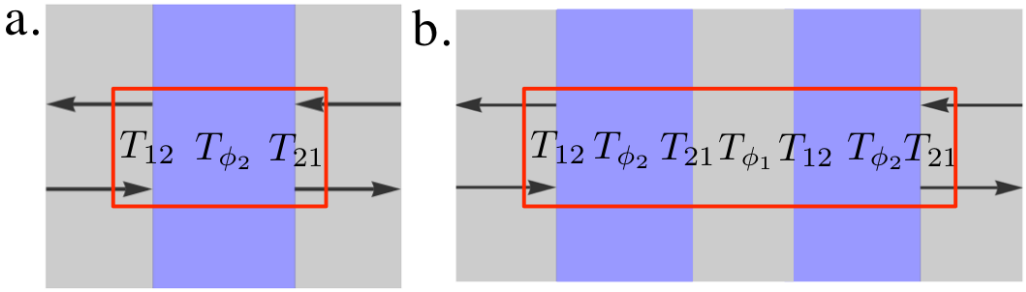

Figure 3.4: The transfer matrix for a one layer system (a), and a two layer system (b). Transfer matrices are shown in the red box.

transfer matrix:

$$\mathbf{T} = \mathbf{T}_{12}\mathbf{T}_{\phi_2}\mathbf{T}_{21}. \tag{3.32}$$

This matrix involves the multiplication of three matrices: two for the interfaces, and one for the phase changes due to the propagation between the two interfaces. A multiple layer will contains many interfaces and two types of mediums between interfaces. Following the 2 layer example shown in Figure 3.4 (b), the generalized result for a N layer system can be obtained as:

$$\mathbf{T} = \mathbf{T}_{12}\mathbf{T}_{\phi_2}\mathbf{T}_{21}\mathbf{T}_{\phi_1}...\mathbf{T}_{\phi_1}\mathbf{T}_{12}\mathbf{T}_{\phi_2}\mathbf{T}_{21} \tag{3.33}$$

$$= \mathbf{T}_{\phi_1}^{-1/2}\mathbf{T}_{core}^{N}\mathbf{T}_{\phi_1}^{-1/2}, \tag{3.34}$$

where

$$\mathbf{T}_{core} = \left[\mathbf{T}_{\phi_1}^{1/2}\mathbf{T}_{12}\mathbf{T}_{\phi_2}\mathbf{T}_{21}\mathbf{T}_{\phi_1}^{1/2}\right]. \tag{3.35}$$

If N is not large, the transfer matrix can be obtained by directly multiplication of each matrix. If N is large, we can provide another efficient way to calculate it.

This method will be used again to obtain the exact solution for the one dimensional radiative transfer theory, where $N \to \infty$, in the next section. Suppose $\mathbf{T}_{core}$ can be diagonalized by a unitary matrix $\mathbf{U}$, so that

$$\mathbf{U}\ \mathbf{T}_{core}\mathbf{U}^{-1} = \begin{pmatrix} \lambda_1 & 0 \\ 0 & \lambda_2 \end{pmatrix}, \tag{3.36}$$

where $\mathbf{U}$ can be constructed by the eigenvector of $\mathbf{T}_{core}$ and λ_i are the corresponding eigenvalues. Therefore the solution of the transfer matrix would simply be:

$$\mathbf{T} = \mathbf{T}_{\phi_1}^{-1/2}\mathbf{U}^{-1} \begin{pmatrix} \lambda_1^N & 0 \\ 0 & \lambda_2^N \end{pmatrix}\ \mathbf{U}\ \mathbf{T}_{\phi_1}^{-1/2}. \tag{3.37}$$

We denote r_{tot} and t_{tot} as the total reflection and transmission of the electric field for the whole multiple layer system. Comparing with the expression of Eq 3.30, we can get the scattering matrix and transfer matrix for the whole system in a similar form and therefore we can solve r_{tot} and t_{tot} as follows:

$$r_{tot} = -\mathbf{T}(2,1)/\mathbf{T}(2,2), \tag{3.38}$$

$$t_{tot} = \mathbf{T}(1,1) - \mathbf{T}(1,2)\mathbf{T}(2,1)/\mathbf{T}(2,2), \tag{3.39}$$

where $\mathbf{T}(i,j)$ denote the ij-th component of the matrix $\mathbf{T}$. Since both r_{tot} and t_{tot} are for electric fields, the reflection and the transmission of the energy flux can be obtained by $R = |r_t|^2$ and $T = |t_t|^2$, respectively. If there is no absorption in the system, energy would be conserved: $R + T = 1$. Note there is no need to consider the oblique factor $\cos\theta_i$, since for incident, reflected and transmitted waves, they all have the same factors, and they are canceled out in the expression for either R and

T, or r_{tot} and t_{tot}.

4. MULTIPLE SCATTERING METHODS

In Section 3, we have introduced several single scattering methods to study both iridosomes and leucosomes. Using these methods, various scattering properties can be calculated. However, in the skin of cephalopods, there are numerous iridophore and leucophore cells, and each of them can contain hundreds to thousands of iridosomes or leucosomes. After a beam of light enters the skin, the photons can be scattered many times until being reflected or transmitted out. These collective scatterings will determine the optical appearance of the skin. Although for different species, the size and number density of the iridosomes and leucosomes can vary significantly, the multiple scattering problem is essential to accurately predict the color.

In this section we will introduce several methods to solve this multiple scattering problems for a collection of leucosomes and iridosomes. We will discuss the application of these methods in modeling realistic systems in the next section. Both the leucophore and iridophore cells are modeled as a plane parallel system consisting of small random positioned scatterers, as shown in Figure 4.1 (a) and (b) for leucosomes and iridosomes, respectively. The modeled system is statistically uniform, namely, the scatterers have an equal probability of being located at any position. The system thickness (Z) and the scatterer number density (n_d) can be retrieved from the electron micrographs of a skin section, which will also be discussed in the next section. Note both the thickness and the number density must be measured consistently for the same region of the skin.

A leucosome system is a collection of spheres, as shown in Figure 4.1 (a), so their orientations doesn't matter. But iridosomes, as shown in Figure 4.2, can have

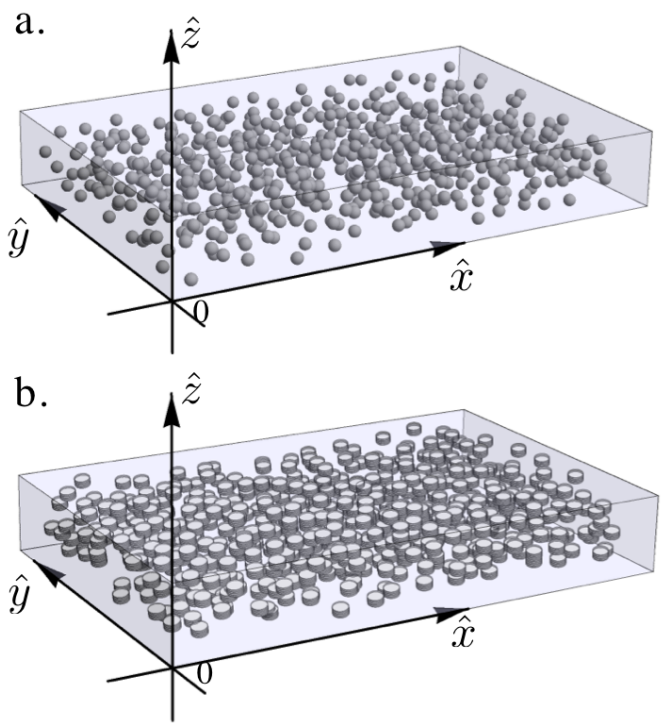

Figure 4.1: (a)A leucosome system, and (b) an iridosome system. The xyz frame is defined as the system frame for a plane parallel system with thickness Z along $\hat{z}$ direction. There is infinite spatial extent in $\pm\hat{x}$ and $\pm\hat{y}$ direction. The particles in this system can orient in any direction.

both random and fixed orientations. Therefore, a theory that can solve the multiple scattering problem for arbitrary oriented particles is required in our study. Vector radiative transfer theory is well developed for studying this kind of problem. It takes the single scattering properties as the inputs; and can calculate the angular distribution of the diffuse polarized reflectance.

In this section, we will first introduce the vector radiative transfer equation (VRTE) for oriented particles [25, 20], and discuss how it can be reduced to a simpler form for random oriented or spherical particles [21]. Their different treatments in the numerical simulations will also be discussed. After that, we will provide several exact solutions, which include the successive order of scattering solution [18, 40, 19], and the Monte Carlo solution [41, 42, 43]. (By exact, we mean there is no mathematical approximation in the formalism.) We will also introduce several approximate solutions, such as the single scattering approximation for an optically thin system [19], and a one dimensional model to estimate the reflectance [44]. These methods will be used to test the numerical methods, and estimate the final results before a full scale simulation is conducted. Both the Monte Carlo method and the one dimensional model will be widely used in our studies, and will be discussed in more details here.

4.1 Vector Radiative Transfer Equation(VRTE) for Oriented Particles

The VRTE can be used to solve the multiple scattering problem for oriented non-spherical particles [25, 20]. For oriented particles, they can either orient to a fixed direction, or have a non-random orientation, as shown in Figures 4.2 (b) and (c). The scattering process of oriented particles compared with randomly oriented particles is much more complex. For oriented particles, (1)the scattering phase function will depend on both the scattering zenith angle and azimuthal angle; (2) the extinction cross section will be different for different incident polarized states—the extinction

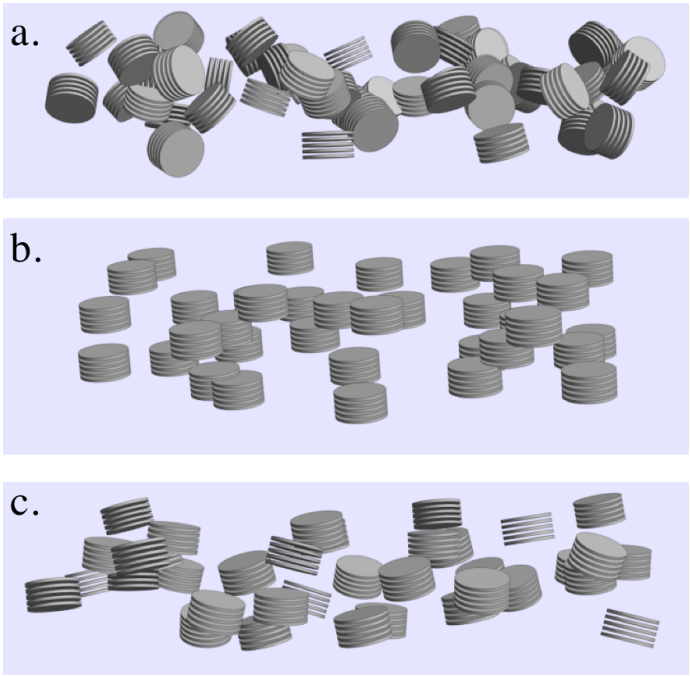

Figure 4.2: Illustrations of an iridosome system with (a) complete random orientations, (b) fixed orientations, and (c) partial random/fixed orientations.

matrix then has to be introduced. However, for spherical or random oriented particles, the phase function depends only on the zenith angle and a scalar extinction cross section is sufficient. We will show that the theory for oriented particles can be reduced to the one for random oriented particles.

In this section, I will first introduce the necessary reference frames for the study of oriented particles, and then introduce the formalism of VRTE. The solutions will be provided in the next two sections.

4.1.1 Reference Frames

Before we introduce the radiative transfer theory, we will first define the reference frames used to define the Stokes vector in a multiple scattering system, and the Mueller matrix for a single scatterer. For both randomly and fixed oriented particles, we can define the same global reference frame as shown in Figure 4.1, and Figure

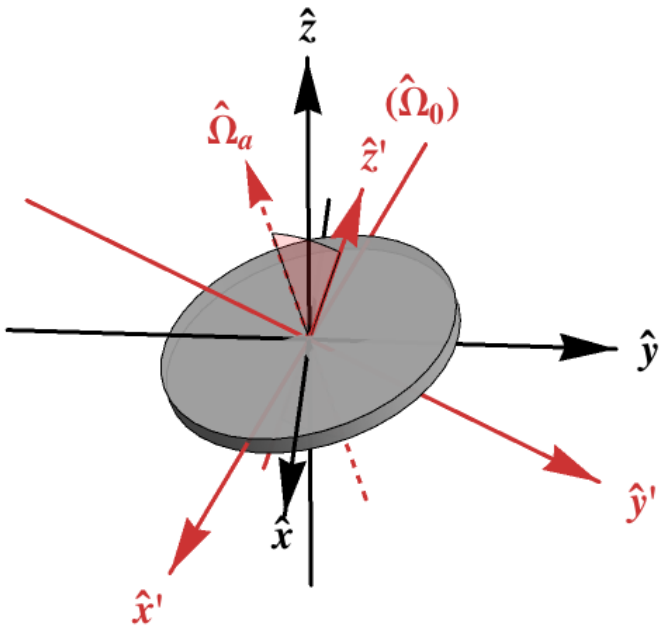

Figure 4.3: Definition of the particle $x'y'z'$ frame relative to the system xyz frame. $\hat{z}'$ is along the light incident direction $\hat{\Omega}_0$, $\hat{x}'$ is perpendicular to both $\hat{z}'$ and the particle symmetry axis $\hat{\Omega}_a$, and $\hat{y}'$ is perpendicular to both $\hat{x}'$ and $\hat{z}'$.

4.3. We denote this frame as the system frame or xyz frame. The Stokes vector in the radiative transfer equation is defined relative to the meridian plane of this frame.

For oriented particles, another reference frame which is fixed to a particle is required to specify the single scattering Mueller matrix. This system is denoted as the particle frame or $x'y'z'$ frame. For particles with an axis of symmetry, e.g. iridosomes, the relative angle β between the incident direction $\hat{\Omega}_0$ and the direction of the particle symmetry axis $\hat{\Omega}_a$ can be obtained through [18]:

$$\mu = \cos\beta = \hat{\Omega}_0 \cdot \hat{\Omega}_a. \tag{4.1}$$

Because of the particle's symmetry, only the results for $\beta \in [0, \pi/2]$ are necessary.

The direction of the cylinder axis and light propagation in the system frame are

defined in the following notations:

$$\hat{\Omega}_0 = (\mu_0, \phi_0) = \begin{pmatrix} \sqrt{1-\mu_0^2}\cos\phi_0 \\ \sqrt{1-\mu_0^2}\sin\phi_0 \\ \mu_0 \end{pmatrix}, \tag{4.2}$$

$$\hat{\Omega}_a = (\mu_a, \phi_a) = \begin{pmatrix} \sqrt{1-\mu_a^2}\cos\phi_a \\ \sqrt{1-\mu_a^2}\sin\phi_a \\ \mu_a \end{pmatrix}, \tag{4.3}$$

where $\hat{\Omega} = (\mu, \phi)$ is the direction vector with azimuthal angle ϕ and direction cosine $\mu = \cos\theta$,

To construct the particle reference frame, $\hat{z}'$ is along the light propagating direction $\hat{\Omega}_0$, $\hat{x}'$ is perpendicular to the plane determined by $\hat{\Omega}_0$ and $\hat{\Omega}_a$, and $\hat{y}'$ is perpendicular to both $\hat{x}'$ and $\hat{z}'$ (Figure 4.3):

$$\hat{z}' = \hat{\Omega}_0, \tag{4.4}$$

$$\hat{x}' = \frac{\hat{\Omega}_0 \times \hat{\Omega}_a}{|\hat{\Omega}_0 \times \hat{\Omega}_a|}, \tag{4.5}$$

$$\hat{y}' = \frac{\hat{z}' \times \hat{x}'}{|\hat{z}' \times \hat{x}'|}. \tag{4.6}$$

There are some special cases for the definition: if $\hat{\Omega}_0$ is parallel to $\hat{\Omega}_a$ but not parallel $\hat{z}$, we choose $\hat{x}' = \hat{z} \times \hat{\Omega}_a / |\hat{z} \times \hat{\Omega}_a|$; if all three vectors: $\hat{\Omega}_0$, $\hat{\Omega}_a$, and $\hat{z}$, are parallel to each other, we just simply choose $\hat{x}' = \hat{x}$. Through this definition, the scattering properties are always symmetric with respect to the $\hat{y}' - \hat{z}'$ plane, which reduces the single scattering calculation to only the region with azimuthal angle $\phi' \in [0, \pi]$, while θ' still in the range $[0, \pi]$. Note, even for particles with no symmetry, the particle frame can still be established in the same way; however, the single scattering Mueller

matrix needs to be calculated in the full range of θ', ϕ' and β'.

4.1.2 VRTE Formalism

The vector radiative transfer equation (VRTE) for randomly positioned and arbitrarily oriented particles in a homogeneous plane parallel system is given [25] by

$$-\mu\frac{d\mathbf{I}(z,\hat{\Omega})}{dz} = \boldsymbol{\beta}(\hat{\Omega})\mathbf{I}(z,\hat{\Omega}) - \int_{4\pi} d\Omega'\beta_s(\hat{\Omega}')\mathbf{P}(\hat{\Omega},\hat{\Omega}')\mathbf{I}(z,\hat{\Omega}'), \tag{4.7}$$

where n_d is the number density, and the extinction coefficient matrix $\boldsymbol{\beta}(\hat{\Omega}) = n_d(\hat{\Omega})\mathbf{K}(\hat{\Omega})$, the scattering coefficient $\beta_s(\hat{\Omega}') = n_d C_s(\hat{\Omega}')$, here $\mathbf{K}$ is the extinction matrix and C_s is the scattering cross section for unpolarized light. The upper boundary of the plane parallel system is Z while the lower boundary is 0 (Figure 4.1). The boundary condition is specified by $I(0,\mu > 0,\phi)$ and $I(Z,\mu < 0,\phi)$. No surface reflections are considered in this work. Generally, the scattering coefficient β, phase matrix P and extinction matrix K all depend on the incident light direction and the particle's orientation.

For randomly oriented or spherical particles, the extinction matrix reduces to the scalar extinction cross section. The solution of the VRTE will be much simplified which we will shown in section 4.3, and also provide its integral solution along with several approximate results. In this section, we will formulate the general VRTE for arbitrarily oriented particles.

Stokes vector $\mathbf{I} = (I, Q, U, V)^T$ is defined in the meridian plane of the system frame, while the Mueller matrix, $\mathbf{M}$, is defined relative to the scattering plane in the particle frame. The phase matrix is defined [21] as:

$$\mathbf{P}(\hat{\Omega},\hat{\Omega}') = \mathbf{L}(\pi - i_2)\mathbf{M}(\mu_s,\phi_s)\mathbf{L}(-i_1), \tag{4.8}$$

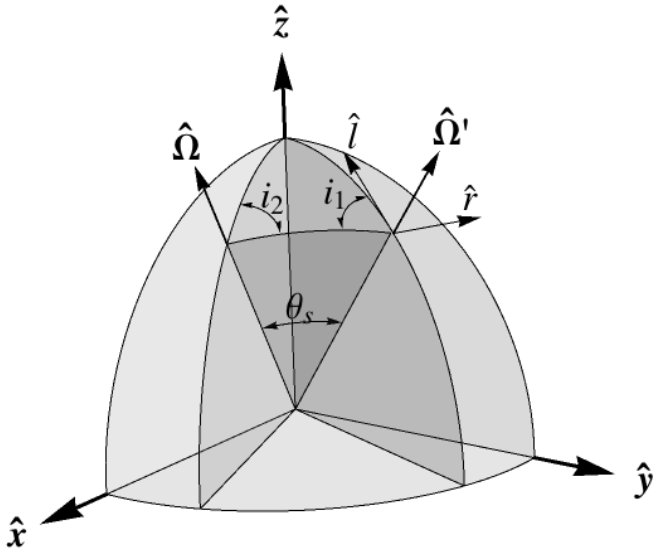

Figure 4.4: Rotations of the Stokes vectors. The incident and scattered Stokes vectors are defined relative to the meridian planes $\hat{z} - \hat{\Omega}'$ and $\hat{z} - \hat{\Omega}$, respectively. i_1 and i_2 indicate the relative angles between the meridian planes and the scattering plane $\hat{\Omega} - \hat{\Omega}'$. θ_s is the scattering angle. Unit vectors $\hat{l}$ and $\hat{r}$ denote the parallel and perpendicular components of the electric field, and they are used to define the rotation matrix $\mathbf{L}(\theta)$.

where $\mu_s = \cos\theta_s$, θ_s is the scattering angle, and ϕ_s is determined in the particle frame. $\mathbf{L}(-i_1)$ is the rotation matrix which takes the incident meridian plane to the scattering plane, and $\mathbf{L}(\pi - i_2)$ is the clockwise rotation which takes the scattering plane to the new meridian plane as shown in Figure 4.4. Recall that the Mueller matrix $\mathbf{M}(\mu_s, \phi_s)$ is defined in the particle frame with incident light along z' and the scattered light in the direction (μ_s, ϕ_s). To define the rotation matrix $\mathbf{L}$, the unit vectors for the parallel $(\hat{l})$ and perpendicular $(\hat{r})$ components of the electric field are defined in Figure 4.4, and $\hat{r} \times \hat{l}$ is along the light propagating direction $\hat{\Omega}'$.

The phase function used here $P = \mathbf{P}_{11} = M = \mathbf{M}_{11}$ is normalized according to:

$$\int_{4\pi} d\Omega' P(\hat{\Omega}, \hat{\Omega}') = 1. \tag{4.9}$$

The extinction coefficient matrix $\boldsymbol{\beta}$ for a particle with a mirror symmetry [25] can be expressed as:

$$\boldsymbol{\beta} = n_d \mathbf{K} = \begin{pmatrix} \beta_{ext} & \beta_{pol} & 0 & 0 \\ \beta_{pol} & \beta_{ext} & 0 & 0 \\ 0 & 0 & \beta_{ext} & \beta_{cpol} \\ 0 & 0 & \beta_{cpol} & \beta_{ext} \end{pmatrix} \tag{4.10}$$

The extinction coefficient, polarized and circular polarized coefficients are defined as $\beta_{ext} = n_d C_{ext}$, $\beta_{pol} = n_d C_{pol}$ and $\beta_{cpol} = n_d C_{cpol}$, where C_{ext},C_{pol} and C_{cpol} are the extinction cross section, the linear polarized and circular polarized cross sections. The properties of this matrix for an iridosome will be discussed in Section 5. The extinction matrix $\mathbf{K}_0$ is calculated through the forward scattering amplitude matrix with azimuthal angle $\phi' = 0$ in the $x'y'z'$ frame. Generally, the meridian plane of the Stokes vector defined in the system frame corresponds to an azimuthal angle $\phi' \neq 0$

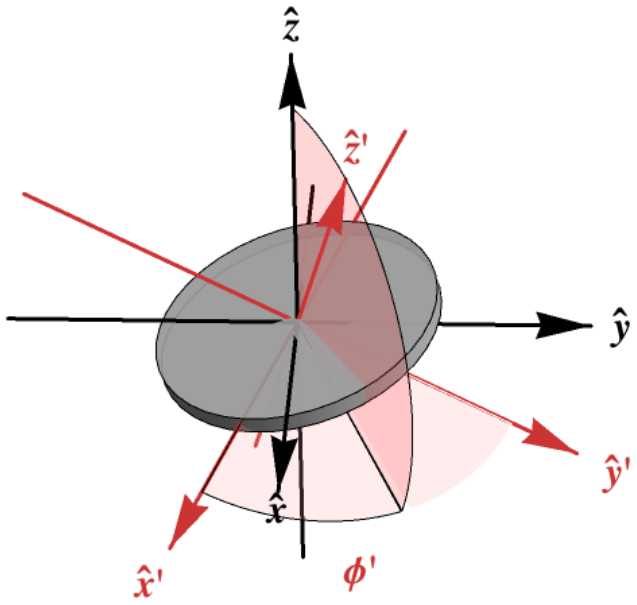

Figure 4.5: Illustration for the rotation of extinction matrix. Light is propagating along $\hat{z}'$, and its Stokes vector is defined relative to the meridian plane $\hat{z} - \hat{z}'$ in the system frame. This corresponds to an azimuthal angle ϕ' in the particle $x'y'z'$ frame. Since the extinction matrix is always calculated relative to the $\hat{x}' - \hat{z}'$ plane in the particle frame. A rotation of the extinction matrix to the $\hat{z} - \hat{z}'$ plane is required in order to use it in the vector radiative transfer equation.

in the particle frame (Figure 4.5), we need to perform proper rotations before we can use this matrix in the radiative transfer simulations:

$$\mathbf{K}(\hat{\Omega}) = \mathbf{L}(\phi')\mathbf{K}_0\mathbf{L}(-\phi'). \tag{4.11}$$

Therefore, we don't have to evaluate the extinction matrix for each different meridian plane in the particle frame.

4.2 Exact Solutions

Several approaches has been developed to study the radiative transfer of oriented non-spherical particle [45, 46, 47, 48, 49, 50, 51]. In this section, we will first formulate the successive orders of scattering (SOS) solutions for VRTE [18, 40, 19], and then we will evaluate the SOS solutions using the Monte Carlo method.

4.2.1 Successive Order of Scattering (SOS) Solution

The formal integral solution for the VRTE (Eq. 4.7) can be found as:

$$\begin{aligned}\mathbf{I}(z,\hat{\Omega}) &= \mathbf{T}(\hat{\Omega}, z, z_m(-\mu))\mathbf{I}(z_m(-\mu),\hat{\Omega}) \\ &+ \int_{z_m(-\mu)}^{z} \frac{dz_1}{\mu}\mathbf{T}(\Omega, z, z_1)\int_{4\pi} d\Omega'\beta_s(\hat{\Omega}')\mathbf{P}(\hat{\Omega},\hat{\Omega}')\mathbf{I}(z_1,\hat{\Omega}'),\end{aligned} \tag{4.12}$$

where the transmission matrix is defined as:

$$\mathbf{T}(\hat{\Omega}, z'', z') = \exp[-\boldsymbol{\beta}(\hat{\Omega})(z''-z')/\mu] \tag{4.13}$$

Since the system is homogeneous, the extinction matrix doesn't depend on positions. $(z''-z')/\mu$ is the distance the light propagates along $\hat{\Omega}$, where $\hat{\Omega} = (\mu, \phi)$.

To simplify the expression of Eq. 4.12, we introduced a boundary selection function $z_m(\mu)$. Through it, the proper boundary in the equation can be determined by

the direction cosine μ of light propagation:

$$z_m(\mu) = \begin{cases} Z & \text{if } \mu > 0; \\ 0 & \text{if } \mu < 0. \end{cases} \tag{4.14}$$

Note that $z_m(-\mu) = Z - z_m(\mu)$.

Without this boundary function, Eq. 4.12 has to be separated into two equations for different boundary conditions as follows:

$$\begin{aligned} \mathbf{I}(z, \hat{\Omega}) &= \mathbf{T}(\hat{\Omega}, z, 0)\mathbf{I}(0, \hat{\Omega}) \\ &\quad + \int_0^z \frac{dz_1}{\mu} \mathbf{T}(\hat{\Omega}, z, z_1) \int_{4\pi} d\Omega' \beta_s(\hat{\Omega}') \mathbf{P}(\hat{\Omega}, \hat{\Omega}') \mathbf{I}(z_1, \hat{\Omega}'), \qquad \mu > 0 \end{aligned} \tag{4.15}$$

$$\begin{aligned} \mathbf{I}(z, \hat{\Omega}) &= \mathbf{T}(\hat{\Omega}, z, Z)\mathbf{I}(Z, \hat{\Omega}) \\ &\quad + \int_Z^z \frac{dz_1}{\mu} \mathbf{T}(\Omega, z, z_1) \int_{4\pi} d\Omega' \beta_s(\hat{\Omega}') \mathbf{P}(\hat{\Omega}, \hat{\Omega}') \mathbf{I}(z_1, \hat{\Omega}'). \qquad \mu < 0 \end{aligned} \tag{4.16}$$

By introducing the boundary function, the solution for the upwelling and downwelling radiance can be combined together, and we can then expand Eq. 4.12 into a series of different order terms: Consider a plane wave source at the boundary in the direction $\hat{\Omega}_0$:

$$\mathbf{I}(z_m(-\mu), \hat{\Omega}) = \mathbf{I}_0 \delta(\hat{\Omega} - \hat{\Omega}_0), \tag{4.17}$$

and due to the linearity of the VRTE, the transformation matrix between the incident Stokes vector and the scattered Stokes vector can be denoted by the effective Mueller matrix:

$$\mathbf{I}(z, \hat{\Omega}) = \mathbf{M}^{eff}(z, \hat{\Omega})\mathbf{I}_0, \tag{4.18}$$

and $\mathbf{M}^{eff}$ is the summation of all order of scattering terms:

$$\mathbf{M}^{eff} = \sum_{n=0}^{\infty} \mathbf{M}_n^{eff}, \tag{4.19}$$

M_0^{eff} is the direct term which only describes the attenuation of the direct light along its incident direction:

$$\mathbf{M}_0^{eff}(z, \hat{\Omega}) = \mathbf{T}(\hat{\Omega}_0, z, z_m(-\mu_0))\delta(\hat{\Omega} - \hat{\Omega}_0), \tag{4.20}$$

The diffuse effective Mueller matrix includes the summation of $n \geq 1$ terms, as shown in the next section, which can be calculated numerically for a general phase matrix. The general n-th order term of the SOS method can be expressed iteratively as:

$$\mathbf{M}_n^{eff}(z, \hat{\Omega}) = \int_{z_m(-\mu)}^{z} \frac{dz_n}{\mu} \mathbf{T}(\hat{\Omega}, z, z_n) \int_{4\pi} d\Omega_n \beta_s(\hat{\Omega}_n) \mathbf{P}(\hat{\Omega}, \hat{\Omega}_n) \mathbf{M}_{n-1}^{eff}(z_n, \hat{\Omega}_n) \tag{4.21}$$

For example, the explicit expression for the first and the second order terms would be:

$$\mathbf{M}_1^{eff}(z, \hat{\Omega}) = \int_{z_m(-\mu)}^{z} \frac{dz_1}{\mu} \mathbf{T}(\hat{\Omega}, z, z_1) \beta_s(\hat{\Omega}_0) \mathbf{P}(\hat{\Omega}, \hat{\Omega}_0) \mathbf{T}(\hat{\Omega}_0, z_1, z_m(-\mu_0)) \tag{4.22}$$

$$\begin{aligned} \mathbf{M}_2^{eff}(z, \hat{\Omega}) = & \int_{z_m(-\mu)}^{z} \frac{dz_2}{\mu} \mathbf{T}(\hat{\Omega}, z, z_2) \int_{4\pi} d\Omega_2 \beta_s(\hat{\Omega}_2) \mathbf{P}(\hat{\Omega}, \hat{\Omega}_2) \\ & \times \int_{z_m(-\mu_2)}^{z_2} \frac{dz_1}{\mu_2} \mathbf{T}(\hat{\Omega}_2, z_2, z_1) \beta_s(\hat{\Omega}_0) \mathbf{P}(\hat{\Omega}_2, \hat{\Omega}_0) \mathbf{T}(\hat{\Omega}_0, z_1, z_m(-\mu_0)) \end{aligned} \tag{4.23}$$

Note that without using the boundary selection function, the first order solution will have two terms, while the second order solution will have 4 terms, and the n-th order solution will have 2^n terms.

4.2.2 Monte Carlo Method

Direct integration of the the SOS solution is very complex. It is only feasible for the simple Rayleigh scattering Mueller matrix. For a system with arbitrary particles, such as iridosomes and leucosomes, we can only solve the VRTE numerically. In this section, we will introduce a Monte Carlo method, which can statistically evaluate the integrations over solid angles and distances in the SOS solution —the integrations will be replaced by the summation over sampled distances and directions. For randomly oriented particles —both $\beta_{pol} = 0$ and $\beta_{cpol} = 0$, our method then reduces to the standard Monte Carlo method discussed in previous works [41, 42, 43].

As shown in Eq. 4.21, there are two types of integrations, associated with both the distance and direction. In order to evaluate each terms in the SOS solution, we need to statistically sample both distance and direction efficiently. The direction and distance will be sampled in the sequence from the light source to the detector (called a forward approach). Furthermore, We will associate each sequence of the sampled directions and distances with a photon package with an initial weight of unity [42]. A part of the weight will be reduced after each sampling, until the final results are sufficiently converged. In our following examples, incident light is propagating downwardly with $\mu_0 < 0$ from the upper boundary $z_m(-\mu_0) = Z$ (source location), and the transmitted radiance is evaluated at the lower boundary with $\mu < 0$ and $z_m(\mu) = 0$ (detector location). This can also be seen from the boundary function Eq. 4.14: $z_m(\mu_0) = 0$ and $z_m(-\mu) = Z$.

To sample the physical length z_i for the oriented particle systems, we need to further study the properties of the transmission matrix (Eq. 4.13). The transmission

matrix can be simplified as:

$$\mathbf{T}(\hat{\Omega}, z'', z') = \exp(-\tau) \cdot \begin{pmatrix} \cosh(p\tau) & -\sinh(p\tau) & 0 & 0 \\ -\sinh(p\tau) & \cosh(p\tau) & 0 & 0 \\ 0 & 0 & \cos(p'\tau) & -\sin(p'\tau) \\ 0 & 0 & \sin(p'\tau) & \cos(p'\tau) \end{pmatrix}, \tag{4.24}$$

where $\tau = \beta_{ext}(z'' - z')/\mu$, is the optical depth for unpolarized light, and $p = \beta_{pol}/\beta_{ext} = C_{pol}/C_{ext}$, $p' = \beta_{cpol}/\beta_{ext} = C_{cpol}/C_{ext}$. τ, p and p' all depend on the incident direction $\hat{\Omega}$ and the particles' orientation. The radiance is attenuated according to the transmission function:

$$\begin{aligned} T(\hat{\Omega}, z'', z') &= \mathbf{T}(\hat{\Omega}, z'', z')_{11} = \exp(-\tau)\cosh(p\tau), \\ &= \frac{1}{2}(\exp[-(1+p)\tau] + \exp[-(1-p)\tau]). \end{aligned} \tag{4.25}$$

This function will be used to sample the distance z''.

For randomly oriented particles, light will not polarize through attenuation. However, for oriented particles, as shown in Eq. 4.24, light can be polarized due to the contribution of a non-zero β_{pol}. The degree of polarization for an unpolarized incident light source is $\tanh(p\tau)$, which will approach unity when $p\tau$ is very large, and the longer the propagating path, the more it will be polarized.

The error in the radiance of the direct term, M_0^{eff}, brought about by neglecting the contribution of non-zero β_{pol} or p is defined by $T_p/T_{p=0} - 1 = \cosh(p\tau) - 1$, as shown in Figure 4.6. For example, for $\tau = 5$, $p = 0.05$ can lead to a 3% error in the total radiance transmission; for $p = 0.1$, a 13% error; and for $p = 0.15$, a 30% error. Thus, for an optically thick layer, even very small p can still lead to large

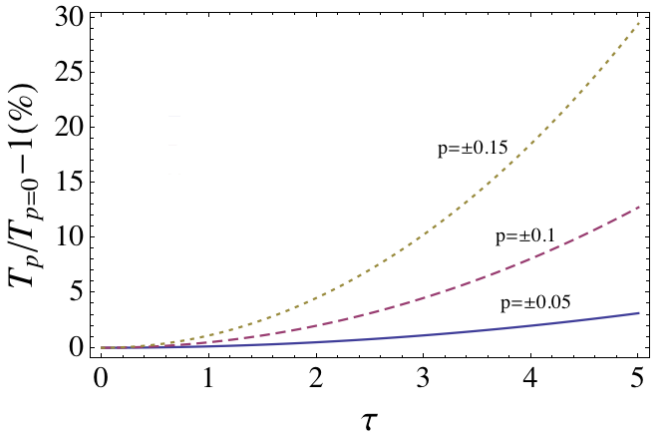

Figure 4.6: The error on the attenuated direct radiance for neglecting of β_{pol} with unpolarized light source. $T_{p=0} = \exp(-\tau)$ and $T_p = \exp(-\tau)\cosh(p\tau)$. Results for $p = \pm 0.05, \pm 0.1$, and ± 0.15 are shown.

error on the radiance of direct light. Generally to have an error less than 10% for the attenuation of the direct light, we should have $|p|\tau \leq 0.44$. Since for a plane parallel system $\tau = \beta_{ext}\Delta z/\mu$, even for small change of Δz at the zenith angle close to $\pi/2$, there are still large errors. To obtain the total radiance, all the diffuse terms have to be evaluated numerically, and there is generally no analytical results even for the first order term.

As examples for this Monte Carlo approach, the first two orders of the solution (Eqs. 4.22 and 4.23) will be discussed. The examples can be extended to a general n-th order term. The first order term has only one integration with z_1:

$$\mathbf{M}_1^{eff}(0,\hat{\Omega}) = \int_Z^0 \frac{dz_1}{\mu}\mathbf{T}(\hat{\Omega},0,z_1)\beta_s(\hat{\Omega}_0)\mathbf{P}(\hat{\Omega},\hat{\Omega}_0)\mathbf{T}(\hat{\Omega}_0,z_1,Z)), \tag{4.26}$$

$$= \frac{\mu_0}{\mu}\int_Z^0 \frac{dz_1}{\mu_0}\mathbf{T}(\hat{\Omega},0,z_1)\underline{\beta_s(\hat{\Omega}_0)}\mathbf{P}(\hat{\Omega},\hat{\Omega}_0)\underline{\mathbf{T}(\hat{\Omega}_0,z_1,Z))}. \tag{4.27}$$

while there are two transmission matrices associated with z_1, the left matrix $\mathbf{T}(\hat{\Omega},0,z_1)$ is a function of z_1/μ, and the rightmost matrix $\mathbf{T}(\hat{\Omega}_0,z_1,Z)$ is a function of z_1/μ_0.

$\mathbf{T}(\hat{\Omega}_0, z_1, Z)$ is chosen to sample z_1/μ_0; this is equivalent to propagating a photon forwardly from the source to the detector.

There are two approaches to sample the z_i, one is to use $\exp(-\tau)$ as in a randomly oriented system. But since there is a $\cosh[p\tau]$ term left in the transmission function, which will be divergent very fast for a small value of μ. In order to have a stable algorithm, it's better to use the full transmission function $\exp(-\tau)\cosh(p\tau)$ (Eq. 4.25) as the probability density function. Meanwhile, this function is also the best probability density function for the importance sampling which has better efficiency compared with $\exp(-\tau)$. In Eq. 4.27, since the integration integral for z_1 is finite, the transmission function T needs to be normalized before using it as a probability density function. A weight function W is defined as (the corresponding parts of integral are underlined in Eq. 4.27) :

$$\begin{aligned} W(\hat{\Omega}', z_b, z_a) &= \beta_s(\hat{\Omega}') \int_{z_a}^{z_b} \frac{dz}{\mu} T(\hat{\Omega}', z, z_a) \\ &= \frac{\beta_s}{\beta_{ext}} \frac{(1 - T_m(\hat{\Omega}', z_b, z_a))}{(1 - p^2)}, \end{aligned} \tag{4.28}$$

$$\begin{aligned} T_m(\hat{\Omega}', z_b, z_a) &= \frac{1+p}{2} \exp[-(1-p)\beta_{ext}(z_b - z_a)/\mu] \\ &+ \frac{1-p}{2} \exp[-(1+p)\beta_{ext}(z_b - z_a)/\mu], \end{aligned} \tag{4.29}$$

where $p = p(\hat{\Omega}')$, $\beta_s = \beta_s(\hat{\Omega}')$, and $\beta_{ext} = \beta_{ext}(\hat{\Omega}')$. $\alpha = \beta_s/\beta_{ext}$ is the scattering albedo for unpolarized light. When $p = 0$, $W = \alpha(1 - exp[-\beta_{ext}(z_b - z_a)/\mu)])$, which is the ratio of the photon package scattered during the attenuation from z_a to z_b in the direction $\hat{\Omega}'$ according to the Bouguer-Lambert-Beer law. The probability density function t, and the cumulative probability function t_c can be defined by using

W and T_m as follows:

$$t(\hat{\Omega}', z, z_a) = \frac{\beta_s(\hat{\Omega}')}{\mu'} \frac{T(\hat{\Omega}', z, z_a)}{W(\hat{\Omega}', z_b, z_a)}, \tag{4.30}$$

$$t_c(\hat{\Omega}', z, z_a) = \int_{z_a}^{z} dz' t(\hat{\Omega}', z, z_a) = \frac{1 - T_m(\hat{\Omega}', z', z_a)}{1 - T_m(\hat{\Omega}', z_b, z_a)} \tag{4.31}$$

To sample a distance z_i, a random number η is generated, and z_i can be inverted through $\eta = t_c(\hat{\Omega}', z_i, z_a)$. Meanwhile, the reduced transmission matrix: $\tilde{\mathbf{T}} = \mathbf{T}/T$, is introduced to remove the bias in the sampling of the distance using only T instead the whole transmission matrix. Therefore, $\mathbf{M}_1^{eff}$ can be statistically evaluated as:

$$\mathbf{M}_1^{eff}(0, \hat{\Omega}) = \frac{\mu_0}{\mu} \frac{1}{N_1} \sum_{i1} \mathbf{T}(\hat{\Omega}, 0, z_{i1}) \mathbf{P}(\hat{\Omega}, \hat{\Omega}_0) W(\hat{\Omega}_0, 0, Z) \tilde{\mathbf{T}}(\hat{\Omega}_0, z_{i1}, Z), \tag{4.32}$$

where N_1 is the total number of sampled Z_{i1}. In this example, only the position is sampled. For higher order terms, we have to evaluate both the positions and directions.

For the second order term, the effective Mueller matrix at the top of the system can be obtained from Eq. 4.23 as:

$$\begin{aligned} \mathbf{M}_2^{eff}(0, \hat{\Omega}) = & \int_Z^0 \frac{dz_2}{\mu} \mathbf{T}(\hat{\Omega}, 0, z_2) \int_{4\pi} d\Omega_2 \beta_s(\hat{\Omega}_2) \mathbf{P}(\hat{\Omega}, \hat{\Omega}_2) \\ & \times \int_{z_m(-\mu_2)}^{z_2} \frac{dz_1}{\mu_2} \mathbf{T}(\hat{\Omega}_2, z_2, z_1) \beta_s(\hat{\Omega}_0) \mathbf{P}(\hat{\Omega}_2, \hat{\Omega}_0) \mathbf{T}(\hat{\Omega}_0, z_1, Z). \end{aligned} \tag{4.33}$$

There are two functions associated with each z_i and Ω_i. To use the Monte Carlo method in the current formalism, z_2 has to be sampled first by using $\mathbf{T}(\hat{\Omega}, 0, z_2)$, since sampling z_1 will always require the value of z_2, no matter which probability function is chosen. This would be equivalent to propagating a photon from the detector to the source. On the contrary, in order to perform a forward Monte Carlo method, we first

reverse the integration order of z_2 and z_1, and then change the corresponding intervals to make the integral results the same (Protter and Morrey 1985,p307): $z_2 \in [Z, 0]$ and $z_1 \in [z_m(-\mu_2), z_2]$ is changed to $z_1 \in [Z, 0]$ and $z_2 \in [z_1, Z - z_m(-\mu_2)] = [z_1, z_m(\mu_2)]$. Finally, the order of μ, μ_0 and μ_2 are rearranged:

$$\mathbf{M}_2^{eff}(0,\hat{\Omega}) = \frac{\mu_0}{\mu}\int_Z^0 \frac{dz_1}{\mu_0}\mathbf{T}(\hat{\Omega},0,z_2)\int_{4\pi} d\Omega_2\beta_s(\hat{\Omega}_2)\mathbf{P}(\hat{\Omega},\hat{\Omega}_2) \times \int_{z_1}^{z_m(\mu_2)} \frac{dz_2}{\mu_2}\mathbf{T}(\hat{\Omega}_2,z_2,z_1)\beta_s(\hat{\Omega}_0)\mathbf{P}(\hat{\Omega}_2,\hat{\Omega}_0)\mathbf{T}(\hat{\Omega}_0,z_1,Z). \tag{4.34}$$

The corresponding functions and integrals for the sampling are distinguished with the same number of underlines. In this example, the sampling sequence is z_1, Ω_2 and z_2. Note, to sample $\hat{\Omega}_2$ we choose the rightmost phase function $P(\hat{\Omega}_2, \hat{\Omega}_0)$ which is dependent on $\hat{\Omega}_2$. Since the phase function is normalized over 4π solid angles (Eq. 4.9), it can be used as probability density function to sample $\hat{\Omega}_2$ directly. Similar to the reduced transmission matrix, the reduced phase matrix is defined as $\tilde{\mathbf{P}} = \mathbf{P}/P$. Note here P=M, and $\tilde{\mathbf{P}} = \mathbf{L}(\pi - i_2)\tilde{\mathbf{M}}(\mu_s, \phi_s)\mathbf{L}(-i_1)$. Both angles μ_s and ϕ_s can be sampled through the bivariate function $M(\mu_s, \phi_s)$. Therefore, the second order effective Mueller matrix $\mathbf{M}_2^{eff}$ can be evaluated statistically as:

$$\mathbf{M}_2^{eff}(0,\hat{\Omega}) = \frac{\mu_0}{\mu}\frac{1}{N_2}\sum_{i2}\sum_{j2}\sum_{i1}\mathbf{T}(\hat{\Omega},0,z_{i2})\mathbf{P}(\hat{\Omega},\hat{\Omega}_{j2})W(\hat{\Omega}_{j2},z_{i1},z_m(\mu_{j2})) \times \tilde{\mathbf{T}}(\hat{\Omega}_{j2},z_{i2},z_{i1})\tilde{\mathbf{P}}(\hat{\Omega}_{j2},\hat{\Omega}_0)W(\hat{\Omega}_0,0,Z)\tilde{\mathbf{T}}(\hat{\Omega}_0,z_{i1},Z), \tag{4.35}$$

N_2 is the total number of the sampled z_{i2}, $\hat{\Omega}_{j2}$, and z_{i1}. From Eq. 4.28, the physics of sampling the distance z in this approach is to force a collision within the boundary of the system, and the corresponding bias is removed by reducing the photon weight by $(1 - T_m)$ similar to the discussion in [41, 42]. This can save the

samples which will have no chance of scattering inside the system, and guarantees that every photon contributes to the detector. Furthermore, an extra factor $(1-p^2)^{-1}$ needs to be considered to make the probability function normalized. Meanwhile, the oblique factor μ_0/μ comes naturally from changing the integral sequence, a physical interpretation can be found in [42, 52].

To study the structure of the solution terms, and to design an efficient algorithm to evaluate the higher order terms, we can neglect all the explicit notations for the summations and the angle and position dependences. According to Eqs. 4.32 and 4.35, M_1^{eff} and M_2^{eff} terms can be expressed symbolically as:

$$\mathbf{M}_1^{eff} = \frac{\mu_0}{\mu}\mathbf{TP}W\tilde{\mathbf{T}}, \tag{4.36}$$

$$\mathbf{M}_2^{eff} = \frac{\mu_0}{\mu}\mathbf{TP}W\tilde{\mathbf{T}}\tilde{\mathbf{P}}W\tilde{\mathbf{T}}, \tag{4.37}$$

and from iteration, the nth order term, M_n^{eff}, can also be expressed as:

$$\mathbf{M}_n^{eff} = \frac{\mu_0}{\mu}\mathbf{TP}W\tilde{\mathbf{T}}(\tilde{\mathbf{P}}W\tilde{\mathbf{T}})^{n-1}. \tag{4.38}$$

The forward time sequences of the scattering and propagation of the photons corresponding to the multiplication of the terms from right to left. $W\tilde{\mathbf{T}}(\tilde{\mathbf{P}}W\tilde{\mathbf{T}})^{n-1}$ is called the collision part, and $\mathbf{TP}$ the estimation part. During the first $(n-1)$ collision processes, the photon contribution is evaluated through the reduced matrices. After the last step of the collisions, every sampled photon is directly estimated to the detector using the full phase matrix and transmission matrix $\mathbf{TP}$.

To improve the efficiency of the Monte Carlo evaluation, an efficient estimation scheme is developed based on the solution's structure of the total diffused effective

Mueller matrix:

$$\begin{aligned}\mathbf{M}^{eff} &= \sum_{1}^{N} \mathbf{M}_n^{eff}, \\ &= \mathbf{M}_1^{eff} + \mathbf{M}_2^{eff} + \mathbf{M}_3^{eff} + ... + \mathbf{M}_N^{eff}, \\ &= \frac{\mu_0}{\mu}(\mathbf{TP}W\tilde{\mathbf{T}} + \mathbf{TP}W\tilde{\mathbf{T}}(\tilde{\mathbf{P}}W\tilde{\mathbf{T}}) + ...\mathbf{TP}W\tilde{\mathbf{T}}(\tilde{\mathbf{P}}W\tilde{\mathbf{T}})^{N-1}), \\ &= \frac{\mu_0}{\mu}((((..)W\tilde{\mathbf{T}}\tilde{\mathbf{P}} + \mathbf{TP})W\tilde{\mathbf{T}}\tilde{\mathbf{P}} + \mathbf{TP})W\tilde{\mathbf{T}}\tilde{\mathbf{P}} + \mathbf{TP})W\tilde{\mathbf{T}}. \end{aligned} \tag{4.39}$$

M_n^{eff} is on the order of W^n, which is the net photon weight for the corresponding photon package. N is the highest order of scattering required in this calculation, and it can be determined when the photon weight W^n is small enough. Eq. 4.39 is the summation over all orders of z_i and $\hat{\Omega}_i$. Note the structure $W\tilde{\mathbf{T}}\tilde{\mathbf{P}} + \mathbf{TP}$, which corresponds to a virtual photon estimated to the detector through $\mathbf{TP}$, then another collision is sampled by $W\tilde{\mathbf{T}}\tilde{\mathbf{P}}$ with a new direction, position and photon weight. This process continues until the photon weight is decreased to a small enough value. Through this scheme, any photon sample having a N-th order contribution to the detector will automatically contribute to all the orders $n \in [1, N]$. Zhai and et.al. provided an estimation scheme to improve the efficiency of the Monte Carlo simulation for randomly oriented particles, and provided a detailed algorithm to implement them [42]. Following our approach based on SOS, we can show a similar estimation scheme can be developed through the exact combination of different orders of scattering terms for oriented particles.

4.3 Approximate Solutions

As discussed previously, for spherical and randomly oriented particle, the extinction matrix will reduce to a scalar quantity, and the VRTE can be simplified. In this section, we will provide several approximate solution for such a spherical and

randomly oriented particle system. We will first introduce the single scattering approximation [18, 19], which works for a system with very thin optical depth, and can also be used to test the numerical code. Based on this result we will discuss the exact solution of a one dimensional model for the irradiance reflectance estimation [44]. Since this method is highly efficient, before conducting the full scale Monte Carlo simulations, we will start with this method for leucosomes and randomly oriented iridosomes.

For randomly oriented particles, instead of using the actual physical distance z, we can define a dimensionless optical depth τ as

$$\tau = \int_z^\infty \beta(z)dz, \tag{4.40}$$

where for a plane parallel system in our consideration, the lower limit $z \in [0, Z]$. From this definition, the top surface is $\tau = 0$, and the bottom surface has the maximum optical depth, denoted by $\tau = \tau_m$. The integral solution of RTE for randomly oriented particles of a homogeneous system:

$$\mathbf{I}(\tau, \Omega) = e^{-(\tau_m(-\mu)-\tau)/\mu}\mathbf{I}(\tau_m(-\mu), \Omega) + \int_\tau^{\tau_m(-\mu)} \frac{d\tau_1}{\mu} e^{-(\tau_1-\tau)/\mu}\omega \int d\Omega_1 \mathbf{P}(\Omega, \Omega_1)\mathbf{I}(\tau_1, \Omega_1), \tag{4.41}$$

where $\Omega = \{\mu, \phi\}$. Similar to the boundary function we defined previously, when $\mu > 0$, $\tau_m(-\mu) = \tau_m$ is the lower boundary, and when $\mu < 0$, $\tau_m(-\mu) = 0$ is the upper boundary. The source term is defined as:

$$\mathbf{I}(\tau_m(-\mu), \Omega) = \mathbf{F}_0(\Omega_0)\delta(\Omega - \Omega_0). \tag{4.42}$$

Through iteration starting from this term, we can get the scattering terms at any

order.

4.3.1 Single Scattering Approximation

The single scattering approximation will only consider the first order scattering—the photon will be only scattered once [18, 19]. For a very thin layer, only first order scattering dominates, and this approximation will be accurate enough to calculate the reflectance. Based on the integral solution, Eq. 4.41, we can get the direct (zero-th order) scattering term:

$$\mathbf{I}_0(\tau,\Omega) = e^{-(\tau_m(-\mu_0)-\tau)/\mu_0}\mathbf{F}_0(\Omega_0)\delta(\Omega-\Omega_0). \tag{4.43}$$

This corresponds to the attenuation of the incident light. The next order iteration will give the first order term:

$$\mathbf{I}_1(\tau,\Omega) = \int_\tau^{\tau_m(-\mu)} \frac{d\tau_1}{\mu} e^{-(\tau_1-\tau)/\mu}\omega(\tau_1)\mathbf{P}(\Omega,\Omega_0)e^{-(\tau_m(-\mu_0)-\tau_1)/\mu_0}\mathbf{F}_0(\Omega_0) \tag{4.44}$$

Here we only consider the light incident from the top with $\mu_0 < 0$ and the reflection(upwelling radiance) with $\mu > 0$ at optical depth τ, the first order term is:

$$\mathbf{I}_1(\tau,\Omega) = \int_\tau^{\tau_m} \frac{d\tau_1}{\mu} e^{-(\tau_1-\tau)/\mu}\omega(\tau_1)\mathbf{P}(\Omega,\Omega_0)e^{\tau_1/\mu_0}\mathbf{F}_0(\Omega_0), \tag{4.45}$$

note here $\mu_0 < 0$ so $\tau_1/\mu_0 < 0$. Considering the optical depth at $\tau = 0$, we can integrate the above equation:

$$\mathbf{I}_1(0,\Omega) = \frac{|\mu_0|F_0}{|\mu|+|\mu_0|}\mathbf{P}(\Omega,\Omega_0)(1-\exp(-\frac{|\mu|+|\mu_0|}{|\mu||\mu_0|}\tau_m)), \tag{4.46}$$

This result gives the single scattering approximation of the radiance distributions.

For an optically thin layer, $\tau_m << 0$, we can further simplify Eq. 4.46 into:

$$\mathbf{I}_1(0,\Omega) = F_0\omega\mathbf{P}(\Omega,\Omega_0)\tau_m/|\mu|. \tag{4.47}$$

The dependency on the incident angle comes only from the phase matrix. The factor μ comes with the oblique viewing angle—we get the photon path length proportional to $1/\mu$ at this viewing angle. Since the radiance is constant through propagation for each particle on this path, eventually the total radiance will be proportional to $1/\mu$.

The total reflected irradiance can be obtained by integrating the radiance (phase function) over the upper hemisphere Ω^+:

$$F^+(0) = \int_{\Omega^+} I(0,\Omega)\mu d\Omega \tag{4.48}$$

$$= F_0\omega\tau_m B, \tag{4.49}$$

where the backscattering ratio B is defined as:

$$B = \int_{\Omega^+} P(\Omega,\Omega_0)d\Omega. \tag{4.50}$$

Therefore, the reflectance for the irradiance would be:

$$R = \frac{F^+(0)}{F_0|\mu_0|} = \frac{\omega}{|\mu_0|}\tau_m B \tag{4.51}$$

For normal incidence and a non-absorptive system, we have $R = \tau_m B$, where τ_m is the total optical depth of the plane parallel system. This can be used to estimate the total reflectance of a thin layer system.

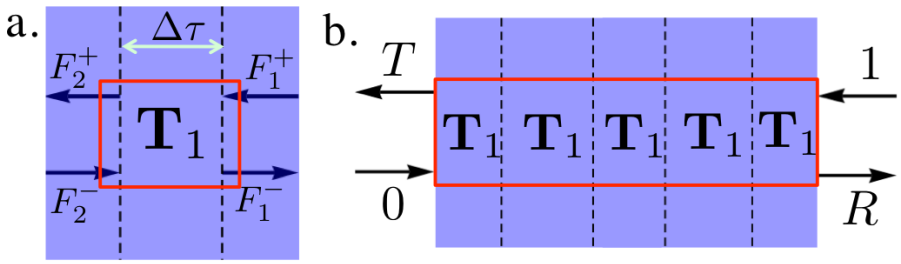

Figure 4.7: (a) Transfer matrix $\mathbf{T}_1$ for one layer. The incident irradiance are F_1^+ and F_2^-, and the scattered irraidance are F_2^- and F_1^+. (b) The transfer matrix for the whole system with incident irradiance 1, reflection R and transmission T. Transfer matrices are shown in the red box.

4.3.2 One Dimensional Model

Since the single scattering approximation can be only used in an optically thin system, here we will provide another treatment to consider an optically thick system. Kattawar and et.al. provided an exact solution for a one dimensional model [44]. In this model only the upwelling and downwelling fluxes are considered, and the final reflectance can be directly associated with the optical depth and the backscattering properties of the particles:

$$R = \frac{B\tau_m}{1 + B\tau_m}. \tag{4.52}$$

Here, we will provide an alternative approach to prove this result. Based on the single scattering approximation result, we will derive this equation using the transfer matrix method introduced in the last section.

Considering a system with total optical depth τ_m, we can divide this system into n thin layers each one with optical depth $\Delta\tau = \tau_m/n$, and $n \to \infty$. The transmission and reflection of such an one layer can be represented using a transfer matrix (Figure 4.7 (a)). We can solve the total transmission and reflection for the whole system using

a similar transfer matrix method. Here the energy flux (irradiance) is considered, not the electric field. Consider two sides of the single layer, denoted by 1 and 2, the downward and upward irraidance, denoted by (+) and (−). The scattering matrix, and the transfer matrix are defined as:

$$\begin{pmatrix} F_1^- \\ F_2^+ \end{pmatrix} = \mathbf{S}_1 \begin{pmatrix} F_1^+ \\ F_2^- \end{pmatrix}, \begin{pmatrix} F_2^+ \\ F_2^- \end{pmatrix} = \mathbf{T}_1 \begin{pmatrix} F_1^+ \\ F_1^- \end{pmatrix}. \tag{4.53}$$

The scattering matrix can be obtained similarly as discussed in the last section:

$$\mathbf{S}_1 = \begin{pmatrix} R_1 & T_1 \\ T_1 & R_1 \end{pmatrix}, \tag{4.54}$$

where R_1 and T_1 are the reflection and transmission for a thin layer, which can be solved using the single approximation results. Based on the scattering matrix, the transfer matrix can be obtained as:

$$\mathbf{T}_1 = \frac{1}{T_1} \begin{pmatrix} T_1^2 - R_1^2 & R_1 \\ -R_1 & 1 \end{pmatrix} = \frac{1}{1 - R_1} \begin{pmatrix} 1 - 2R_1 & R_1 \\ -R_1 & 1 \end{pmatrix}, \tag{4.55}$$

where the last step used the fact that energy is conserved, $T_1 + R_1 = 1$ for a non-absorptive system.

Therefore, the transfer matrix for the whole system (Figure 4.7 (b)) becomes:

$$\mathbf{T} = \mathbf{T}_1^n = \frac{1}{(1 - R_1)^n} \begin{pmatrix} 1 - 2R_1 & R_1 \\ -R_1 & 1 \end{pmatrix}^n, \tag{4.56}$$

where $R_1 = \Delta\tau B = B\tau_m/n$. Taking the limit of infinite layers, we can have:

$$\mathbf{T} = \lim_{n\to\infty} \frac{1}{(1-R_1)^n} \begin{pmatrix} 1-2R_1 & R_1 \\ -R_1 & 1 \end{pmatrix}^n \tag{4.57}$$

$$= \lim_{n\to\infty} \begin{pmatrix} 1-\frac{nR_1}{1-R_1} & \frac{nR_1}{1-R_1} \\ -\frac{nR_1}{1-R_1} & 1+\frac{nR_1}{1-R_1} \end{pmatrix} \tag{4.58}$$

$$= \begin{pmatrix} 1-\tau_m B & \tau_m B \\ -\tau_m B & 1+\tau_m B \end{pmatrix} \tag{4.59}$$

For the whole system, assume the light is only incident from one side of the system and with irradiance 1. Therefore, the transfer matrix can couple the reflectance R and transmittance $T = 1 - R$ for the system:

$$\begin{pmatrix} T \\ 0 \end{pmatrix} = \mathbf{T} \begin{pmatrix} 1 \\ R \end{pmatrix}, \tag{4.60}$$

the reflection from this one dimensional model can be solved as:

$$R = \frac{\tau_m B}{1+\tau_m B}, \tag{4.61}$$

and this results is consistent with Eq. 4.52.

5. NUMERICAL STUDIES ON LEUCOPHORES AND IRIDOPHORES *

Section 1 introduced the two types of cells: leucophores and iridophoers, which produce the structural color in the skin of cephalopods. Each cell also contains hundreds to thousands of small scatterers —such as small spherical structures called leucosomes for leucophores; and small layered structures called iridosomes for iridophores. Using the single scattering methods introduced in Section 3 and the multiple scattering methods introduced in Section 4, in this section we can investigate how leucophores and iridophores scatter light.

We will divide this section into two parts: the first dealing with iridophores and the second dealing with leucophores. In each part, we will first discuss the single scattering properties of a single scatterer (iridosome or leucosome), and then at the end we will study their diffuse reflectance with a collection of such scatterers. When discussing single scattering properties, we will emphasize the iridosomes more than the leucosomes, since the scattering properties of small spheres has been well studied [17, 16], but the novel finite layered structure of iridosomes has not been very well discussed.

From the multiple scattering simulations, we will show that different colors can be produced by the scatterers with different structures. A Monte Carlo code developed following the theory in Section 5 will be used to do the simulation.

5.1 Scattering Properties of Iridosomes and Iridophores

As discussed in Section 1 and shown in Figure 1.1, in the skin of cephalopods, there are many iridophores, and each of them contains numerous iridosomes. They

*Part of this section is reprinted with permission from M. Gao, Y. You, P. Yang, and G. W. Kattawar, "Backscattering properties of small layered plates: a model for iridosomes," Optics Express **20**, 25111-25120 (2012). Copyright 2012 by Optical Society of America.

can produce iridescent colors, such as green and blue, to further blend the colors produced by chromatophores, and help cephalopods to better match the background. Due to the layered structure of iridosomes, they can also produced polarized reflectance, which may serve as a channel for intraspecific communication [2]. In this section, we will first introduce the numerical model of a single iridosome, and then study various single scattering properties of it. Using these single scattering results as the input, we will study the multiple scattering properties of a collection of iridosomes, as a model for iridophores.

The single scattering properties are calculated using the DDA method as discussed in Section 3. The complete Mueller matrices and phase functions are obtained. The angular width of the reflection peak is found to depend on both the size parameter and the aspect ratio. The backscattering properties of small layered plates are studied for various size parameter values with respect to the plate thickness, plate aspect ratio, number of layers, incident direction, and polarization states of the incident light. The results are compared with the analytical results for semi-infinite plates. The criteria for using the reflectance of semi-infinite plates to approximate the backscattering efficiencies of finite size plates are quantified with respect to the number of layers, incident angle, and polarization state.

5.1.1 Numerical Model of an Iridosome

An iridosome is modeled as a cylinder with a layered inner structure. Two examples are shown in Figure 5.1 for both a single-layer and 5-layer plates. Plate diameter, thickness, and the total cylinder height are respectively denoted by D, d, and L. The direction of the incident light is at an angle β relative to the symmetry axis of the iridosome and is shown in Figure 5.1 (a).

The iridosome plate material is found to be a kind of protein, called reflectin,

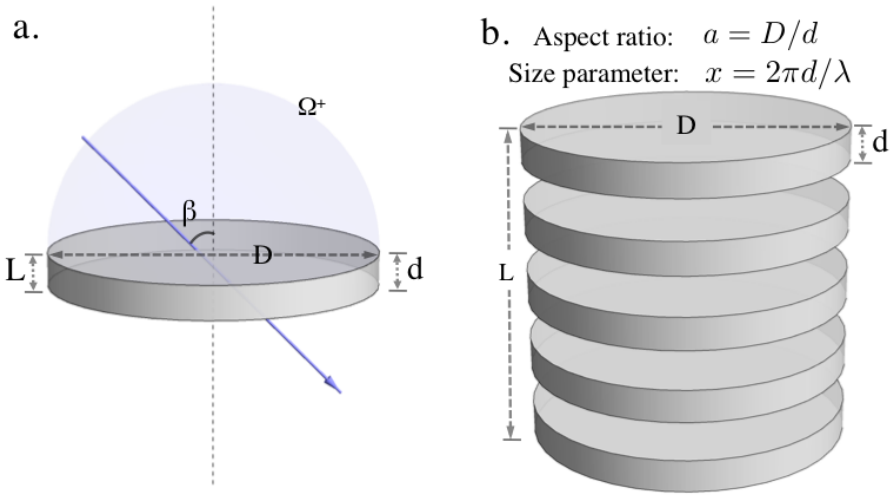

Figure 5.1: (a) A single layer plate. (b) A 5-layer plate.

and its refractive index is measured to be 1.591 ± 0.002 with a negligible dispersion in the visual spectrum [53, 54]. The material of the ambient tissue and that between plates are mainly cytoplasm, whose refractive index is close to that of water ($n_w = 1.33$). Thus, the relative refractive index of the plate (n_r) is 1.2 in reference to the cytoplasm. In our model, we choose the same relative refractive index for iridosomes. To further simplify the modeled structure, we consider ideal multiple-layered plates in which the optical length of the plates and the spacing between plates are the same, and therefore the spacing thickness is $n_r d$.

The size parameter is defined as $x = 2\pi d/\lambda$ for one layer of the plate, where λ is the wavelength in the medium. The plate thickness d of iridosomes can range from $50nm$ to $200nm$ [7, 8, 9, 10, 11, 12, 13], and, in the visual spectrum, the incident wavelength λ_0 in air is from 0.4 to $0.75\mu m$. Therefore, the size parameter of the plate thickness in the medium is $x = 2\pi n_w d/\lambda_0$, and can vary approximately from 0.5 to 5. This size parameter range is used in our simulations in steps of 0.1.

The aspect ratio is defined as $a = D/d$ upon one layer of the plate. For example, both single-layer and 5-layer plates in Figure 5.1 have the same aspect ratio of 10. A

range of the aspect ratio from 1 to 20 is chosen for our study. Rather than discussing the aspect ratio variations among certain cephalopod species, we focus on the aspect ratio's influence on the optical properties, from which a particular type of iridisome can be evaluated later on.

After discussing the single scattering properties of iridosomes, we will study the multiple scattering properties based on a modeled iridosome as shown in Figure 5.1(b) with 5 layers and each layer thickness $d = 100nm$; spacing $d_s = 120nm$; relative refractive index $n_r = 1.2$; and $r = 5d$ ($a = 10$). A collection of iridosomes with different orientations are shown to produce different colors.

To calculate the reflectance of a single-layer semi-infinite plate (R_1) (Figure 5.2), Airy's formula is used for different size parameters, polarization states, and both normal and oblique incidences [39]:

$$R_{1s,p} = \frac{4r_{s,p}^2 \sin^2\alpha}{\left(1 - r_{s,p}^2\right)^2 + 4r_{s,p}^2 \sin^2\alpha}, \tag{5.1}$$

$$r_s = \frac{\cos\beta - n_r \cos\theta}{\cos\beta + n_r \cos\theta}, \tag{5.2}$$

$$r_p = \frac{n_r \cos\beta - \cos\theta}{n_r \cos\beta + \cos\theta}, \tag{5.3}$$

where $\alpha = 2\pi n_r d \cos\beta/\lambda$ is a phase factor and related to the size parameter by $\alpha = n_r x \cos\beta$. As shown in Eqs. 5.2 and 5.3, r_s and r_p are the Fresnel reflectance formulas for the perpendicular and parallel polarized components relative to the principal plane defined by the direction of the incident and reflected light, where β is the incident angle and θ is the refracted angle. The reflectance is a periodic function of the size parameter x. Our analytical results for an arbitrary number of layers are derived by using the transfer matrix method as discussed in the last section, and the resulting reflectance remains a periodic function of the size parameter. Additionally,

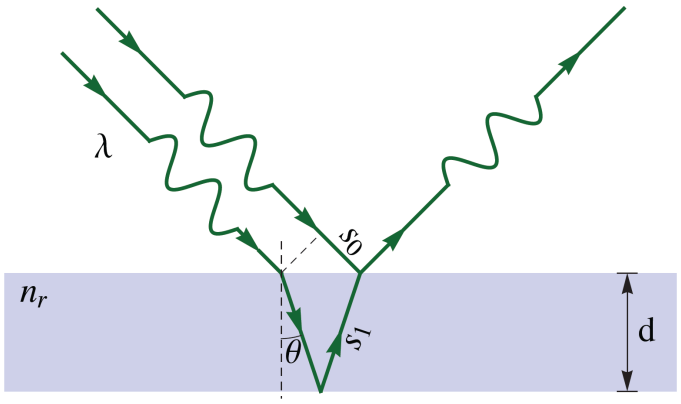

Figure 5.2: Illustration of the interference of the light reflected from the top and bottom surfaces of a semi-infinite plate with thickness d and relative refractive index n_r in the principal plane.

the maximum constructive and destructive interferences determine the maximum and minimum reflection of a semi-infinite plate. As shown in Figure 5.2, the difference in the optical lengths of the two reflection paths is $\Delta l = 2n_r s_1 - s_0 = 2n_r d\cos\theta$, where θ is the refracted angle. The phase factor in Eq. 5.4 can be related to the path difference by $\alpha = \pi\Delta l$ under normal incidence. Due to the $\lambda/2$ phase shift at the interface, the condition for maximum constructive interference is $\Delta l = (m + 1/2)\lambda$, where m is an integer. Thus, to have maximum constructive interference under normal incidence, we have$\alpha = \pi/2$ and $3\pi/2$, which corresponds to $x = 1.3$ and 3.9; to have maximum destructive interference, we have $\alpha = \pi$, which corresponds to $x = 2.6$. However, for a finite size system, the reflection maxima and minima deviate from the prediction of these size parameters, and to compare the difference we will indicate $x = 1.3$, 2.6, and 3.9 in the reflection spectrum graphs.

5.1.2 Phase Function of an Iridosome

The phase function $P(\Omega)$ describes the angular distribution of scattered light for an unpolarized light source, where $\Omega = (\theta_s, \phi)$ is the solid angle for the scattering direction (Section 2). ϕ is the azimuthal angle, and θ_s is the scattering angle between

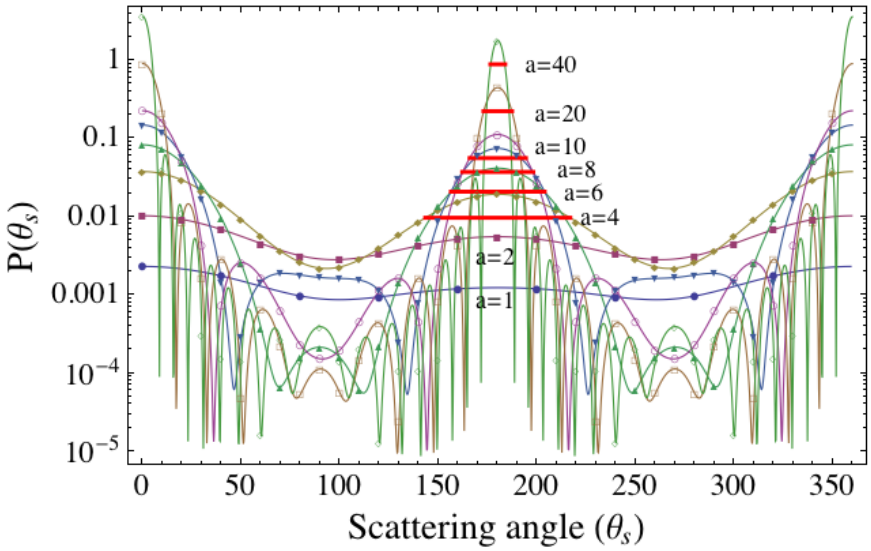

Figure 5.3: Phase function $P(\theta_s)$ with aspect ratio a ranging from 1 to 40 for a single-layer plate under normal incidence and size parameter $x = 1.3$. The FWHM of the reflection peaks ($\Delta\theta$) is indicated as a solid horizontal red bar. The aspect ratio, a, is shown close to its corresponding curve.

the scattering direction and the incident direction. The phase functions are calculated with various size parameters, aspect ratios, incident directions, and polarization states. We will discuss the angular distribution of the reflection peak in the phase functions, and how it depends on the incident angles.

For a size parameter $x = 1.3$ the phase functions are shown in Figure 5.3 with different aspect ratios under normal incidence. For convenience in comparing backscattering properties, each phase function is normalized by $k^2 C_g$ as in Eq. 5.4. Because the light is at normal incidence on the plates, the phase function is azimuthally symmetric. For example, as shown in Figure 5.3, the phase function is symmetric around $\theta_s = 180°$, which corresponds to the direct backscattering direction. The full width at half maximum (FWHM) of the reflection peaks is denoted by $\Delta\theta$ and provides a way to quantify the angular spreading of the reflection. When the aspect ratio a increases, the reflection peak around $\theta_s = 180°$ becomes narrower and $\Delta\theta$ decreases.

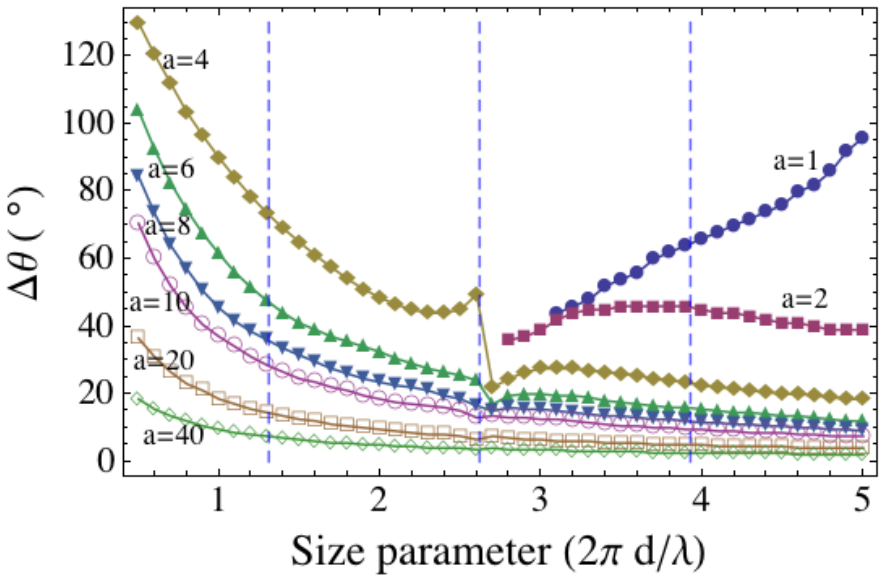

Figure 5.4: The FWHM of the reflection peak ($\Delta\theta$) versus the plate thickness size parameter for a single-layer plate. The aspect ratio is a. Vertical dashed lines are for size parameters $x = 1.3$, 2.6, and 3.9.

The FWHM of the reflection peak is shown by the horizontal red solid bar in Figure 5.3. For the aspect ratio from 4 to 40, $\Delta\theta$ is found to decrease from 73.5° to 7.5° with an angular resolution of 0.5°. For an aspect ratio of 1 or 2, no angle corresponds to the phase function with a value half of that at 180°, and, therefore, no value for $\Delta\theta$ exists; the phase function has less variations compared with the one with large aspect ratio particles.

For size parameters in the range from 0.5 to 5, the values of $\Delta\theta$ are summarized in Figure 5.4 with the same 0.5° angular resolution. $\Delta\theta$ decreases as the aspect ratio increases throughout all the considered size parameters. For aspect ratios $a = 1$ and 2 and size parameters approximately less than 2.6, no value exists for $\Delta\theta$. For size parameters larger than 2.6 and $a = 1$, $\Delta\theta$ can be found between 44° to 96°, and for $a = 2$, $\Delta\theta$ decreases to between 36° and 46°. Furthermore, when $a = 4$, $\Delta\theta$ is between 130° and 18.5° for size parameters from 0.5 to 5. When $a = 40$, $\Delta\theta$ further

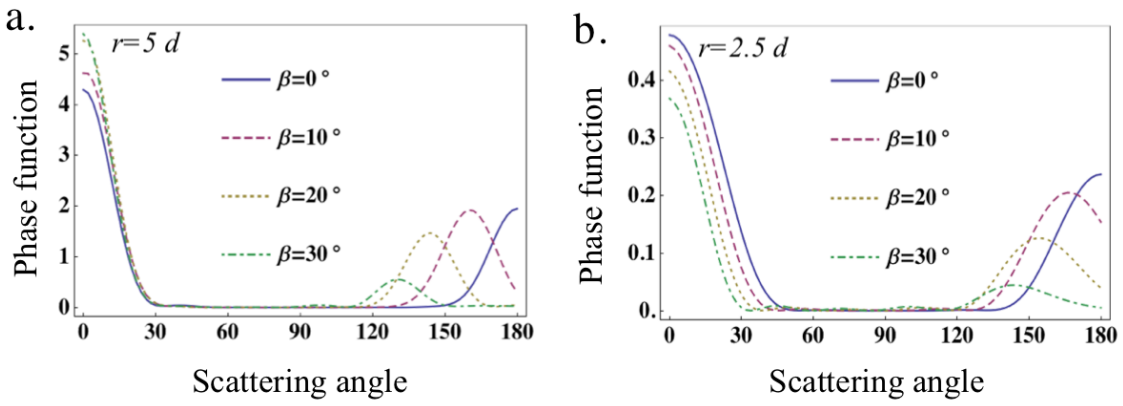

Figure 5.5: Phase functions of the tilted 5-layered structure in the y-z plane, with incident angle β varying from 0° to 30° as shown in the legend, incident wavelength $480nm$. Aspect ratio $a = 10$ (a) and $a = 5$ (b)

.

decreases to between 18.5° and 2° for the same range of size parameters. For the plates with a thickness of 5 and $a = 40$, the reflection peak is at least 2° in width. The spreading becomes less prominent when the aspect ratio is large. However, for the semi-infinite plates, the reflection is confined to a single direction determined by Snel's law. The angular broadening of the reflection can be explained by the ray-spreading effect [55]. When the angular distribution is considered either for a phase function or the diffuse reflection of a random system, the influence of the spreading of the reflection peak needs to be evaluated.

When light is incident with an incident angle β, the reflection peak of the phase function can be roughly predicted as in the specular reflection direction $180 - 2\beta$, as shown in Figure 5.5. But the magnitude is rapidly decreasing with the increase of β. And the reflection peak is not located exactly at $180 - 2\beta$ with large incident angles. When the aspect ratio decreases from 10 to 5, the reflection peaks move further towards the backward direction. Moreover, when the scattering angle is larger than 40°, the reflection peak becomes vanishingly small.

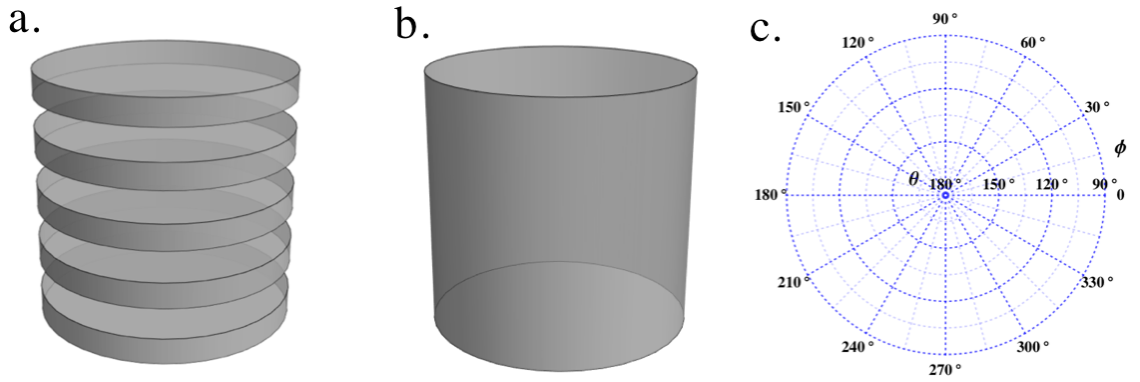

Figure 5.6: (a). A 5 layer iridosome used in our numerical model. (b). A solid cylinder with the same radius and total height as the iridosome in (a). (c) Angular distribution diagram for backscattering.

5.1.3 Mueller Matrix of an Iridosome

We have introduced the Mueller matrix in Section 2, which contains all the elastic scattering information of a scatterer. In this section, the reduced backscattering Mueller matrices of a five-layer iridosome are compared with a cylinder with the same radius and total height (Figure 5.6(a) and (b)). We will see the angular distribution of the Mueller matrix elements are sensitive to particle shapes and structures. Since the real iridosomes in the skin of cephalopods can have a wide range of shapes and sizes, and their structure has not been well studied, Mueller matrix imaging [56] could provide a useful way to classify iridosomes through their scattering patterns as shown in the following.

The angular distribution of the Mueller matrix is represented using the diagram in Figure 5.6(c). The size parameter of one layer thickness is $x = 1.3$; the radius of the iridosome and cylinder is $r = 5d$ (aspect ratio $a = 10$). The angular distribution diagram is shown in Figure 5.6(c), which will be used to represent Mueller matrix distributions later. The reduced Mueller matrix (elements except m_{11} are divided by m_{11}) is used in our discussion.

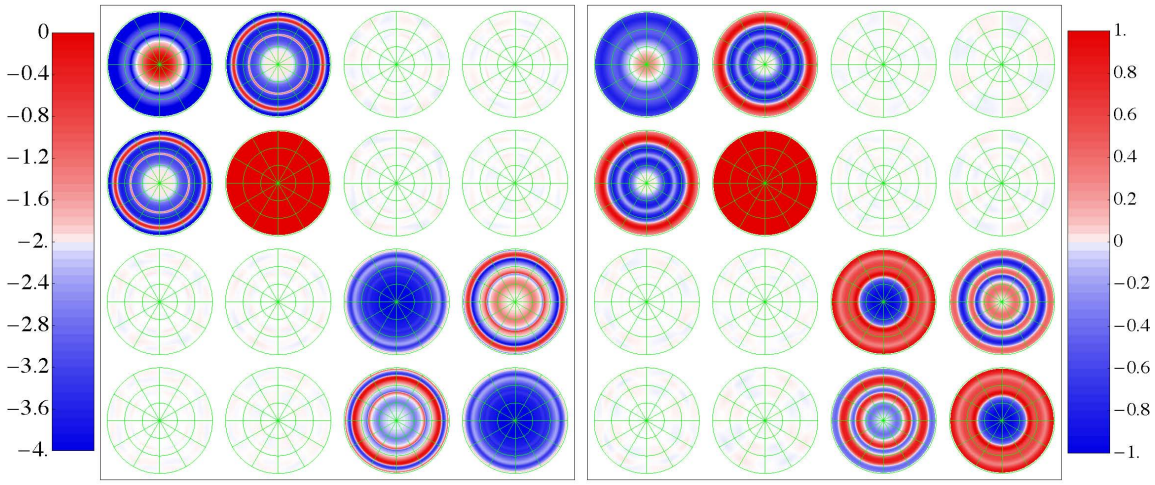

Figure 5.7: Angular distribution of the reduced backscattering Mueller matrix with incident angle $\beta = 0°$, and wavelenth $480nm$. (a) 5 layer iridosome, (b) solid cylinder with the same radius and total height. m_{11} is plotted on a log scale with the color bar on the left; the right color bar is for all other reduced elements.

The Muller matrices are compared for three different incident angles, including $\beta = 0°, 30°$ and $90°$, as plotted in Figures 5.7, 5.8, and 5.9. The left panel (a) is for the 5 layer iridosome, and the right panel (b) is for the solid cylinder. The color bar on the left is for m_{11} on a log scale, and the color bar on the right is for all the other reduced Mueller matrix elements with values in the range of $[-1, 1]$. Observed from these three figures, the diagonal 2×2 blocks of the Mueller matrices are symmetric with respect to the principal plane ($y - z$ plane with $\phi = 90°$ and $270°$), while the off-diagonal 2×2 blocks are anti-symmetric, namely with the same absolute value but opposite sign. This is because of the mirror symmetry of the amplitude matrix on the two sides of the principal plane [17].

The backscattering can be greatly enhanced by interference due to the multilayer structures. As shown in Figure 5.7, the reflection peak of the phase function m_{11} of (a) is approximately 10 times stronger than the peak in (b). The pattern of the other elements of (a) and (b) are very similar when $\beta = 0°$, since the top view of both

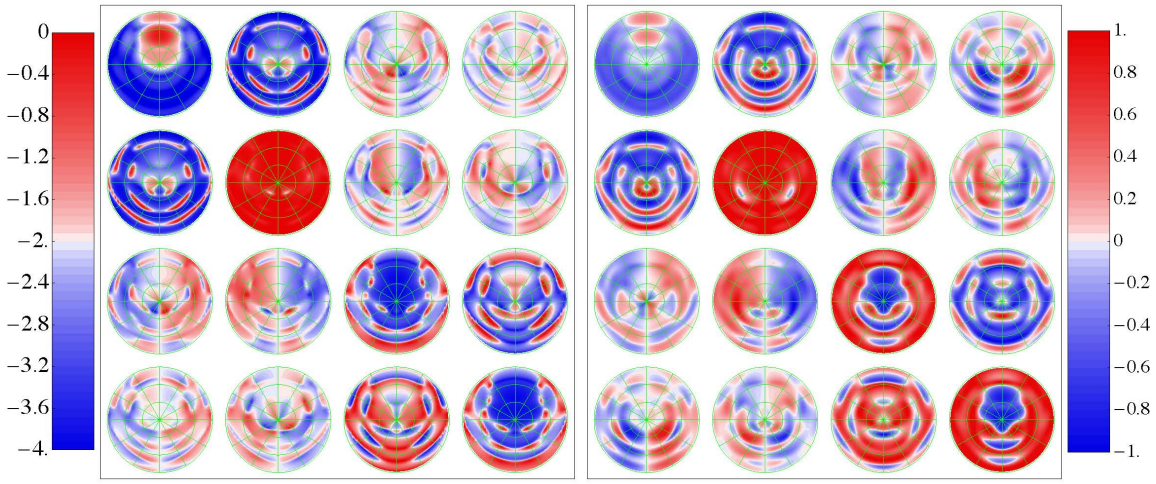

Figure 5.8: Same as Figure 5.7, but for an incident angle $\beta = 30°$.

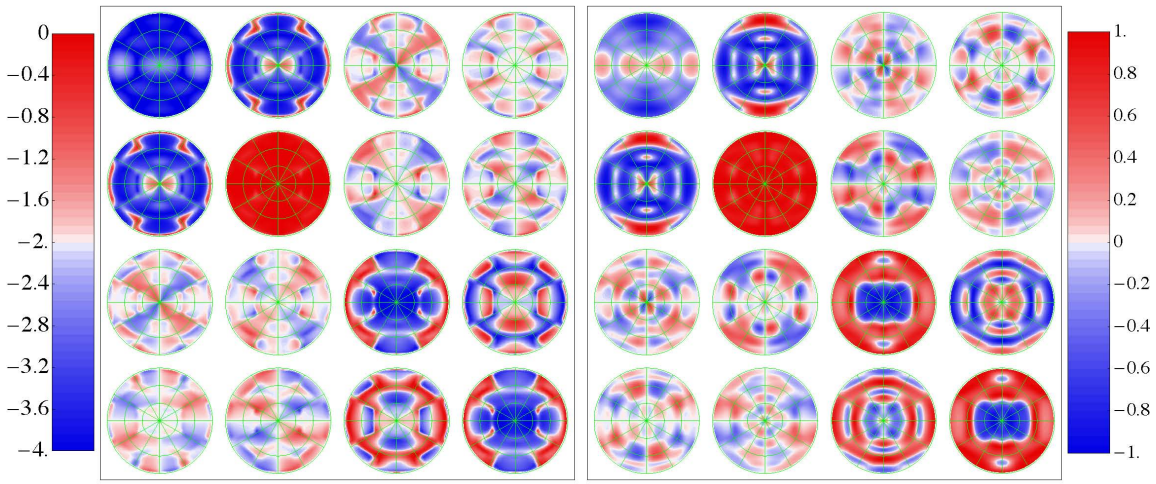

Figure 5.9: Same as Figure 5.7, but for an incident angle $\beta = 90°$.

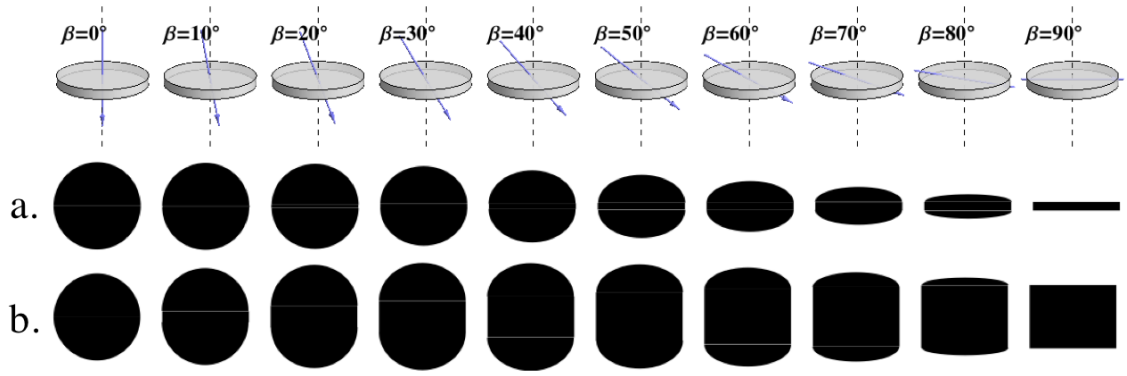

Figure 5.10: The projected geometric areas (C_g) which are perpendicular to the incident direction are shown for (a) a single-layer plate and (b) a 5-layer plate. Incident angle β is from 0° to 90°.

structures are the same. But this phenomenon changes when the incident angle is increased to $\beta = 90°$, as shown in Figure 5.9, where the two patterns are completely different: for example, in (a) there is a reflection peak in the center, but in (b) it splits into two peaks around the center, since now the light is incident on the side of the iridosome, which sees a totally different structure for the layered iridosome compared with the smooth surface of solid cylinder. In Figures 5.7 and 5.8, although they share similar scattering pattern, the scattering maximum and minimum for the 5 layer iridosome in (a) are confined to a much smaller region compared with the solid cylinder in (b).

5.1.4 Backscattering Efficiency of an Iridosome

In this section we will discuss another important physical quantity , called backscattering efficiency, which characterizes the backscattering properties, and can be used to estimate the multiple scattering reflection through the one dimensional model we introduced in Section 4.

As shown in Figure 5.1 (a), the upper solid angle hemisphere Ω^+ is defined as the backscattering region. For unpolarized incident light, the integration of the phase

function over this region is used to obtain the backscattering efficiency:

$$Q_b = \frac{1}{k^2 C_g} \int_{\Omega^+} P(\Omega) d\Omega, \tag{5.4}$$

where $k = 2\pi/\lambda$ is the wavenumber, and $C_g = \pi D^2 \cos\beta/4 + DL \sin\beta$ is the projected geometric area of the cylinder. Note that the projected geometric area is perpendicular to the incident direction. Two sets of examples of the projected areas are shown in Figure 5.10 for both single-layer and 5-layer plates. Furthermore, when the aspect ratio approaches infinity, the backscattering efficiency becomes equal to the reflectance of the semi-infinite plate. Therefore, we use the backscattering efficiency as an indicator to show the reflection deviation of the small plates from that of the semi-infinite plates.

For a bulk system with random positioned scatterers, Q_b can be used to estimate the diffuse reflectance. Here, the diffuse reflectance is for the irradiance and no angular distribution is present. The diffuse reflectance is important in determining the optical appearance of the system, such as the color and brightness of the cephalopod skin. Normally the calculation involves solving a 3-D radiative transfer equation, but the irradiance reflectance can also be calculated by using the one dimensional model introduced in Section 4 : if the number density is n_d and the system thickness is L, the diffuse reflectance is $R_{diff} = C_b n_d L/(1 + C_b n_d L)$, where $C_b = Q_b C_g$ is the backscattering cross section. Therefore, the backscattering efficiency of one scatterer is directly related to the diffuse reflection of a bulk system.

Throughout this section, we will compare the backscattering efficiency with the reflection of semi-infinite plates. In this way, we can understand how the scattering properties of a finite structure differs from that of semi-infinite plates. We can also determine the criterion for using the reflection to approximate the backscattering

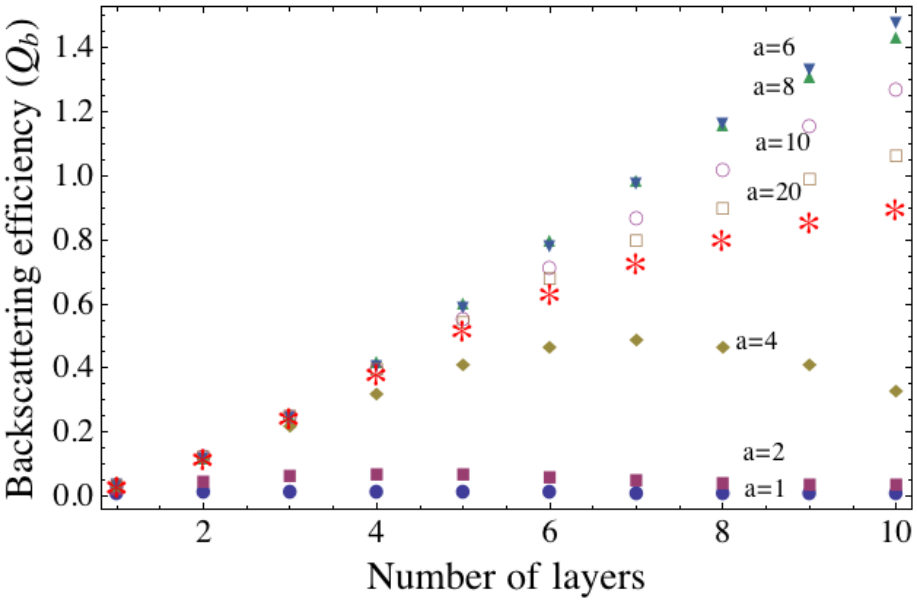

Figure 5.11: Backscattering efficiency Q_b versus number of layers for a size parameter of the plate thickness $x = 1.3$ with different aspect ratios and under normal incidence. The reflection for semi-infinite plates is indicated by asterisks.

efficiency, which can be used to study iridosomes with large aspect ratios. Here we will compare the numerical results for finite plates with the reflectance of the semi-infinite plates.

The theoretical results for the reflection of the semi-infinite plates can be solved using the transfer matrix method as discussion in Section 3. The DDA method, as introduced in Section 3, is used to calculate the single scattering properties of an iridosome. For multiple layered system, we have to numerically calculate their reflectance using the TMM.

The backscattering efficiency Q_b (Eq. 5.4) is sensitive to the aspect ratio and the number of layers of an iridosome. As the aspect ratio increases, Q_b will undergo a metamorphosis from a small particle to a semi-infinite layered plate. In Figure 5.11, Q_b is shown for various numbers of layers and aspect ratios at $x = 1.3$. When the radius increases, Q_b approaches the reflection of the semi-infinite plates (red asterisks

in the graph) for each number of layers. When $a = 1$ or 2 and the number of layers is larger than 1, Q_b is much smaller than the reflection of semi-infinite plates. When $a = 4$, Q_b will decrease as the number of layers increase when the number of layers is larger than 7. In general for $a > 4$, as shown in Figure 5.11, adding more layers of plates into the scattering will increase the backscattering efficiencies as predicted by the semi-infinite plates. The size effect plays a significant role for small scatterers in determining the backscattering efficiency. Meanwhile, Q_b can be larger than 1 due to the interference effects of the scattered waves similar to the phenomenon that causes extinction [17].

For normal incidence, the backscattering efficiency Q_b versus the size parameter for a single-layer and a 5-layer plate is compared with the semi-infinite results in Figure 5.12. With large aspect ratios, such as $a = 20$, the backscattering efficiency can be approximated with great accuracy by using the results from the semi-infinite plates. When the aspect ratio decreases, two maximum reflection peaks remain observed, but the positions shift to shorter wavelengths and the values generally differ more from the semi-infinite results. For example, when $a = 1$, as shown in Figure 5.12 (a) and (b), one of the Q_b maxima around $x = 2.6$ becomes the minimum for the semi-infinite plate. Since the radius of the plates is very small, unlike the semi-infinite plates, the interference effects between the top and bottom interface of the plates become unimportant in determining Q_b.

To quantify the error of using the semi-infinite results to approximate the backscattering efficiency (Q_b), we defined a quantity Q_{error} by comparing the value of the maxima between the finite and semi-infinite plates: $Q_{error} = |(Q_{b,max} - R_{max})/(Q_{b,max} + R_{max})|$, where $Q_{b,max}$ is the maximum backscattering efficiency for the finite plates and R_{max} is the maximum reflectance for the semi-infinite plates. A smaller Q_{error} means less difference between the maxima of these two kinds of plates, and, as ob-

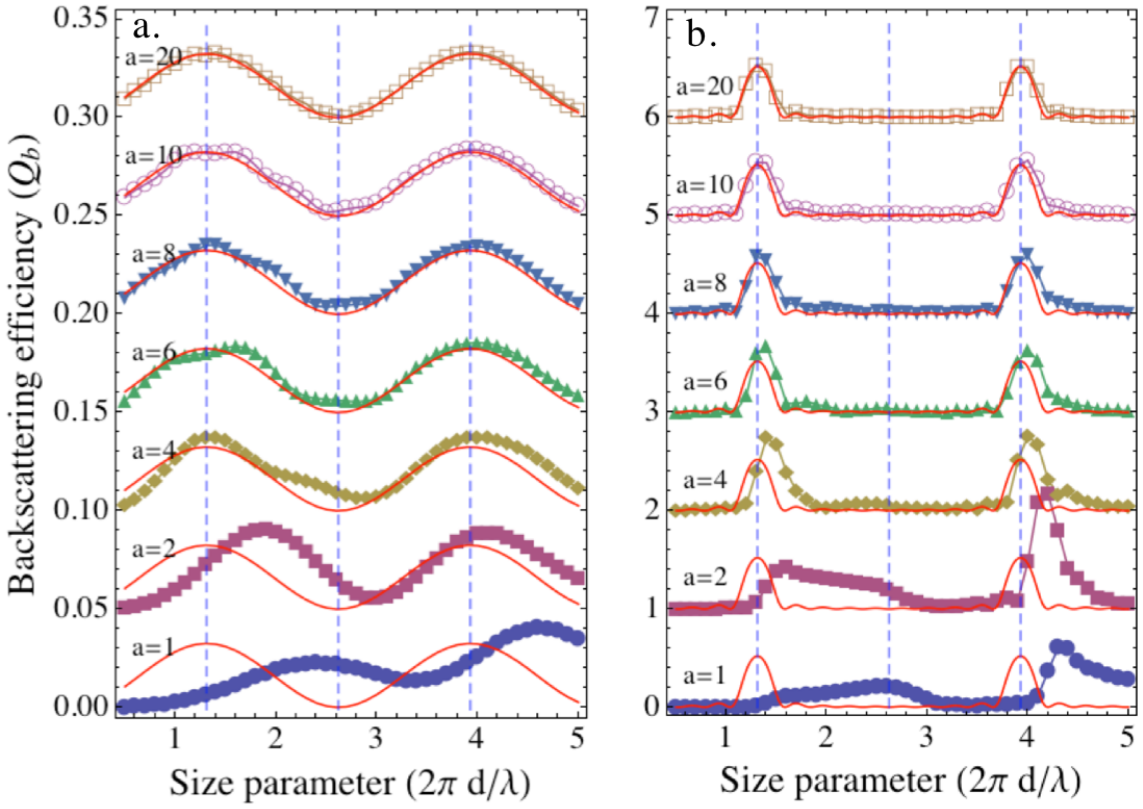

Figure 5.12: Backscattering efficiency Q_b versus size parameter $x = 2\pi d/\lambda$ of the plate thickness at different aspect ratios under normal incidence. The reflection for semi-infinite plates is indicated by solid red lines. (a) Results for a single-layer plate. Each curve is successively moved upward by 0.05. Maximum reflection of the semi-infinite plates is 0.033 at $x = 1.3$ and 3.9. (b) Results for 5-layer plate. Each curve is successively moved upward by 1.0. Maximum reflection of the semi-infinite plates is 0.52 at $x = 1.3$ and 3.9. The step for the size parameter in the calculation is 0.1. Vertical dashed lines are for the interference maxima with size parameter $x = 1.3$, 2.6, and 3.9.

served from Figure 5.12, when the maxima are close, the wavelengths for the locations of those maxima are also close to each other. We choose a Q_{error} of less than 10% as an acceptable criterion to use the semi-infinite approximation. Therefore, from Figure 5.12, for single-layer plates, the aspect ratio must be larger than 4, and for a 5-layer plate, the aspect ratio must be larger than 8. A larger layer number requires a larger aspect ratio. With an aspect ratio $a = 10$, for a single-layer plate, $R_{max} = 0.033$ at both $x = 1.3$ and 3.9, $Q_{b,max} = 0.035$ at $x = 1.4$, and $Q_{error} = 4\%$; for a 5-layer plate, $R_{max} = 0.52$ at both $x = 1.3$ and 3.9, $Q_{b,max} = 0.60$ at $x = 4.0$, and $Q_{error} = 7\%$. At this aspect ratio, both the single-layer plate and the 5-layer plate have $Q_{error} < 10\%$ and, therefore, to further study the dependency of backscattering efficiency on the incident angles we use $a = 10$ for both the single and 5-layer plates.

The angular dependence of the backscattering efficiency (Q_b) can be used to study the response of different incident polarizations on the small plates backscattering. The results are shown in Figure 5.13 and Figure 5.14, for angle intervals of 10° and an aspect ratio of 10 for both perpendicular and parallel polarization states. To have $Q_{error} \leq 10\%$ for the single-layer plate, we need an incident angle $\beta \leq 30°$ for a parallel polarized component, and $\beta \leq 50°$ for a perpendicular component. However, for the 5-layer plate to have the same $Q_{error} \leq 10\%$, we need $\beta \leq 10°$ for both polarizations due to the large fraction of edge compared to the total projected area. Therefore, the perpendicular component provides a better approximation compared with the parallel polarized component for both the single-layer and 5-layer results. The reflectance of semi-infinite plates approaches unity for all size parameters as the incident angle approaches 90°. Since the light is incident directly on the edges of the plates, the backscattering efficiencies is completely different from the reflection, and we cannot use the reflection of semi-infinite plates to approximate Q_b for large

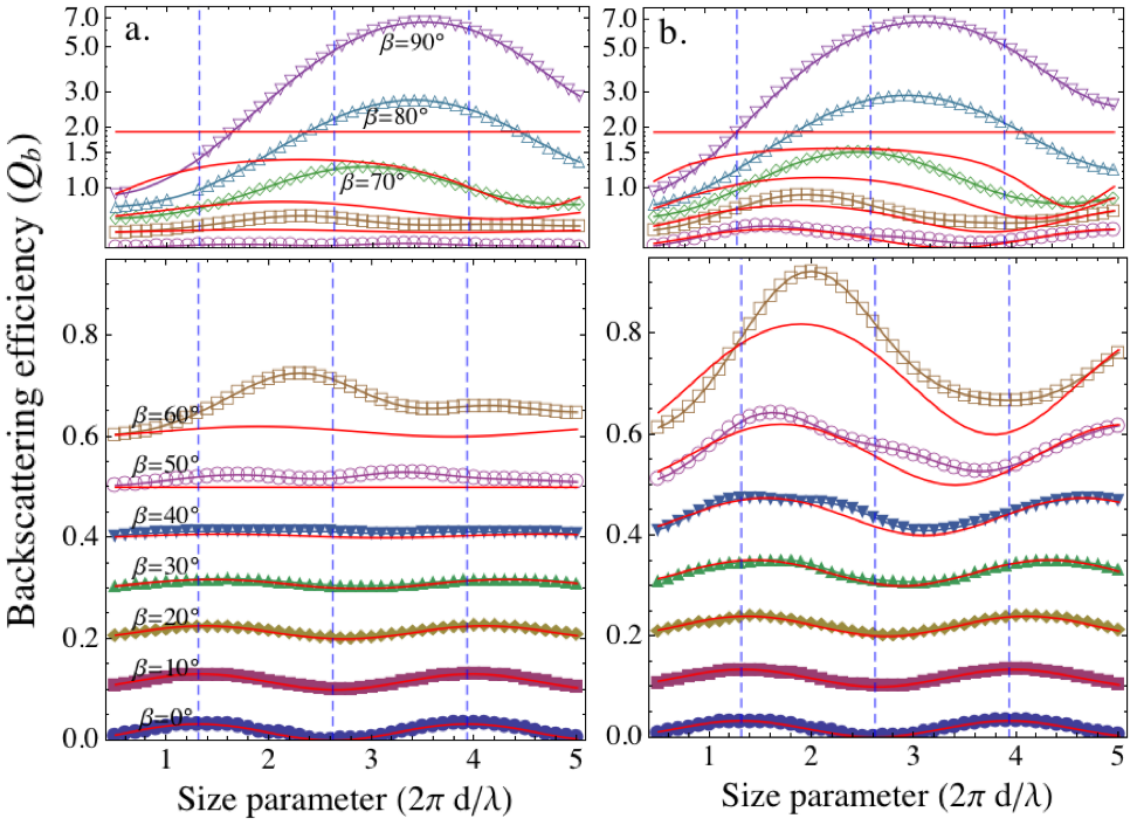

Figure 5.13: Same as Figure 5.12 but for a single-layer plate with an aspect ratio 10 and varying incident angles β. Incident light is polarized in (a) parallel direction and (b) perpendicular direction relative to the principal plane. Each curve is successively moved upward by 0.1. All results are plotted on a linear scale except forβ = 70°, 80°, and 90° which are plotted on a log scale.

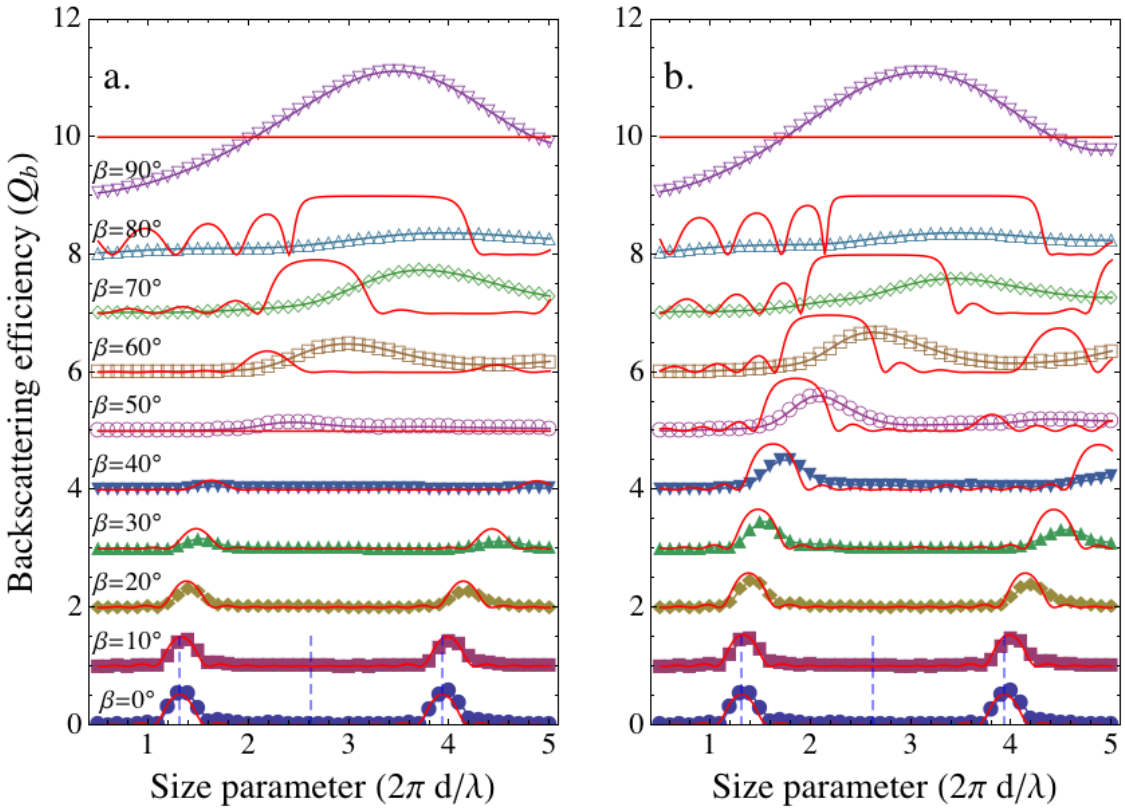

Figure 5.14: Same as Figure 5.13 but for a five-layer plate. Each curve is successively moved upward by 1.0.

incident angles.

The semi-infinite plates will respond differently to different incident polarization states; the reflectance of the parallel-polarized incident light will vanish at the Brewster angle, leaving the reflected light totally polarized in the direction perpendicular to the principal plane. As shown in Figure 5.13 and Figure 5.14, we found similar behaviors for both the single and 5-layer finite size plates. We compared the maximum reflectance for each incident angle, and found the minimum value for single-layer plates to be 0.013 and for 5-layer plates to be 0.06, and both to occur at $\beta = 40°$. The angle is smaller than the Brewster angle of 50.2° for the relative refractive index $n_r = 1.2$. Moreover, these two values are 37% and 10% of their corresponding maximum Q_b at normal incidence, while for the semi-infinite plates the value of the minimum reflectance of the parallel polarized light will be zero at the Brewster angle. This constitutes another prominent difference between finite and semi-infinite plates.

5.1.5 Extinction Matrix of an Iridosome

After we understand the angular distribution of the polarized scattered light. We need to understand the transmission properties of iridosomes; this is described by the extinction cross section. As we discussed in Section 2, the extinction cross section for a non-spherical particle would depend on the incident polarization states, and we have to use a 4×4 extinction matrix to describe it. The extinction matrix can be related with the transmission properties through a generalized Bouguer-Lambert-Beer law (Section 4, Eq. 4.24).

Generally, the extinction matrix is a function of the incident wavelength and iridosome orientation. For a spherical particle or the particle with random orientations, the extinction matrix reduces to a diagonal matrix, specified solely by the extinction cross section, C_{ext}, for the unpolarized incident light. For non-spherical particles,

there are two other important elements: C_{pol} and C_{cpol}; we will discuss their physical meanings in what is to follow. In this section, we will also compare the extinction efficiency matrix $\mathbf{Q}$ (with three corresponding elements Q_{ext}, Q_{pol} and Q_{cpol} with the semi-infinite plates for various incident angles. And we will show for large aspect ratio iridosomes, their extinction matrix is very close to the semi-infinite plates. Therefore the results for semi-infinite plates can be used to efficiently estimate the extinction matrix for finite size plates.

C_{pol} describe the cross section different between parallel and perpendicular direction (Section 2). The corresponding extinction cross sections for the incident light polarized along these parallel($\hat{l}$) and perpendicular directions($\hat{r}$) are:

$$C_l = C_{ext} + C_{pol}, \quad C_r = C_{ext} - C_{pol}. \tag{5.5}$$

C_{cpol} describes the birefringent effect of the scattering by iridosomes. It introduces a phase difference between the parallel and perpendicular component of the electric field, $\phi_l - \phi_r = -\tau_{cpol}$. Because of this, the circular polarized light field can be generated through the non-zero U component of the incident Stokes vector, and the relative amplitude between U and V components will oscillate with the increase of path length. Meanwhile, both the U and V components will become unimportant compared with the I and Q components of the forward transmitted light field at large path lengths, as can be seen from Eq. 4.24 in Section 4.

The forward scattering amplitude matrix of a single layer cylindrical plate is calculated using the DDA method as discussed in Section 3. After obtaining these matrices, we use Eq.2.37 to calculate the extinction matrices. The extinction efficiency matrix can thus be determined by dividing the projected geometric area, as shown in Figure 5.10. The three independent elements, Q_{ext}, Q_{pol} and Q_{cpol} for the

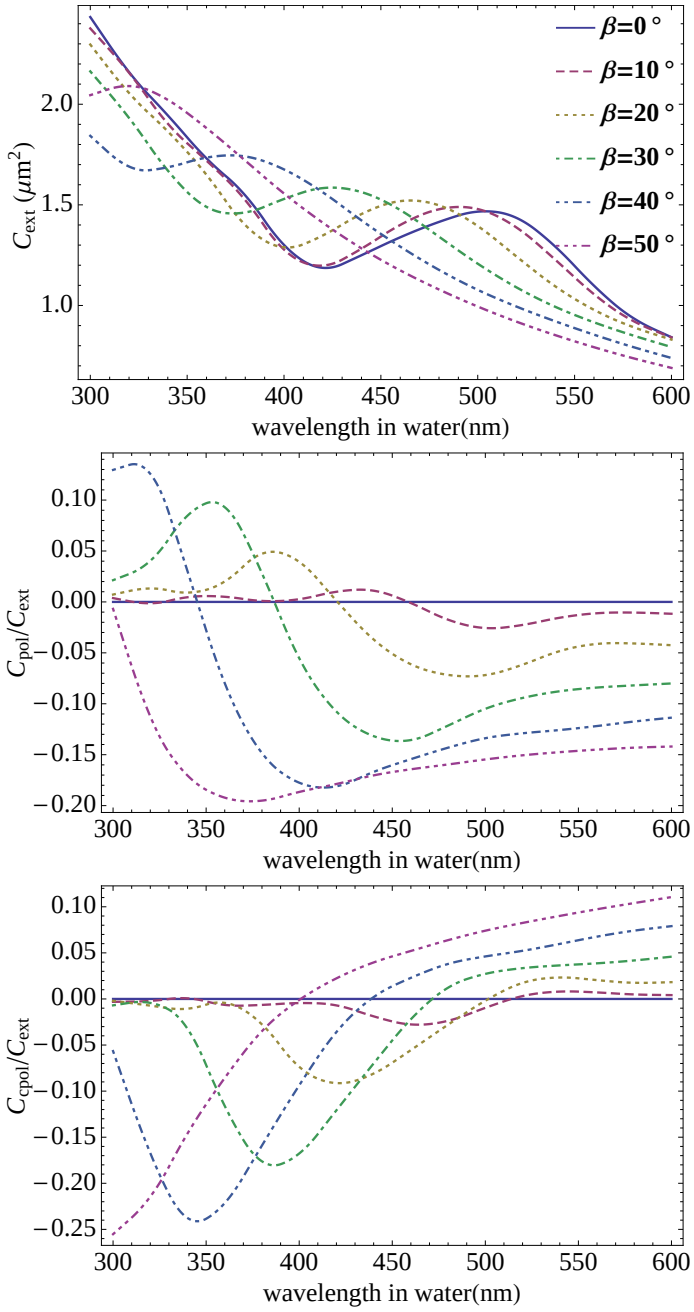

Figure 5.15: Elements of extinction matrix with various incident angles and wavelengths for 5 layer iridosome with aspect ratio $a = 10$ and one layer thickness $d = 100nm$; refractive index $n_r = 1.2$ (size parameter $x = 1.3$).

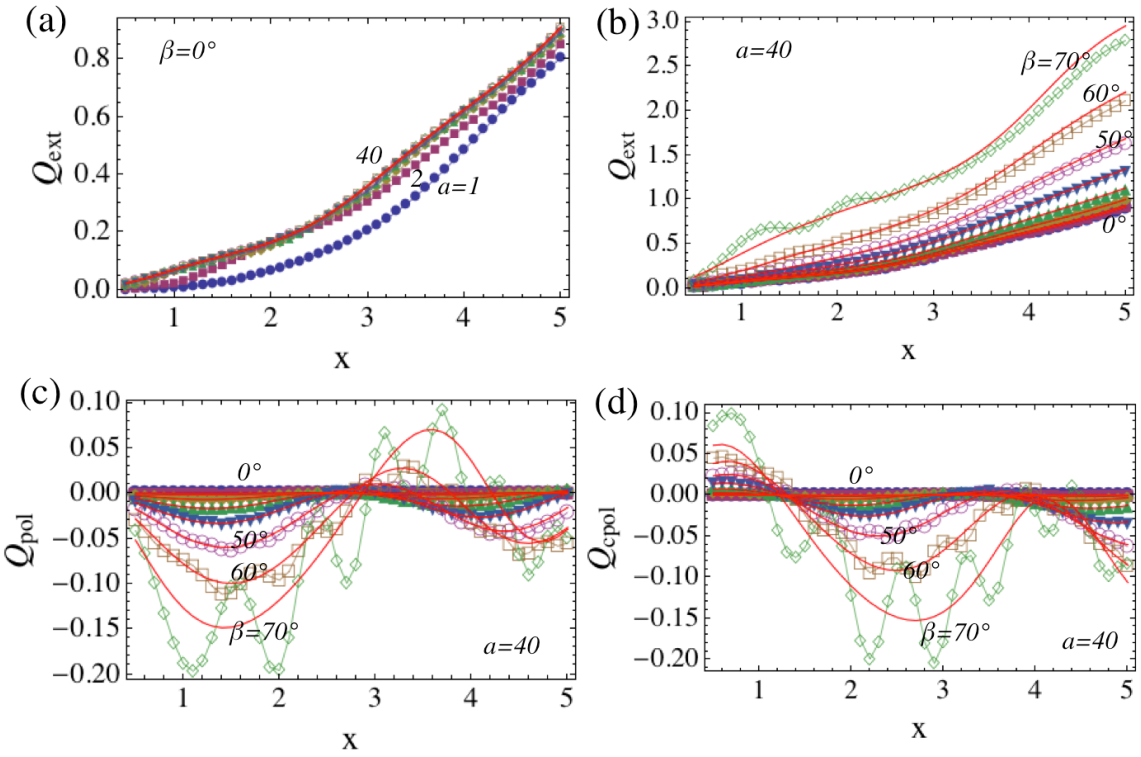

Figure 5.16: (a) Q_{ext} vs size parameters x with different aspect ratios $a = 1$, 2, 4, 6, 8, 10, 20 and 40 at incident angle $\beta = 0°$. The results with $a = 4$, 6, 8, 10, 20 and 40 are almost identical with the theoretical results. The red solid line is the results of semi-infinite plates at normal incidence. (b) Q_{ext} vs size parameters x at different incident angles from $\beta = 0°$ to 70° with aspect ratio $a = 40$. The red solid line is for the results of semi-infinite plates with the same range of incident angles. (c) same as (b) but for Q_{pol}. (d) same as (b) but forQ_{cpol}.

same 5 layer iridosomes with aspect ratio $a = 10$ as discussed in the last section are shown in Figure 5.15. In our studies, we find both the C_{pol} and C_{cpol} are important at some angle-wavelength range—they can be as high as 20% relative to C_{ext}, and can't be simply neglected.

To understand how the extinction matrix elements various with the aspect ratio $a = D/d$ we chose a series of aspect ratios $a = 1, 2, 4, 6, 8, 10, 20, 40$ to determine its influence, and when the finite plates can have a similar extinction matrix as the semi-infinite plates. The range of the size parameter is chosen in the same way as in

the last section where x varies from 0.1 to 5. From our results, the finite system with large aspect ratios can indeed be understood from the results of the semi-infinite plates, and the extinction is determined solely by the generalized optical theorem in Section 2.

The incident angle β is relative to the axis of the plates (Figure 5.1). The results for $\beta \leq 70^\circ$ are shown in Figure 5.16. For larger incident angles, the extinction matrices deviates more and more from the semi-infinite results as denoted by the solid red lines. The analytical results for $\beta = 0$ is calculated by using Eq. 2.53 in Section 2, which are almost the same as the results produced by the finites plates. We can see Q_{ext} is smaller than the semi-infinite results for relatively larger size parameters. For both Q_{pol} and Q_{cpol}, small incident angles produce excellent agreement between the finite and semi-infinite plates. When incident angle increases, such as up to 60° and 70°, comparing the results with $a = 20$ and $a = 40$, the results a=40 has more oscillations but smaller variations around the analytical results for the semi-infinite results.

When the aspect ratio $a \leq 4$, the extinction efficiency is close to the results of the semi-infinite plates shown by the red solid line at normal incidence $\beta = 0^\circ$. As shown by Figure 5.16 (a), the extinction efficiency results for $a = 4, 6, 8, 10, 20, 40$ overlap to each other. Q_{pol} and Q_{cpol} are always zero for normal incident light.

The dependency of the extinction on the incident angles is shown in Figures 5.16 (b),(c), and (d). For the plates with aspect ratio $a = 40$, the extinction efficiency as shown in Figure 5.16 (b) shows the semi-infinite results are almost indentical for incident angles up to 40°. When the incident angle increase even up to 70°, the semi-infinite results are still close to the finite plates results. Similarly, for polarized and circular polarized extinction efficiency as shown in Figures 5.16 (c) and (d), the results of semi-infinite plates remain a good approximation for incident angles up to

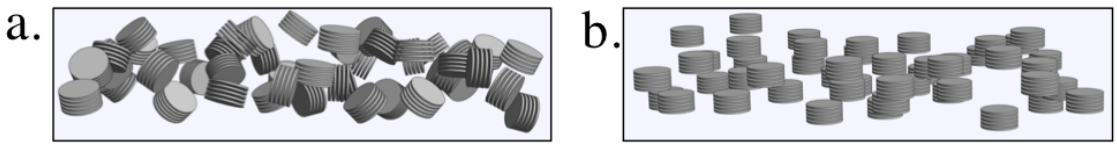

Figure 5.17: Orientation distributions of a collection of iridosomes: (a) random orientations, and (b) vertical orientations.

40°. When the angles keep increasing, the results of finite plates start to oscillate around the semi-infinite results with larger and larger amplitudes.

The DDA results are based on the spherical wave formalism as shown in Section 3. The agreement with the simulation and the analytical results proves the resemblance between the plane wave formalism and the spherical wave formalism for thin plates in calculating the extinction efficiency matrix.

5.1.6 Diffuse Reflection of Iridophores

Here we present our modeling for the skin layers with iridophores, which are modeled as a collection of iridosomes. The skin layer thickness, and iridosome size and number density were retrieved from the electron micrograph of *Octopus vulgaris* as shown in Figure 1.1. The thickness is about $10\mu m$ and the number density of the iridosomes is around $1/\mu m^3$. To solve the light scattering in such a system, we need the single scattering properties of one iridosome; the same structure of the 5 layer iridosomes are used as in the previous sections.

Since the iridosome layer is very complex, so we will try to approximate the system between two limits: a uniform layer with random orientated iridosome (Figure 5.17 (a)), and the layer with iridosome oriented in a vertical direction (Figure 5.17 (b)). The multiple scattering modeling of these two distributions are also discussed in Section 4.

For the random orientations, the scattering coefficients are obtained by multiply-

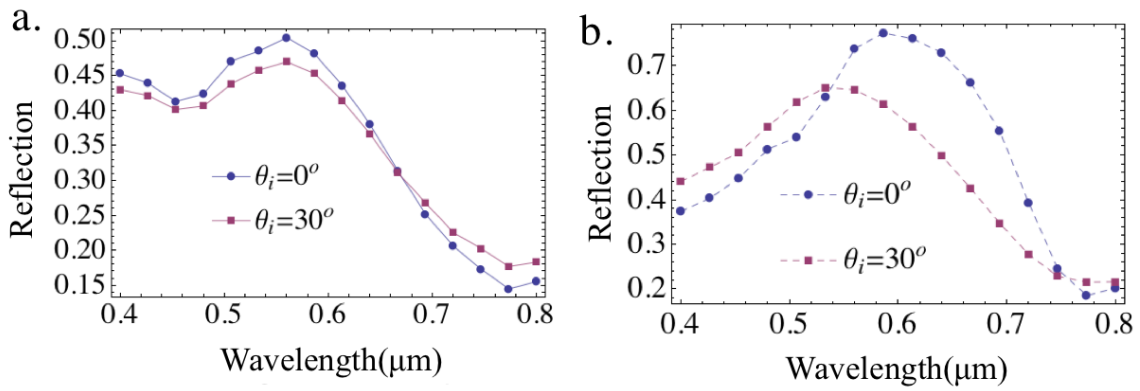

Figure 5.18: The diffuse reflection vs. incident wavelength (in vacuum) of an iridophore system for (a) random orientations, and (b) vertical orientations.

ing the scattering cross section by the numder density of iridosome ($1/\mu m^3$). For the incident angle at 0° and 30°, we get similar reflection spectra, and similar peak locations, as shown in Figure 5.18(a). For both incident angles, the diffuse reflectance spectra are similar to each other. Therefore, for a randomly oriented system both the intensity and color can remain stable with respect to the incident angle.

For the system with a fixed orientation, the scattering coefficients and reflection spectra all depend on the relative angle between the photon direction and the iridosome orientation. In the Monte Carlo simulation, for each scattering event, we should select the proper phase function and the scattering coefficient depending on the direction of the photons relative to the iridsome. As shown in Figure 5.18 (b), the maximum reflectance shifted to shorter wavelength when incident angle increases; the color is green at $\beta = 0°$, and becomes bluer at $\beta = 30°$.

The considerations of the dependency of the extinction cross section on both the incident direction and polarization state are necessary to give accurate Monte Carlo simulations for fixed orientation particles. The diffuse reflection spectrum of a layer of iridosomes is found to depend on the incident direction (Figure 5.18 (b)), thus can be used to predict the color appearance of the animal. The Monte Carlo method can

enable us to calculate iridosome's optical response with arbitrary orientation distributions. For the real system, the orientation distribution could be a combination of random and fixed orientations. And there are many other complexities, like the size distribution, shape variance and so on, they will be discussed in our future work.

5.2 Scattering Properties of Leucophores

The white leucophore cell is usually located as the bottom layer of the skin of cephalopods, and it contains numerous transparent granules (leucosomes) with high refractive index [2]. As a good diffuse reflector, it plays a central role in matching the environment intensity through its high reflectivity. It provides a perfect background for the octopus to "paint" colors through the chromatophores and iridophores above it. They are observed in measurement as a broadband reflector with Lambertian reflection and no polarization components.

In our model, the leucophore is treated as a collection of solid spheres. From the electron micrograph of *Octopus vulgaris* as shown in Figure 1.1, the average diameter is estimated as $0.5\mu m$ (with a standard deviation $0.05\mu m$) is used. For different species or different body locations on one species, the size of the leucosome is not necessarily the same, but normally they are on the order of $1\mu m$, which enables them to maintain a similar optical appearance. The measurement of the refractive index is not currently available, thus the values from 1.1 to 1.4 relative to water (1.33) are chosen to study the sensitivity of the results. The total thickness of the system is chosen as $3\mu m$, and the estimated number density is around $3/\mu m^3$, as shown in Figure 5.19. Both these parameters are retrieved from the same electron micrograph to guarantee consistency.

The Lorenz-Mie theory (Section 3) is used to obtain the single scattering Mueller matrix and the extinction cross section. The discussion on the single scattering

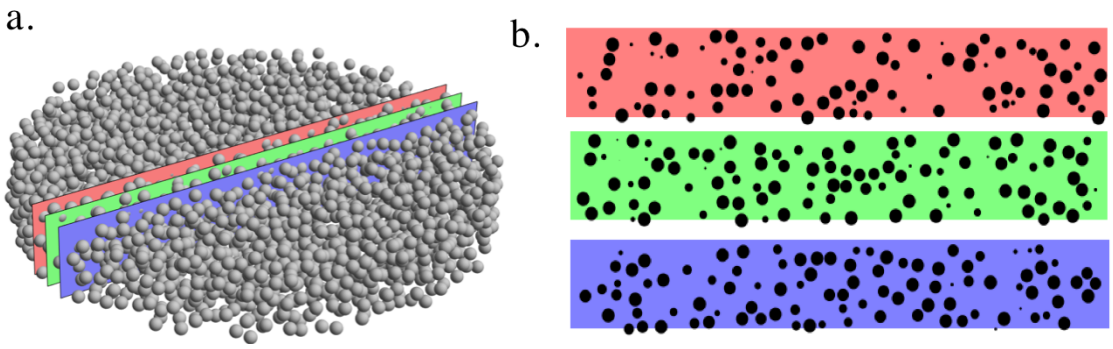

Figure 5.19: A 3d model for a leucophore with number density $3/\mu m^3$ and particle diameter $0.5\mu m$ (a) and the corresponding cross sections (b) through different vertical planes. Through the comparison of these cross sections with the electron micrograph, it can be estimated that iridosomes have a similar number density as around $3/\mu m^3$.

properties of a sphere can be found in [17, 16]. Using these results as input, the multiple scattering simulations are conducted by using the Monte Carlo method for randomly oriented particles as discussed in Section 4. The whole system is modeled as a semi-infinite plate with a finite thickness filled with leucosomes. The effective Mueller matrix (for the reflection of the whole system) for different wavelengths, refractive indices, and scattering angles will be calculated.

The diffuse reflectance (irradiance), the angular reflectance (radiance) and the degree of polarization ($DOP = \sqrt{Q^2 + U^2 + V^2}/I$) are calculated and shown in Figures 5.20, 5.21, 5.22 and 5.23 respectively. In our Monte Carlo method, as discussed in Section 4, we can study the contribution to the reflection with different orders of scatterings. And we will compare the all orders of scattering results with the results with only the first order of scattering. As shown in Figure 5.20, the reflectance from the first order of scattering is much smaller than the all order of scatterings. This means a leucophore is a strong multiple scattering system, and most of the photons from the incident light will undergo many scatterings before emergence. We cannot use the first order of scattering approximation to estimate the reflectance.

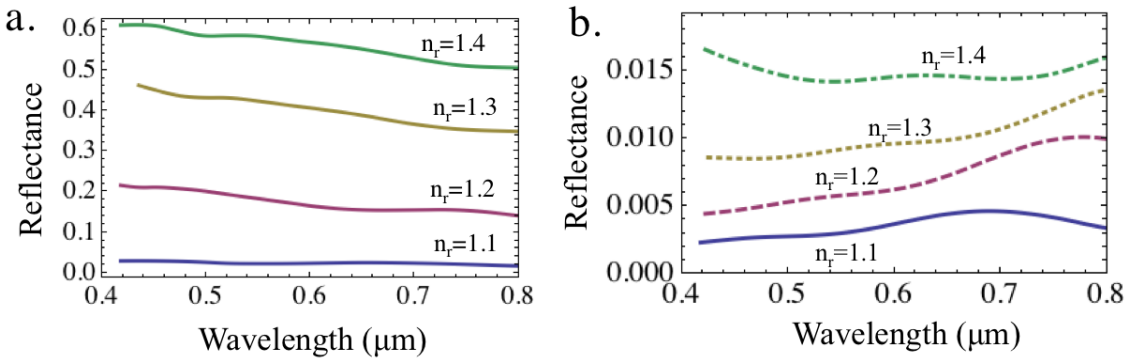

Figure 5.20: Diffuse reflection of the leucophore system for (a) all orders of scatterings, and (b) only the first order of scattering.

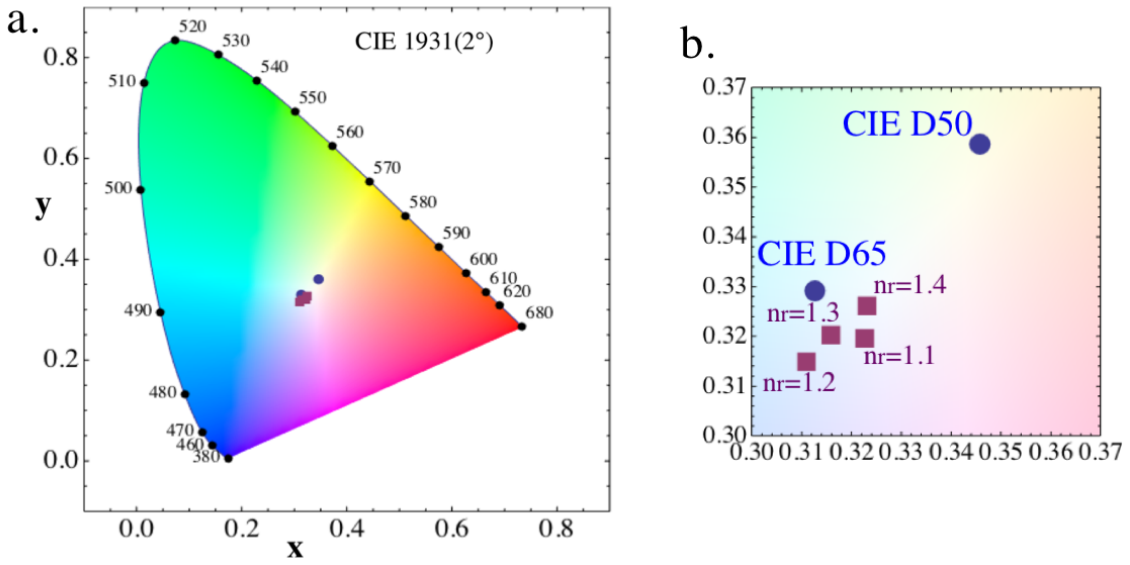

Figure 5.21: (a) Color coordinates for the leucophore reflection spectrum. CIE D50 and D65 denote two standard white light. (b) An enlarged graph near the center of (a).

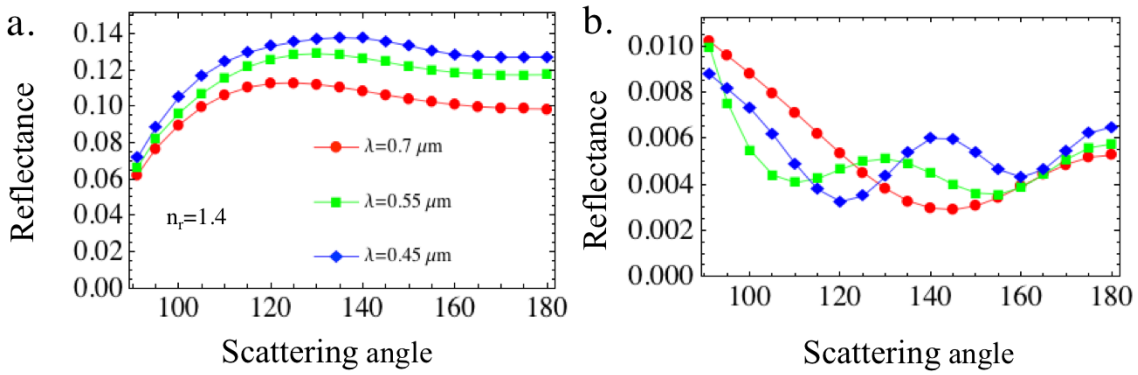

Figure 5.22: Angular reflectance(radiance) for all orders of scatterings (a) and for the first order of scatterings (b), and $n_r = 1.4$.

Although the refractive index is unknown, however, from the reflectance spectrum in Figure 5.20 (a), all of them can produce white reflectance—the reflectance spectrum is quite flat, with a variation less than 20% over the whole visual spectrum. (Note the wavelength here is defined in vacuum.) We calculated the color coordinates of the modeled reflectance spectrum in Figure 5.21 [57], and all of them are located at the center close to the CIE standard white light [58]. CIE D50 represents horizontal daylight, and D65 represents noon daylight. The change of refractive index will mainly change the overall reflectance but not the spectrum. When the observed reflectance is available, we can compare it with our simulated reflectance and determine the refractive index of the leucosome.

The angular reflectance and degree of polarization for $n_r = 1.4$ are shown in Figure 5.22 (a) and Figure 5.23 (b). The angular distributions are with respect to the scattering angles where 180° denotes backscattering, and 0° denotes forward scattering. The angular reflectance represents the radiance distribution with the incident beam having an irradiance of unity. Therefore, its angular integral can give the total reflection for irradiance as shown in Figure 5.20. It almost has an an equal reflection over a wide range of angles from 120° to 180°. This shows that leucophore

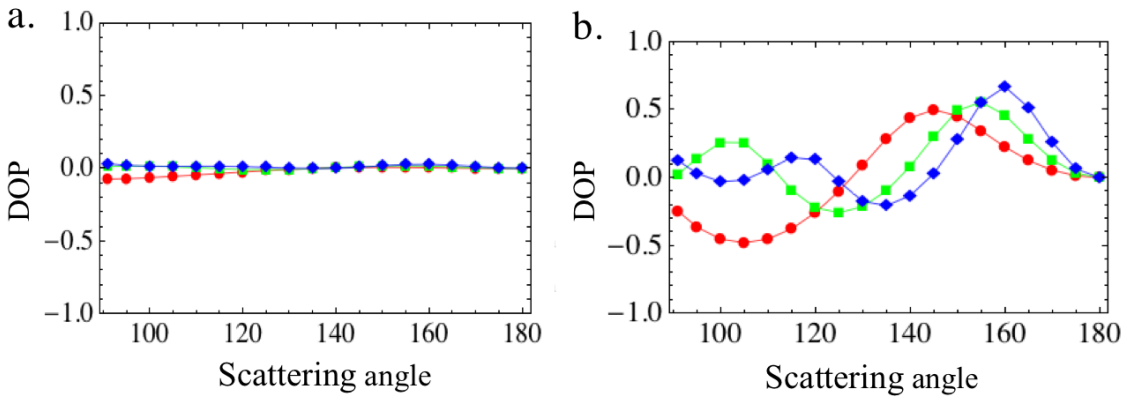

Figure 5.23: Degree of polarization(DOP) for all orders of scatterings (a) and for the first order of scatterings (b), and $n_r = 1.4$.

is a good Lambertian surface except for scattering angles close to the horizon. Over the whole backscattering range from $\theta_s = 90°$ to $180°$, the degree of polarization remains negligible.

However, from the comparison with the results for the first order of scatterings as shown in Figure 5.22 (b) and Figure 5.23, neither effects can be produced without multiple scatterings. Therefore, We have shown the three key features of a leucophore system: white, Lambertian, and no polarization, and the importance of the multiple scattering to produce them.

6. CONCLUSIONS

As an effort to understand the physics of the structural colors of cephalopods, we have summarized the numerical methods and provided the ab inio numerical studies of both leucophores and iridophores. The single scattering properties for the individual structure inside of both cells are obtained through the Mie theory and the DDA method. Many of the distinct optical properties are obtained for small structures. Through the Monte Carlo simulation on the multiple scattering properties, the effective Mueller matrices for the cells are obtained, and the reflectance spectrum is discussed.

In Section 2, 3 and 4, we have summarized the concepts and the numerical methods used to study both iridophores and leucophores, and therefore provide the framework to study the structural color of cephalopods. The single scattering methods discussed in Section 3 can be used to study the scattering properties of a single scatterer, and can also be extended to study other shapes. Through these methods we can obtain the scattering Mueller matrix and all other necessary results for the multiple scattering simulations as discussed in Section 4.

In Section 5, we studied the backscattering properties of small layered plates as a model for iridosomes, including the Mueller matrix, phase function, backscattering efficiency, and extinction matrix. We compared the Mueller matrix for a layered iridosome with that of a solid cylinder, and observed distinct features for the iridosomes which were lacking for the solid cylinder. We also shown that the Mueller matrix imaging can be useful to classify iridosomes with different size, shape and inner structure. The criteria for using the reflection of the semi-infinite plate to approximate the backscattering efficiency of small plates are discussed with respect to

the aspect ratio, number of layers, and incident angle. For plates with small aspect ratios and large incident angles, the scattering properties must be calculated beyond the semi-infinite approximation. Furthermore, the backscattering efficiency can be used to estimate the diffuse reflectance of a random system, and therefore, suggest its optical appearance.

Further in Section 5, from our Monte Carlo simulations, we have shown for iridophores, the orientations of iridosomes are important for them to produce a proper reflectance spectrum. With randomly oriented iridosomes, their reflectance spectrum are stable relative to different incident directions; but with fixed oriented iridosomes, different incident angles will produce different colors. For leucophores, since leucosomes are small spheres, there is no orientation effect. From our numerical results, we confirmed that leucophores can produce white Lambertian reflectance through multiple scattering. Through a further investigation on the contribution of different orders of scattering, the first order of scattering is not sufficient to produce any of these effects on leucophores.

We have worked on the structural data retrieved from the electron micrographs in the literature, but there is no corresponding reflectance measurement results we can compare with. Recently, we have started to collaborate with the Marine Biological Laboratory (MBL) at Woods Hole, Massachusetts, and to work on more accurate cell morphology data. Using the numerical methods provided in this work, we can compare our simulation results with the measured reflectance, and have obtained consistent results. These numerical approaches have proved to be useful in providing insights on the physics of the scattering process for both leucophores and iridophores. Many more systems will be studied following the approaches provided in this work.

REFERENCES

[1] R. Hanlon, C.-C. Chiao, L. Mathger, K. Buresch, A. Barbosa, J. Allen, L. Siemann, and C. Chubb, *Rapid adaptive camouflage in cephalopods* (Cambridge University Press, 2011), pp. 145–163.

[2] L. Mathger, N. Shashar, and R. Hanlon, "Do cephalopods communicate using polarized light reflections from their skin?" Journal of Experimental Biology **212**, 2133–2140 (2009).

[3] E. Denton and M. Land, "Mechanism of reflexion in silvery layers of fish and cephalopods," Proceedings of the Royal Society of London. Series B, Biological Sciences **178**, 43–61 (1971).

[4] M. F. Land, "The physics and biology of animal reflectors," Progress in Biophysics and Molecular Biology **24**, 75–106 (1972). Doi: 10.1016/0079-6107(72)90004-1.

[5] R. Sutherland, L. Mathger, R. Hanlon, A. Urbas, and M. Stone, "Cephalopod coloration model. i. squid chromatophores and iridophores," J. Opt. Soc. Am. A. **25**, 588–599 (2008).

[6] R. Sutherland, L. Mathger, R. Hanlon, A. Urbas, and M. Stone, "Cephalopod coloration model. ii. multiple layer skin effects," J. Opt. Soc. Am. A. **25**, 2044–2054 (2008).

[7] D. Froesch and J. Messenger, "On leucophores and the chromatic unit of octopus vulgaris," Journal of Zoology **186**, 163–173 (1978).

[8] L. Mathger, T. Collins, and P. Lima, "The role of muscarinic receptors and intracellular ca2+ in the spectral reflectivity changes of squid iridophores," Journal of Experimental Biology **207**, 1759–1769 (2004).

[9] J. Arnold, R. Young, and M. King, "Ultrastructure of a cephalopod photophore. ii. iridophores as reflectors and transmitters," Biological Bulletin **147**, 522–534 (1974).

[10] S. Brocco and R. Cloney, "Reflector cells in the skin of octopus dofleini," Cell and Tissue Research **205**, 167–186 (1980).

[11] R. Cloney and S. Brocco, "Chromatophore organs, reflector cells, iridocytes and leucophores in cephalopods," Integrative and Comparative Biology **23**, 581 (1983).

[12] K. Cooper, R. Hanlon, and B. Budelmann, "Physiological color change in squid iridophores ii. ultrastructural mechanisms in lolliguncula brevis," Cell and Tissue Research **259**, 15–24 (1990).

[13] S. Mirow, "Skin color in the squids loligo pealii and loligo opalescens ii. iridophores," Cell and Tissue Research **125**, 176–190 (1972).

[14] L. M. Mathger and E. J. Denton, "Reflective properties of iridophores and fluorescent 'eyespots' in the loliginid squid alloteuthis subulata and loligo vulgaris," Journal of Experimental Biology **204**, 2103–2118 (2001). Mathger, LM Denton, EJ.

[15] L. M. Mathger and R. T. Hanlon, "Malleable skin coloration in cephalopods: selective reflectance, transmission and absorbance of light by chromatophores and iridophores," Cell and Tissue Research **329**, 179–186 (2007).

[16] C. Bohren and D. Huffman, *Absorption and Scattering of Light by Small Particles* (Wiley-VCH Verlag GmbH, Weinheim, Germany, 2004).

[17] H. C. van de Hulst, *Light Scattering by Small Particles* (Dover Publications, New York, 1981).

[18] K. Liou, *An Introduction to Atmospheric Radiation* (Academic Press, New York, 2002).

[19] J. W. Hovenier, C. van der Mee, and H. Domke, *Transfer of Polarized Light in Planetary Atmospheres: Basic Concepts and Practical Methods* (Kluwer Academic, Boston, 2004).

[20] M. I. Mishchenko, L. D. Travis, and A. A. Lacis, *Multiple Scattering of Light by Particles: Radiative Transfer and Coherent Backscattering* (Cambridge University Press, Cambridge ; New York, 2006).

[21] S. Chandrasekhar, *Radiative Transfer* (Dover Publications, Inc., New York, 1960).

[22] G. W. Kattawar and C. N. Adams, "Stokes vector calculations of the submarine light field in an atmosphere-ocean with scattering according to a rayleigh phase matrix: effect of interface refractive index on radiance and polarization," Limnol. Oceanogr. **34**, 1453–1472 (1989).

[23] A. A. Kokhanovsky, *Polarization Optics of Random Media* (Springer-Praxis, Chichester, U.K., 2003).

[24] R. W. Preisendorfer, *Radiative Transfer on Discrete Spaces* (Pergamon, New York, 1965).

[25] M. Mishchenko, "Extinction and polarization of transmitted light by partially aligned nonspherical grains," Astrophys. J. **367**, 561–574 (1991).

[26] W. Hergert and T. Wriedt, *The Mie Theory: Basics and Applications*, vol. 169 of *Springer Series in Optical Sciences,* (Springer, 2012).

[27] G. B. Arfken and H. J. Weber, *Mathematical Methods for Physicists* (Academic Press, 2005).

[28] W. J. Wiscombe, "Improved mie scattering algorithms," Appl. Opt. **19**, 1505–1509 (1980).

[29] E. M. Purcell and C. R. Pennypacker, "Scattering and absorption of light by nonspherical dielectric grains," Astrophys. J. **186**, 705–714 (1973).

[30] B. T. Draine, "The discrete-dipole approximation and its application to interstellar graphite grains," Astrophys. J. **333**, 848–872 (1988).

[31] B. T. Draine and P. J. Flatau, "Discrete-dipole approximation for scattering calculations," J. Opt. Soc. Am. A **11**, 1491–1499 (1994).

[32] B. Draine and P. Flatau, "Discrete-dipole approximation for periodic targets: theory and tests," J. Opt. Soc. Am. A **25**, 2593–2703 (2008).

[33] B. T. Draine and P. J. Flatau, "User guide for the discrete dipole approximation code ddscat 7.2," http://arXiv.org/abs/1202.3424 (2012).

[34] M. A. Yurkin and A. G. Hoekstra, "The discrete-dipole-approximation code adda: Capabilities and known limitations," J. Quant. Spectrosc. Radiat. **112**, 2234–2247 (2011).

[35] J. D. . Jackson, *Classical Electrodynamics* (Wiley, New York, 1999), 3rd ed.

[36] B. E. A. Saleh and M. C. Teich, *Fundamentals of Photonics*, Wiley series in pure and applied optics (John Wiley & Sons, Hoboken, N.J., 2007), 2nd ed.

[37] E. Hecht, *Optics* (Addison-Wesley, Reading, Mass., 2002), 4th ed.

[38] A. Huxley, "A theoretical treatment of the reflexion of light by multilayer structures," Journal of Experimental Biology **48**, 227–245 (1968).

[39] M. Born and E. Wolf, *Principles of Optics: Electromagnetic Theory of Propagation, Interference and Diffraction of Light* (Cambridge University Press., 1999), 7th ed.

[40] P.-W. Zhai, Y. Hu, C. R. Trepte, and P. L. Lucker, "A vector radiative transfer model for coupled atmosphere and ocean systems based on successive order of scattering method," Opt. Express **17**, 2057–2079 (2009).

[41] H. H. Tynes, G. W. Kattawar, E. P. Zege, I. L. Katsev, A. S. Prikhach, and L. I. Chaikovskaya, "Monte carlo and multicomponent approximation methods for vector radiative transfer by use of effective mueller matrix calculations," Appl. Opt. **40**, 400–412 (2001).

[42] P.-W. Zhai, G. W. Kattawar, and P. Yang, "Impulse response solution to the three-dimensional vector radiative transfer equation in atmosphere-ocean systems. ii. the hybrid matrix operator–monte carlo method," Appl. Opt. **47**, 1063–1071 (2008).

[43] M. Wendisch and P. Yang, *Theory of Atmsopehric Radiative Transfer – A Comprehensive Introduction* (Wiley-VCH, Weinheim, Germany, 2012).

[44] G. W. Kattawar and G. N. Plass, "Interior radiances in optically deep absorbing media. 1.exact solutions for one-dimensional model," J. Quant. Spectrosc. Radiat. **13**, 1065–1080 (1973).

[45] A. Ishimaru, D. Lesselier, and C. Yeh, "Multiple scattering calculations for nonspherical particles based on the vector radiative transfer theory," Radio Sci. **19**, 1356–1366 (1984).

[46] A. Ishimaru, C. Yeh, and D. Lesselier, "First-order multiple scattering theory for nonspherical particles," Appl. Opt. **23**, 4132–4139 (1984).

[47] A. Ishimaru and C. W. Yeh, "Matrix representations of the vector radiative-transfer theory for randomly distributed nonspherical particles," J. Opt. Soc. Am. A **1**, 359–364 (1984).

[48] Y. Takano and K. N. Liou, "Solar radiative transfer in cirrus clouds. part ii: Theory and computation of multiple scattering in an anisotropic medium," J. Atmos. Sci. **46**, 20–36 (1989).

[49] K. F. Evans and G. L. Stephens, "A new polarized atmospheric radiative transfer model," J. Quant. Spectrosc. Radiat. **46**, 413–423 (1991).

[50] L. Tsang and K. H. Ding, "Polarimetric signatures of a layer of random nonspherical discrete scatterers overlying a homogeneous half-space based on first- and second-order vector radiative transfer theory [geophysical radar remote sensing]," Geoscience and Remote Sensing, IEEE Transactions **29**, 242–253 (1991).

[51] V. Berdnik and V. Loiko, "Radiative transfer in a layer with oriented spheroidal particles," J. Quant. Spectrosc. Radiat. **63**, 369–382 (1999).

[52] J. Hannay, "Radiative transfer: exact rayleigh scattering series and a formula for daylight," Proc. R. Soc. A **463**, 2729–2751 (2007).

[53] T. Chiou, L. Mathger, and R. Hanlon, "Spectral and spatial properties of polarized light reflections from the arms of squid (loligo pealeii) and cuttlefish (sepia officinalis l.)," Journal of Experimental Biology **210**, 3624–3635 (2007).

[54] R. Kramer, W. Crookes-Goodson, and R. Naik, "The self-organizing properties of squid reflectin protein," Nature Materials **6**, 533 – 538 (2007).

[55] P. Yang and K. N. Liou, "Geometric-optics-integral-equation method for light scattering by nonspherical ice crystals," Appl. Opt. **35**, 6568–6584 (1996).

[56] C. Li, G. Kattawar, and P. Yang, "Identification of aerosols by their backscattered mueller images," Opt. Express **14**, 3616–3621 (2006).

[57] C. Bohren and E. Clothiaux, *Fundamentals of Atmospheric Radiation* (Wiley-VCH, 2006).

[58] J. Schanda, *Colorimetry: Understanding the CIE System* (Wiley, 2007).